POLITECNICO
MILANO 1863

SCUOLA DI INGEGNERIA INDUSTRIALE
E DELL'INFORMAZIONE

NONLINEAR ROTORDYNAMIC MODEL OF A GAS TURBINE: COUPLING EFFECTS OF THE THRUST BEARING ON AXIAL VIBRATIONS

TESI DI LAUREA MAGISTRALE IN
MECHANICAL ENGINEERING-INGEGNERIA MECCANICA

Authors: Federico Palmisano, Alessandro Re Fraschini

Palmisano ID:	225790
Re Fraschini ID:	223351
Advisor:	Prof. Steven Chatterton
Co-advisor:	Ing. Ludovico Dassi
Academic Year:	2024/2025

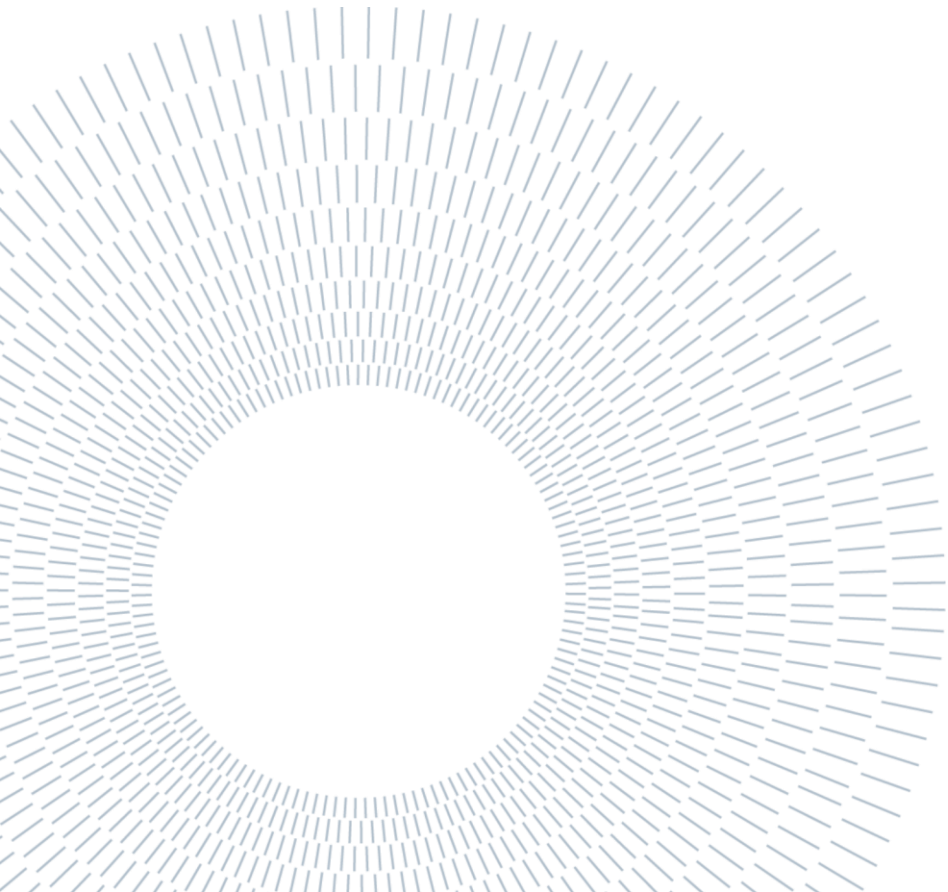

Abstract

Sub-synchronous vibrations (SSV) in the axial direction can be observed in both large gas turbines for power generation and small automotive turbochargers. Such vibrations, occurring at frequencies lower than the shaft's rotational speed, can reach significant amplitudes and pose a risk to structural integrity. Axial SSV can be triggered by lateral vibrations, resulting in coupled axial-lateral dynamics usually governed by the hydrodynamic thrust bearing. This component generates nonlinear forces and moments according to the Reynolds equation.

This work aims to investigate axial SSV and develops a rotordynamic model for a medium-sized (~100 MW) gas turbine capable of capturing the nonlinear coupling between axial and lateral dynamics. Due to the high computational cost of directly solving the Reynolds model, two approaches are proposed to compute bearing forces and moments: a feed-forward artificial neural network and an interpolator, both trained on datasets generated via offline MATLAB simulations. Time-domain numerical simulations with real oil film forces are also performed and compared to simplified model.

The linearized and nonlinear models are compared in terms of accuracy and computational efficiency. From numerical simulations of sinusoidal axial forcing of the unbalanced shaft, nonlinear effects are observed, such as intermodulation frequencies. Axial eigenfrequency depends on the static axial load. At low magnitude static axial load, reduced stiffness and damping cause large axial SSV. Coupling effects induced by the thrust bearing intensify when the collar approaches the bearing sides.

The resulting framework provides a foundation for further extensions to account for additional relevant effects beyond the scope of this study.

Key-words: thrust bearing, axial sub-synchronous vibrations, nonlinear axial dynamic, artificial neural network, FEM

Abstract in lingua italiana

Le vibrazioni sub-sincrone (SSV) nella direzione assiale si osservano spesso sia nelle grandi turbine a gas per la produzione di energia, sia nei piccoli turbocompressori automobilistici. Tali vibrazioni, che si manifestano a frequenze inferiori rispetto alla velocità di rotazione dell'albero, possono raggiungere ampiezze elevate e compromettere l'integrità strutturale del sistema. Le SSV assiali possono essere innescate da vibrazioni laterali, dando origine a una dinamica accoppiata assiale-laterale, governata dal comportamento del cuscinetto reggispinta idrodinamico, che genera forze e coppie non lineari secondo l'equazione di Reynolds.

Questo tesi ha l'obiettivo di analizzare le vibrazioni SSV assiali e sviluppare un modello rotodinamico per una turbina a gas di media potenza (circa 100 MW), capace di rappresentare accuratamente l'accoppiamento non lineare tra le dinamiche assiali e laterali.

Considerando l'elevato costo computazionale della soluzione diretta del modello basato sull'equazione di Reynolds, vengono proposte due strategie alternative per il calcolo delle forze e delle coppie generate dal cuscinetto: una rete neurale artificiale di tipo feed-forward e un interpolatore, entrambi addestrati su un insieme di dati ottenuto da simulazioni realizzate separatamente in MATLAB. Si eseguono anche simulazioni numeriche nel dominio del tempo, considerando le reali forze sviluppate dal meato d'olio, per essere confrontate con il modello semplificato.

I modelli lineare e non lineare vengono quindi confrontati in termini di accuratezza e prestazioni computazionali. Dalle simulazioni numeriche di forzamento assiale sinusoidale, si osservano effetti non lineari, quali le frequenze di intermodulazione. La frequenza propria assiale dipende dal carico assiale statico. A basso carico assiale statico, rigidezza e smorzamento ridotti causano SSV assiali di ampiezza elevata. L'effetto di accoppiamento indotto dal cuscinetto assiale si intensifica quando la ralla si avvicina ai lati del cuscinetto.

Il modello sviluppato costituisce una base solida per sviluppi futuri, finalizzati a includere ulteriori effetti rilevanti non considerati in questo studio.

Parole chiave: cuscinetto assiale, vibrazioni assiali sub-sincrone, dinamica assiale non lineare, rete neurale artificiale, FEM

Contents

Abstract ..... **i**

Abstract in lingua italiana ..... **ii**

Contents ..... **iii**

1 Introduction **1**

1.1 Statement of the problem 1

1.2 Literature review 3

1.3 Thesis overview 6

2 Thrust bearing system **11**

2.1 Thrust bearing description 11

2.2 Machine axial dynamics 16

2.3 Equalizing thrust bearings 19

2.4 Thrust bearing used in the model 22

3 Fluid dynamic model **23**

3.1 Theoretical approach 23

3.2 Fluid dynamic model: inputs and outputs 29

4 Results of fluid dynamic model **35**

4.1 Axial force and moments varying y and ϑ 35

4.2 Axial force and moments varying y, ϑ and ψ 38

4.3 Axial force and moments varying ϑ and ϑ 40

5 Rotordynamic model **43**

5.1 Machine description 43

5.2 Rotordynamic model 44

5.2.1 FEM model 45

5.2.2 Bearings model 54
5.2.3 Unbalance model 55
5.2.4 Blade excitation model 56
5.2.5 Axial dynamics 57
5.3 Static equilibrium due to weight 57
5.4 Linear solution 59
5.4.1 Modal analysis 61
5.5 Nonlinear solution 62
6 Craig-Bampton approach 67
6.1 Introduction 67
6.2 Mathematical description 69
6.3 Validation 74
7 Artificial Neural Network 79
7.1 Introduction 79
7.2 Net for force and moments predictions 83
7.3 Net limitations 85
7.4 Velocities estimation 87
7.5 Dataset 88
7.6 Net architecture analysis 91
7.7 Analysis of net errors 93
7.8 Considerations about the net 94
7.9 Interpolator 95
7.10 Analysis of interpolator errors 97
8 Results of the linear model 99
8.1 Thrust bearing free case 100
8.1.1 Static deflection and bearing reaction forces 100
8.1.2 Campbell diagram and mode shapes 100
8.1.3 Unbalance response 106
8.1.4 Shaft shape and orbits due to unbalance excitation 108

8.2 Thrust bearing activated 109
8.2.1 Static deflection and bearing reaction forces 109
8.2.2 Sensitivity map 115
8.2.3 Stability map 119
8.2.4 Unbalance response 120
8.2.5 Mode shapes 121
8.2.6 Change in thrust bearing position 126
9 Time integration results 129
9.1 Radial dynamics only 129
9.1.1 Unbalance response 129
9.1.2 Radial noise 131
9.2 Axial dynamics 135
9.2.1 Axial noise 135
9.2.2 Axial sinusoidal excitation 137
9.2.3 Undamped thrust response 143
9.2.4 Axial noise and radial analysis 145
9.2.5 Radial noise and axial analysis 148
9.2.6 Load ramp with axial noise 149
9.3 Pad dynamics 151
10 Conclusions 155
Bibliography 157
List of Figures 161
List of Tables 167

1 Introduction

1.1 Statement of the problem

Large rotating machines typically rely on fluid film bearings to support high loads while avoiding direct contact between moving components. These bearings operate through a thin lubricant film that minimizes friction and wear, making them ideal for continuous operation. Based on the principle of hydrodynamic lubrication, they generate a pressure distribution within the lubricant drawn into the clearance between moving surfaces, thereby sustaining the applied loads. However, since these bearings exert forces on the system, they strongly influence the overall dynamic behaviour and stability of the machine.

A turbomachinery system comprises interconnected components such as blades, bearings, and labyrinth seals, each introducing distinct dynamic behaviours. The complexity of the system emerges from interactions among these elements, which often lead to nonlinear and difficult-to-predict responses. Aerodynamic forces on blades vary with operating conditions and can induce bending and torsional vibrations. Meanwhile, hydrodynamic forces in labyrinth seals, driven by swirling flows, often involve cross-coupling effects where motion in one direction produces forces in another, contributing to rotor destabilization. Further complicating the dynamics are pressure pulsations from upstream disturbances and blade-passing frequencies, which impose periodic forces on the shaft: these forces excite the rotor natural modes. Simultaneously, thermal gradients within the rotor generate transient stresses and deformations that alter clearances in bearings and seals, modifying lubrication film thickness and redistributing aerodynamic forces, thereby affecting local stiffness and damping. Couplings or assembly imperfections can cause localized variations in dynamic stiffness, distorting the expected responses. Variations in electrical load alter the transmitted moment, influencing torsional dynamics. Furthermore, mechanical anomalies including rubbing, thermal bow, loosened fasteners, gear defects, and electromechanical irregularities can influence vibrations and can be identified through analysis of radial displacement frequency spectra. The latter can even help to discover signs of damage such as polar stiffness

asymmetry, journal ovality, or cracks. In such systems, localized problems then quickly propagate through component interactions. Accurate prediction of the dynamic behaviour of industrial rotating machinery is therefore critical during the design phase. However, in practice, many problems are resolved empirically relying on engineering intuition, experience, or trial-and-error, while analytical models may lack sufficient precision.

A common standard in rotordynamic analysis is to neglect axial degrees of freedom because axial motion is generally not linked to instability or failure. For this reason, simulations typically focus solely on radial dynamics.

Machines such as compressors and gas turbines are equipped with double-acting oil-lubricated thrust bearings, to support axial loads generated by blade–flow interactions. Rarely, in presence of these components, axial sub-synchronous vibrations (axial SSV) are observed [1]. Amplitude of such vibrations can span the full bearing clearance, representing an issue for structural integrity of the engine. The term *sub-synchronous* refers to vibration frequencies lower than the shaft rotational speed, typically below 50 or 60 Hz, depending on the electrical grid standard (e.g., 50 Hz in Europe and 60 Hz in North America). Axial SSV may lead to rubbing, fretting, fatigue, or even pivot seizure [2], and can also reduce the bearing load-carrying capacity. Moreover, it is challenging to predict and even to detect, as it is rarely monitored in standard configurations.

Additionally, as it is shown in *Chapter 2.2*, the thrust bearing collar is an integral part of the shaft. Consequently, lateral vibrations of machine results in an angular oscillation of the thrust collar. Therefore, variations in the oil film thickness inside the bearing depend not only on axial displacement but also on shaft bending. This creates a circumferentially non-symmetric distribution of hydrodynamic lubrication forces on the pads of the thrust bearing, that generate two moments around the horizontal and vertical axes. These moments influence local rotations and overall radial vibrations, meaning vibrations perpendicular to the shaft axis. Furthermore, when there is no static load, the runner is usually positioned off-centre within the clearance due to an uneven distribution of oil film thickness between the two sides [3]. This asymmetry arises because the side designed to operate under nominal conditions requires a greater stroke to increase load capacity and prevent excessive temperature rise even at low loads. Any significant rotation produces a net axial force caused by the difference in lubricant film thickness between the two sides of the bearing. These reaction forces couple the axial and radial dynamics, enabling sub-synchronous vibrations to occur simultaneously in both directions with the same frequency content.

Due to the limited research available on this phenomenon, the objective of this thesis is to develop a numerical model capable of reproducing axial SSV in a manner consistent with field observations, thus contributing to a better understanding of their origin and to the formulation of effective mitigation strategies.

1.2 Literature review

Several studies apply simplified linearized models to investigate the coupled behaviour of thrust bearings.

- Mitwollen and Hegel in [4] model the static and dynamic response of a thrust bearing by focusing on the axial dynamics of a single pad, assuming that runner misalignment does not affect system behaviour. The model derives tilt-related coefficients from purely axial static and dynamic properties and includes both direct and cross-coupling terms, with the latter accounting for tangential forces. Results indicate that reducing bearing clearance or increasing the applied load increases the critical speed, raises the instability threshold and amplifies whirl-related vibration amplitudes.
- Lie et al. in [5] examine the influence of thrust bearings on system-level dynamics and identifies strong coupling effects. Static tilt significantly alters stiffness and damping coefficients, modifies journal eccentricities, and enhances dynamic coefficients. The resulting stiffening effect reduces static shaft deflection and increases critical speeds. Additionally, the analysis shows a reduction in the positive real part of the unstable eigenvalue of the system, indicating improved dynamic stability.

Pads could be seen as a potential driver for coupling or even for instabilities and SSV:

- According to Kiuchi in [6], the cross-coupling stiffness increases when the pad's static equilibrium is disrupted. These coefficients then act as the primary driving mechanism behind the coupled radial–axial vibrations.
- Gardner [7] and Wu in [8] identify fluid dynamic instabilities as a primary cause of thrust bearing vibrations. These arise from either insufficient or excessive oil flow and become particularly evident during transient phases such as start-up or shut-down or under off-design operating conditions. During these phases the bearing may experience uneven loading, potentially unloading one side of the thrust surface. The phenomenon is observed also by Mikula et al. in [9], comparing different lubricant supply methods.

  When the pad tilts freely, a low oil flow rate on the unloaded side generates hydrodynamic forces aligned with the pad displacement. This interaction

results in unstable vibration behaviour. Several mitigation strategies aim to stabilize the system. These include increasing the oil flow rate, applying back pressure to maintain oil coverage in the bearing, and reducing pad clearance. However, these instabilities occur at flow rates that are significantly lower than those used in typical operations.

Conversely, at high flow rates resonance may arise when the excitation frequency aligns with the natural frequency of the pad and oil film system. Pressure pulsations caused by vortices form near the discharge connection and travel with the rotation of the thrust collar, acting as a source of excitation. The degree of discharge restriction directly influences the success of mitigation efforts. If the oil annulus remains only partially filled, vortex formation and propagation are suppressed, and the likelihood of excitation decreases. A detailed analysis includes evaluating the Strouhal number and estimating the pad's natural frequency. The practical recommendation suggested is then to avoid fully flooded conditions in the annulus to limit the generation of hydrodynamic excitations.

- Decamillo in [10] associates axial sub-synchronous vibrations (SSV) with a forced natural frequency. The excitation source involves pressure pulsations within the discharge annulus, as already identified by Gardner, or a coupling between pad super-synchronous vibrations and shaft vibrations. Experimental testing shows that increasing the oil flow rate, raising the axial load, or reducing the clearance consistently increases the SSV frequency and decreases their amplitude. This behaviour reflects a general stiffening of the system.
- Ishimoto and Marques in [11] highlight that axial sub-synchronous vibrations (SSV) is an instability. Increasing system stiffness by raising oil flow rate and supply pressure eliminates these vibrations. These findings confirm Decamillo's conclusion that higher axial loads suppress vibrations when pad flutter excites the system. Full-load operation shows no axial SSV, which indicates that light loads and off-design conditions primarily cause their occurrence. These vibrations likely originate then according to the authors from insufficient lubrication and pad flutter in the thrust bearing.

De Camillo in [10] provides further insights on axial sub-synchronous vibrations (SSV):

- The balance piston prevents low load conditions on the bearing that otherwise contribute to instability.
- Asymmetry between forward and reverse sides does not mitigate the problem.

- The pad offset improves stability but increases temperature and reduces load capacity.
- High-speed tapers (a tapered region on the leading edge of the shoe) add stiffness to the system and help control SSV.
- Analysis of load cell data reveals a clear link between the high-speed low-load phenomenon, where high speed fails to pressurize the oil, and the presence of SSV within certain pad load ranges. The suggested link is that pads vibrate when unloaded, which enhances SSV. To counteract the drop in hydrodynamic force, O-rings also suppress all pad vibrations.

The problem of axial-lateral coupling is also reported commonly on turbochargers.

- Peixoto et al. in [12] highlight the significance of nonlinear effects in turbochargers operating at high rotational speeds and low mass. The approach uses a database to avoid repeatedly solving Reynolds equations at each time step, especially when accounting for thrust runner rotations and thermal effects. Results show that axial excitation triggers instability in floating ring bearings within compressors as well as oil whirl due to the coupling between axial and radial motions. This excitation affects both axial and radial directions and influences the average temperature of the bearings.
- Chatzivasavas in [13] investigates the influence of thrust bearing parameters on the conical vibration mode of a turbocharger rotor, focusing on oil viscosity, axial loading, and bearing geometry. Increased angular stiffness and damping caused by the thrust bearing delay the onset of sub-synchronous vibrations (SSV) and reduce their amplitude. A parametric study shows that increasing the number of bearing pads increases the axial distance between the collar and the pads, due to elevated oil pressure. Conversely, reducing the number of pads suppresses these instabilities without significantly affecting the amplitude of other vibration modes. Higher thrust forces reduce SSV amplitude and shift the onset to higher rotational speeds, indicating an overall stabilizing effect. Under isothermal conditions, increased oil viscosity causes the rotor to move away from the bearing surface thanks again to pressurization, altering the hydrodynamic pressure distribution and influencing the onset speed of instabilities. Lower viscosity delays their appearance, especially for vibrations related to the conical mode.
- Koutsovasilis in [14] investigates the effect of thrust bearing on radial vibrations and evaluates its influence on critical speeds, shaft motion, and load-carrying capacity. The study includes simulations to assess the impact of shaft diameter and thrust bearing position. The thrust bearing influences the subsynchronous vibrations (SSV) generated by floating journal bearings. When using constant direct terms for the thrust bearing coefficients, the model

predicts a general increase in radial natural frequencies compared to the configuration without thrust bearing. The influence of the thrust increases when the shaft at that thrust location rotates more, indicating that the bearing position strongly affects mode frequencies. Its position affects vibration amplitudes by generating moments that require larger journal eccentricities. Simulated loads exceed nominal values, underlining the need to model the behaviour accurately for proper sizing of bearings. When the angular tilt at the thrust position increases, forces and moments grow, increasing the likelihood of exciting the conical vibration mode.

Dassi, Chatterton, and Pennacchi in [15] identify, through numerical simulation of the De Camillo test rig, that the frequency of the first bending mode matches both the experimentally observed SSV frequency and the axial mode frequency, confirming previous hypotheses by Ishimoto and Peixoto. The result highlights the role of the thrust bearing in increasing the shaft radial stiffness by coupling axial and rotational degrees of freedom. A parametric analysis outlines the following trends:

- Increasing bearing axial stiffness raises the SSV frequency and reduces its amplitude.
- Increasing the applied load shifts the SSV frequency upward and decreases its amplitude.
- Higher oil inlet temperatures, under flooded conditions, reduce the flow rate and bearing pressurization, increase the nonlinearity of the axial force–displacement curve, and lower the axial natural frequency.
- Increasing clearance decreases pressurization, reduces bearing stiffness, enhances system nonlinearity, and lowers the axial natural frequency.
- Increasing shaft speed improves pressurization and raises the axial natural frequency.

Each of these findings reinforces the role of thrust bearing dynamics in modulating system stability and vibration behaviour.

1.3 Thesis overview

- *Chapter 1* is an introduction about axial SSV problem and presents a literature overview concerning this topic.
- *Chapter 2* provides a technical description of thrust bearings, presenting different types commonly used in industrial applications. It also provides a detailed description of thrust bearing used in the thesis.

- *Chapter 3* describes, from a theoretical point of view, the Reynolds model, governing the lubricant film behaviour. MATLAB code used to solve such equation is described, focusing on the assumptions introduced and the limits.
- *Chapter 4* presents the analysis of fluid film forces, particularly for the thrust bearing studied in the thesis.
- *Chapter 5* describes the machine (W501D) geometry and the numerical nonlinear model used. FEM theory and its application on the system analysed in the thesis are shown. A brief introduction of nonlinear model theory supports nonlinear analyses addressed in the next chapters.
- *Chapter 6* describes the theory about Craig-Bampton model reduction and its application on the analysis performed in the thesis.
- *Chapter 7* provides a brief introduction to Artificial Neural Networks (ANN) and their applications on estimation of Reynolds nonlinear hydrodynamic forces. Advantages and disadvantages and possible alternatives of ANN are also shown.
- *Chapter 8* presents the results of the linear analyses performed.
- *Chapter 9* presents the results of the nonlinear analyses performed.
- *Chapter 10* reports the conclusions drawn from the thesis and suggests possible future developments.

This study performs a numerical analysis using MATLAB to model a gas turbine configuration similar to the machine, operating at a nominal speed of 3600 rpm.

Experimental observations reveal a significant amplification of sub-synchronous shaft vibrations (SSV) when the excitation frequency matches the first axial rigid mode of the shaft [10], indicating resonance condition [15]. Moreover, the rotor exhibits extremely high axial stiffness, making the relative axial deformability among individual shaft elements negligible. Additionally, the natural frequencies associated with axial deformation exceed typical excitation ranges, preventing substantial dynamic activation under normal operating conditions. Therefore, the model assumes negligible relative axial displacement between adjacent elements. This assumption simplifies the model by neglecting axial deformation across the rotor and considering only a single axial degree of freedom for the entire shaft line. The model incorporates this axial degree of freedom within the system matrices and vectors alongside the existing radial degrees to represent rigid-body axial motion.

The analysis initiates with a linear model formulation. The system matrices integrate damping and stiffness coefficients characterizing the restoring forces generated by journal and thrust bearings. The study investigates system responses to unbalance

forces resulting from uneven mass distribution along the shaft and to harmonic axial excitations potentially induced by axial noise. Additionally, the model evaluates the eigenvalues of the state matrix to assess system stability and identify corresponding mode shapes.

Linear models enjoy widespread application due to their straightforward numerical implementation and low computational demand. Nonetheless, their validity is confined to operating conditions near equilibrium and to small-amplitude vibrations. They enforce a linear input-output relationship via Taylor expansion, despite the actual system response potentially exhibiting complex, non-analytic behaviour. Consequently, linear models fail to capture system dynamics under elevated excitation levels, such as those caused by significant external loads or self-excited phenomena. This shortcoming necessitates a more accurate modelling approach capable of capturing inherent system nonlinearities, particularly those introduced by the runner. Accordingly, the study develops a nonlinear model by incorporating the nonlinear forces and moments generated by the thrust bearing. Accounting for these effects improves harmonic response predictions and enhances parametric study accuracy. The analysis employs spectrograms and Fourier series to compare linear and nonlinear model outputs. Spectral analysis of nonlinear simulations better represents the true system behaviour and enables comparison with measured signals from accelerometers, displacement, or pressure sensors installed on the bearings.

Nonetheless, this approach encounters a fundamental challenge: the oil film force relationship for the thrust bearing lacks an analytical expression. To model forces and moments acting on the thrust collar, Reynolds equations require numerical solution for each side of the thrust bearing, the direct and reverse sides, and for each bearing pad. The solution depends on a complex set of state variables, including the axial position of the runner, rotations about vertical and horizontal axes, and corresponding velocities. Additional parameters such as oil temperature, turbine speed, and clearance significantly affect the reactions at the bearing. For simplicity, this study fixes these parameters and reserves investigation of their influence for future research.

The model simulates the time evolution of the entire turbine state by evaluating forces and moments at every instant. At each timestep, the solver iteratively balances forces and moments between the thrust runner and bearing pads. This iterative procedure assumes that bearing pads respond considerably faster than the overall system dynamics, enabling the model to treat pads as reaching instantaneous equilibrium for the current configuration.

However, this iterative solution proves computationally expensive, especially when nested within the multiple iterations required by numerical solvers such as MATLAB

ode45 to minimize errors. To mitigate this bottleneck, the study employs a trained neural network or interpolators to approximate thrust bearing forces and moments, substantially accelerating simulations.

The investigation evaluates axial eigenfrequencies alongside radial ones and compares the performances of linear and nonlinear models. It also examines the coupling behaviour of the thrust collar, demonstrating that rotations and angular velocities generate not only moments but also net axial forces. Even small angular displacements, when coupled with axial degrees of freedom, produce significant moment contributions. Furthermore, the analysis incorporates the effects of static sag deflection on coupled shaft dynamics. The dynamic coupling, together with system nonlinearities, forms a core focus of the thesis. The study concludes by proposing several avenues for future research, aimed at better understanding and mitigating axial SSV phenomena.

2 Thrust bearing system

2.1 Thrust bearing description

This section describes a typical thrust bearing, as this component plays a critical role in the coupling mechanism.

Thrust bearings support loads acting along the shaft axis, constrain axial motion, and contribute to overall system stability, as shown in *Figure 2.1b*. The assembly typically consists of a collar, which forms an integral part of the shaft and has a larger diameter than adjacent shaft sections, and two annular structures mounted coaxially around the shaft. These structures contain multiple pads positioned to face the collar. In a double-sided thrust bearing configuration, one set of pads is located on each side of the collar (e.g. on the left and right). Each annular structure functions as an individual *thrust bearing*, so a complete machine typically incorporates two thrust bearings mounted symmetrically with respect to a plane normal to the shaft axis and passing through the midpoint of the collar. The doubled-sided thrust bearing configuration is typical for turbines for power generation: the net axial load, given by the thrust load of the turbine and compressor stages, depends on the machine configuration and on the machine active power. This force drives the rotor toward the direct side under steady-state conditions and toward the reverse side during transients.

(a) (b)

Figure 2.1: (a) Example of thrust bearing; (b) section comprising collar and doubled-sided thrust bearing

The two thrust sides are commonly referred to as *direct* and *reverse* (or *slack*). The direct side corresponds to the surface where most of the hydrodynamic force develops during steady-state operation, which represents a significant portion of the machine operating cycle. At steady-state, the machine operates at high power load, resulting in a high turbine axial force. The reverse side, although less loaded in steady conditions, plays a key role during transients. The difference between the two bearings arises from design considerations: the direct side operates under load for most of the time and therefore requires higher robustness to withstand wear and fatigue, whereas the reverse side features a simpler and more cost-effective construction.

In each pad, oil enters in the leading edge and exits from the trailing edge (highlighted in *Figure 2.3*). In the gap between the collar and the pads the lubricant flows, because of the adhesion with respect to the surface of the runner (stick-slip condition, that forces the oil of assuming the velocities of bodies at its interface), generating a pressure distribution according to hydrodynamic lubrication principle described in *Chapter 3.1*. The oil pressure generates a force acting on the collar and consequently on the whole shaft. A typical pressure distribution at the static equilibrium position is illustrated in *Figure 2.2*.

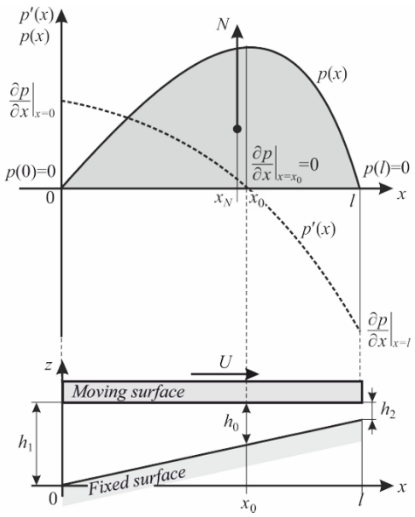

Figure 2.2: Pressure distribution in infinitely long bearing

The pad consists of a steel plate, typically made of structural steel such as S355, with a smooth surface over which oil flows. During operation, especially in the start-up phase, components with relative motion like the pads and collar in a thrust bearing may come into contact. To protect the shaft from damage in such cases, the pads are coated with a low-friction metal alloy that melts upon contact. This alloy generally consists of antimony, tin, and lead, known as white metal or Babbit metal, named after its inventor Isaac Babbit. Due to its limited mechanical properties including resistance, hardness, and creep resistance, surface conditions must remain moderate to extend the service life before replacement is necessary. Specific load and temperature are key parameters to monitor because of their significant impact on pad lifespan. As a guideline, pressure should not exceed 5 MPa at any point on the pad, with an average value between 2 and 3 MPa, while temperature should stay below 110 to 120 °C. Although newer materials exist to partially address these limitations, these values are considered upper limits for the purposes of this thesis.

Industrial thrust bearings come in various arrangements such as different oil supply mechanisms or pad configurations, but their fundamental operating principle remains consistent. The following section lists and briefly explains typical thrust bearings used in industrial applications.

Figure 2.3: Example of pad; particular of leading and trailing edge

To increase oil pressure and consequently the load support capacity, each pad is inclined to form a converging gap where the oil film thickness at the leading edge is greater than at the trailing edge.

This objective can be achieved through some ways:

- *tilting pads*, in which pads are free to rotate around point (*Figure 2.4a)* or a line orthogonal to the shaft axis (*Figure 2.4b)*, known as the pivot. This arrangement also improves shaft stability, especially for high speeds High specific pressures act on the pivot, requiring very hard materials such as quenched and tempered martensitic steel 100Cr6. Due to their widespread industrial use, the majority of medium and high-speed machines are equipped with tilting pad thrust bearings (TPTB). The system analysed in the following pages uses these particular bearings.

(a)

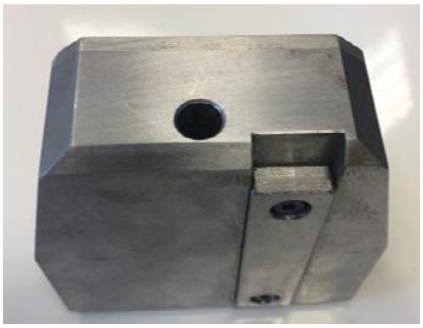

(b)

Figure 2.4: Different pivot configuration: (a) point; (b) line

- *fixed inclined pads*, commonly used in high-speed turbochargers, that are designed so that the pads remain stationary relative to the casing. A schematic representation is shown in *Figure 2.5*.

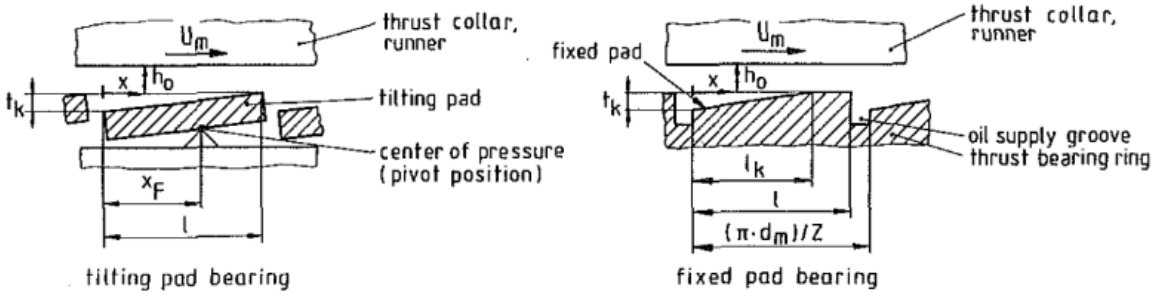

(a) (b)

Figure 2.5: Geometry of: (a) tilting pad bearing; (b) fixed pad bearing

When a machine has two collars, the two thrust bearings (TBs) are not mounted on the same collar but instead two separate collar-TB systems are located at different positions along the shaft. In this case, two configurations are possible: front-to-front and back-to-back, depending on which side of the collar the pads are mounted.

A pump recirculates lubricant oil throughout the bearing for lubrication and then sends it to a heat exchanger to cool the lubricant and maintain the temperature below a safe threshold for continuous operations. Regarding the oil supply method, thrust bearings (TB) are classified into *flooded* and *direc*t lubricated types (see *Figure 2.6*). Flooded bearings, as the name suggests, are completely immersed in a bath of lubricant. Two seals, located on the two sides of the bearing, constrain the oil flow to remain inside the bearing. Cold oil is pumped under the pads and flows through the gap between the pads to reach the pad surface, mixing with the hot oil present and causing hot oil carryover. To ensure the complete formation of the oil film, a quantity of lubricant much greater than required is supplied due to leakage, although the exact amount of leakage is difficult to estimate. This conventional design has been widely used in industry for many years, mainly because of its simplicity. A visual representation of a *flooded* arrangement is shown in *Figure 2.6a.*

In direct lubricated TBs, oil is supplied directly to the pad surface by spray nozzles without significantly lubricating other parts of the bearing. The amount of cold oil supplied exceeds theoretical requirement but is less than in flooded bearings. This design greatly reduces mixing between cold and hot oil, improving the lubrication

mechanism, reducing power losses, and lowering the excess flow rate needed. *Figure 2.6b* illustrates the direct lubrication type.

A typical arrangement for direct lubrication is the *Leading Edge Groove* (LEG), shown in *Figure 2.6c*. This consists of a groove or pocket machined into the pad at the leading edge, which the lubricant completely and continuously fills thanks to a recirculating pump. The oil exits the groove and flows over the pad surface, distributing quite evenly. This mechanism eliminates the hot oil carryover issue, keeping stable the temperature at the inlet of the pad. Because of this design, little space is left between pads, as a larger gap is unnecessary. Occasionally, if the oil supply is insufficient, direct lubricated bearings may behave like flooded bearings, but this situation is undesirable and occurs only outside normal design conditions.

(a) (b) (c)

Figure 2.6: Particular of oil supply arrangement: (a) flooded; (b) spray bar; (c) LEG thrust bearing

2.2 Machine axial dynamics

The thrust bearing plays a key role in the axial dynamics of the entire machine, acting as the only axial constraint. The shaft generally exhibits much higher stiffness in the axial direction than the oil film, allowing it to be treated as a rigid body with respect to axial displacements. The model developed in this work adopts this assumption. Axially, the machine is essentially represented by 1 *dof* system, where:

- the inertia is due to the mass of the entire rotor: about 48,758 kg for the machine considered in the thesis.

- a nonlinear hydrodynamic force, depending both on position and velocity, arising at the interface between the collar and the oil film, represent equivalent stiffness and damping forces. The hydrodynamic model, based on Reynolds equation, is presented in *Chapter 3.1*.
- excitation is due to generic interaction between blades and working fluid (aerodynamic excitation) or turbulence in the pads of the TB.

The linear model captures axial dynamics by incorporating linearized damping and stiffness coefficients into the respective system matrices. The nonlinear model instead includes the actual hydrodynamic force on the right-hand side of the motion equation, specifically in the row associated with the axial degree of freedom. The assembly procedure of both linear and nonlinear models is explained in detail in *Chapter 5.2*.

The asymmetric design of the direct and reverse sides leads to significant differences in both the magnitude of the oil film force and the associated stiffness. In *Figure 2.7*, the strong nonlinear behaviour between the axial displacement of the machine and the resulting oil film force of the thrust bearing is highlighted, for the case considered in the thesis. The static equilibrium position primarily depends on the applied static load and on runner rotation. The influence of runner rotation becomes particularly relevant when strong coupling occurs, as discussed later.

The direct side corresponds to the negative y direction, while the reverse side aligns with the positive y direction. *Figure 2.7* illustrates the relationship between the axial force and axial displacement, assuming the runner vertical in axial equilibrium condition.

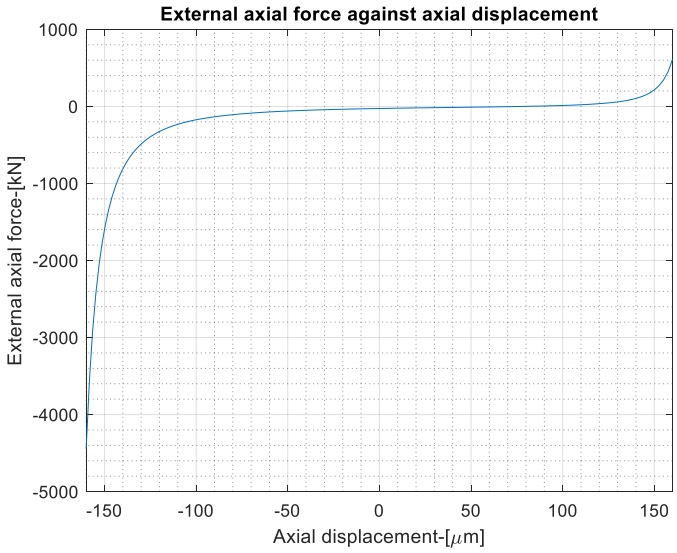

Figure 2.7: Nonlinear axial load-displacement relation

Different situations, in terms of axial load and other relevant parameters, are investigated: results are reported in *Chapter 4*.

Thrust bearing also influences the lateral dynamics. Since the collar is fixed to the shaft, it moves with the shaft, which is described by five *dofs*, as illustrated in the *Figure 2.8* (the axial displacement, along the *y*-axis, is omitted).

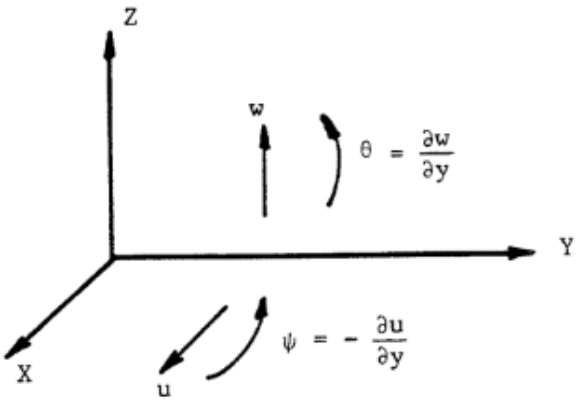

Figure 2.8: Lalanne reference frame [16]

Although the Reynolds equation also depends on shaft angular velocity, this parameter is not treated as a degree of freedom in the present analysis, as it remains constant throughout.

Rotations have a significant impact on oil film distribution and thickness along the circumferential direction. When the collar rotates around the *x* or *z* axis, even with small angular displacements (on the order of 10^{-5} rad), the oil film and resulting pressure distribution lose axial symmetry, as shown in *Figure 2.9*. Therefore, non-negligible moments develop and act on the collar. Forces in the *x* and *z* directions are also present, but they are small enough to be neglected in this model.

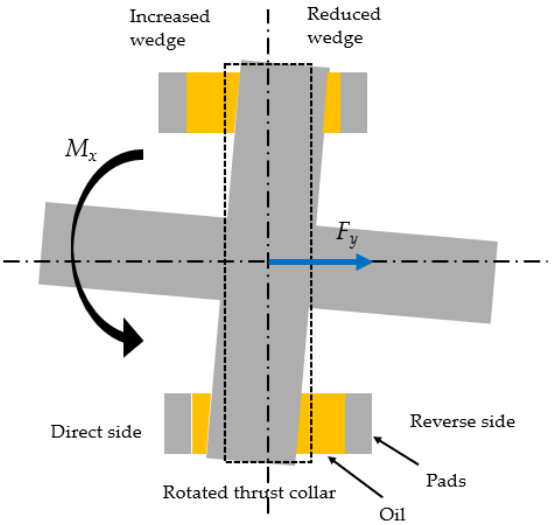

Figure 2.9: Oil film distribution due to collar rotation

To account for this effect, the linear model includes additional off-diagonal terms in the stiffness and damping matrices (such as $K_{y\theta}$ $K_{y\psi}$…) at the positions corresponding to collar rotations and axial displacement, and to their respective derivatives. In the nonlinear model, the hydrodynamic force vector includes non-zero components in the entries associated with these *dofs*.

2.3 Equalizing thrust bearings

As explained, the collar follows the shaft motion, including the rotations of the node where it is mounted, as depicted in *Figure 2.10*. When the collar and the pads are not parallel, non-negligible moments arise. This phenomenon is common and can significantly affect the dynamics of the entire machine.

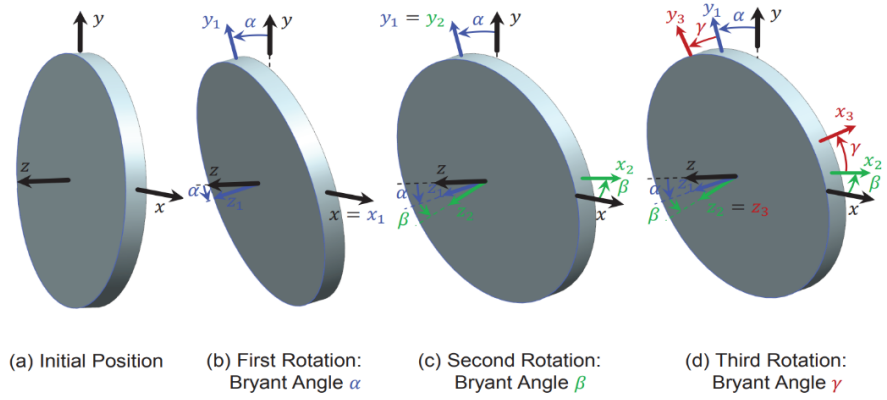

Figure 2.10: Collar rotation

Self-levelling axial bearings feature a specific design to partially address uneven pressure distribution caused by lateral displacements and shaft line weight–induced rotations. These bearings adjust the pad positions to accommodate the shaft's static deflection, thereby reducing the misalignment angle between the collar and pads. Today, they are nearly standard equipment in turbomachinery. As a reference, the collar rotation ϑ due to weight is about 10^{-4} rad. In *Figure 2.11* the vertical displacement and the angular rotation of the shaft line is reported for the machine considered in the thesis.

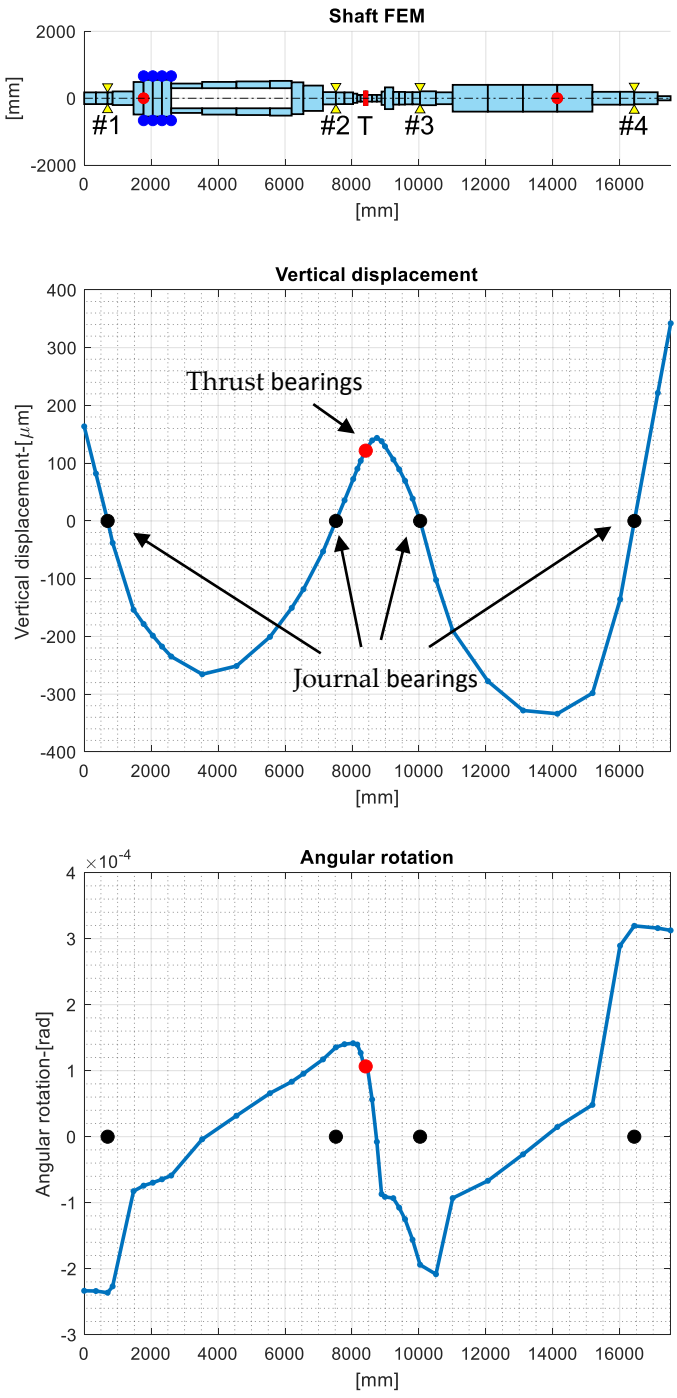

Figure 2.11: Static deflection due to weight

Basically, the pivot, around which the pad can tilt, is not fixed to the bearing case, but is supported by a movable system of equalizing levers, able to adjust pads position according to the load acting on each single pad. This mechanism, represented in *Figure 2.12*, is therefore able to maintain a constant oil film thickness.

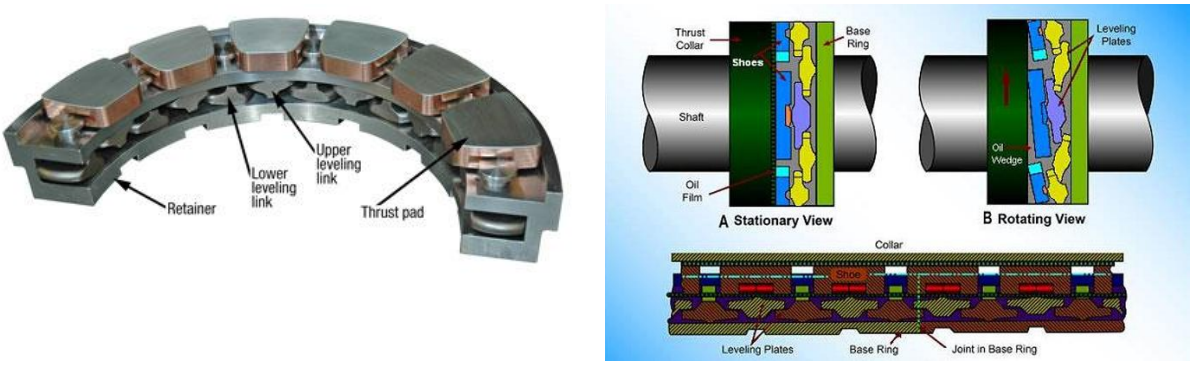

(a) (b)

Figure 2.12: (a) Self levelling thrust bearing; (b) particular of the mechanism

In this work, since collar rotation could play a key role in the coupling mechanism according to [15] and in order to highlight this effect, the *self-levelling* arrangement is completely neglected on both the direct and reverse sides.

2.4 Thrust bearing used in the model

The thrust bearings analysed in this model are tilting-pad, non-self-levelling types mounted on the same collar in a front-to-front configuration. The direct thrust bearing (*Figure 2.13a*) has 11 pads that tilt around a pivot line, while the reverse bearing (*Figure 2.13b*) has 18 pads of the same design. The runner outer diameter measures 400 mm, and the total axial clearance, the distance between the two thrust bearings, is 350 μm, excluding the collar thickness.

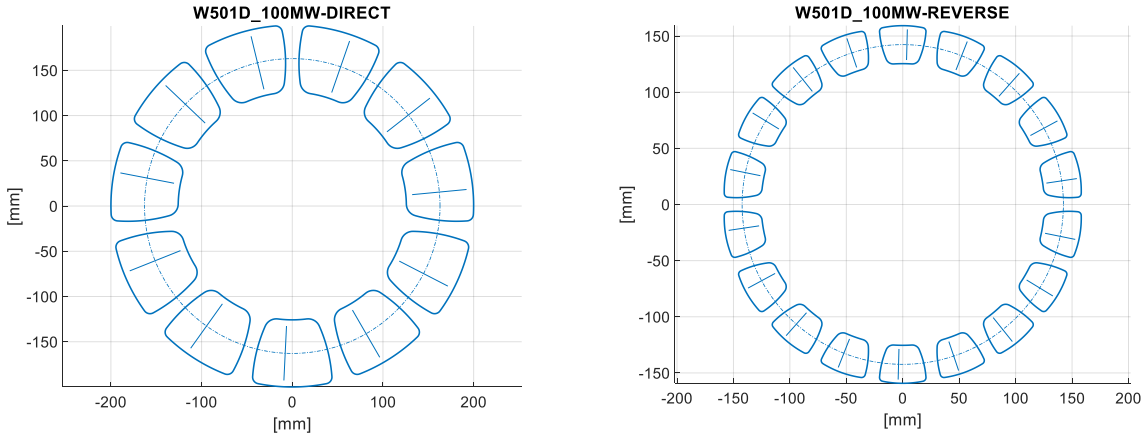

(a) (b)

Figure 2.13: Geometry of thrust bearing analysed: (a) direct side; (b) reverse side

3 Fluid dynamic model

3.1 Theoretical approach

Hydrodynamic lubrication occurs when a highly viscous fluid, such as oil, flows between two nonparallel surfaces in relative motion, according to Williams in [17]. This flow generates a pressure distribution within the fluid film, producing a separating force called the hydrodynamic lift force that acts on the surfaces and prevents direct contact. No pumps are required for this purpose.

At the start of operation, the pad and the runner are almost parallel or only slightly inclined. However, once the runner begins to rotate, the applied load pushes the pad downward, compressing the oil film forming in the gap between the surfaces. Due to the oil's viscosity, the film resists collapsing completely: its thickness cannot drop to zero immediately because the runner's motion drags oil into the gap. This relative movement, combined with the oil's viscosity, creates pressure within the lubricant film that is unevenly distributed, with higher pressure at the trailing edge. This uneven pressure produces a moment on the pad, causing it to tilt slightly around its pivot. As the pad's inclination increases, a wedge-shaped gap forms where the oil film gradually thins in one direction, increasing the hydrodynamic pressure. When this pressure balances the applied load, the pad reaches a stable equilibrium position. Essentially, the system is self-regulating: the pad automatically adjusts its angle in response to the load and oil flow, forming the wedge-shaped film needed to support the load. When one surface is stationary and the other moves, as in bearing runner-pad system, the motion of the moving surface alone draws the viscous fluid into the narrow clearance between them, creating this lubricating film without any external pumping.

This process can be modelled using Reynolds equation, under the assumption of [18]:

1. Newtonian fluid: i.e. shear stress depends linearly in the velocity gradient through a viscosity coefficient μ
2. Incompressible fluid: i.e. density ρ is constant in space and time
3. Laminar flow, evaluated on the basis of Reynolds number
4. Inertia and body forces (e. g. weight) neglected
5. Constant viscosity, meaning it does not depend on pressure or temperature.

Reynolds equation is essentially obtained, for an infinitesimal fluid element, by imposing:

- Continuity:

$$\frac{d}{dt}m = 0 \tag{3.1}$$

which becomes, if it holds hp 2)

$$\nabla \cdot v = 0 \tag{3.2}$$

- and momentum balance, if it holds hp 1), 4), 5):

$$\nabla P = -\mu \nabla^2 v \tag{3.3}$$

Integrating these differential equations imposing constant pressure at boundaries, considering a laminar flow for hp 3) and simplifying at 2D case, velocity profile inside the gap is obtained and, imposing continuity, Reynolds equation is obtained in this form:

$$\frac{\partial}{\partial x}\left(h^3 \frac{\partial P}{\partial x}\right) + \frac{\partial}{\partial z}\left(h^3 \frac{\partial P}{\partial z}\right) = 6\mu U \frac{\partial h}{\partial x} + 12\mu W \tag{3.4}$$

U refers to the tangential velocity of the moving surface relative to the stationary one, evaluated at the mean diameter. This is the main component responsible for dragging the lubricant into the wedge, generating pressure. W represents the squeeze velocity, that is, the rate at which the film thickness h changes with time $\frac{dh}{dt}$. It corresponds to the relative normal speed between the two surfaces and indicates how quickly they move toward or away from each other, causing compression or expansion of the lubricant film.

This equation must be solved for each pad of the bearing. The variable h represents the oil film thickness between any pad and the runner, which depends on the spatial

coordinates x and z locally defined for each pad, implying that the surfaces are not parallel.

When the bearing geometry is known, which means that $h(x,z)$ and other dimensions are known, pressure distribution is determined. A detailed derivation of this equation can be found in [18].

Thus, separating force is obtained by integrating pressure distribution P obtained by solving $F = \iint_S P(x,z)\, dS$ (3.5) on the whole surface:

$$F = \iint_S P(x,z)\, dS \tag{3.5}$$

Also tangential force (responsible of power loss) is obtained, by integrating shear stress from Newton relation:

$$T = \int_0^L \mu \frac{\partial v}{\partial y}|_{wall}\, dx \tag{3.6}$$

Figure 3.1 is a schematic representation of the quantities of interest in the case of a thrust bearing.

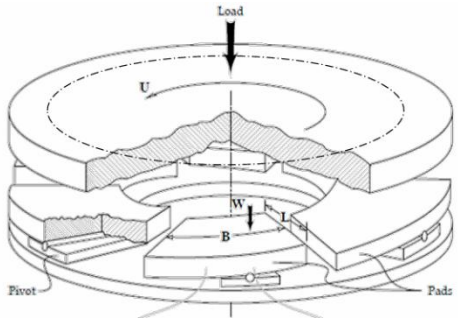

Figure 3.1: Simplified geometry of a thrust bearing

A critical discussion must be performed regarding Reynolds assumptions. Hp 1), 2) and 4) are generally well aligned with physical reality when dealing with highly viscous fluids such as lubricating oil. In actual operating conditions, however, the flow field is inherently 3D, which makes hypothesis 3) theoretically inconsistent. Nonetheless, since h is typically on the order of a few hundred microns and therefore much smaller than the other characteristic dimensions of the geometry, the gradients in the transverse direction become negligible. This justifies the adoption of a 2D flow approximation, which is often acceptable in industrial applications depending on the desired level of accuracy. On the other hand, hypothesis 5) represents the strongest assumption and the one most distant from the actual physical behaviour of the system. This becomes particularly evident when the Reynolds number falls below a

critical threshold, which is typically defined by the geometry and lies between 100 and 1000.

In such cases, the flow remains within the laminar regime. This condition can be expressed as $Re = \frac{\rho U h}{\mu} < Re_{cr}$, where μ is the dynamic viscosity of the oil, ρ its density, h the oil film thickness and U the relative velocity between the surfaces.

Under standard operating conditions, the viscosity is generally high and the film thickness is small, so the laminar assumption is often satisfied. However, h may increase in certain regions, for example when the collar moves far away from a pad, and simultaneously the viscosity may decrease due to localized heating.

As the oil moves through the bearing, viscous shear causes internal energy dissipation, which leads to a temperature rise within the film. This temperature increase reduces the viscosity, which in turn diminishes the pressure generation capability of the lubricant and can lower the load-carrying capacity of the bearing. The variation of the viscosity against temperature is shown in *Figure 3.2*. Neglecting this effect by assuming constant viscosity can introduce significant errors in performance prediction. For this reason, the computational model developed in this work allows the user to either assume constant viscosity using a Hydrodynamic (HD) approach, also called *isothermal model*, or to consider temperature effects through a Thermohydrodynamic (THD) model.

The Hydrodynamic (HD) model does not consider temperature effects and assumes rigid surfaces for both the runner and the pads. It does not involve solving any energy balance. Assuming a fixed temperature can be reasonable when operating speeds are not very high, such as in turbochargers, where oil heating due to friction is significant. This is the approach used in the current work.

The Thermohydrodynamic (THD) model enhances the classical Hydrodynamic (HD) approach by introducing the effects of temperature through an energy balance for each pad (3.7).

$$\rho c_p \left(U \frac{\partial T}{\partial x} + W \frac{\partial T}{\partial z} \right) = k_{oil} \left(\frac{\partial^2 T}{\partial x^2} + \frac{\partial^2 T}{\partial z^2} \right) + \mu \left[\left(\frac{\partial u}{\partial y} \right)^2 + \left(\frac{\partial w}{\partial y} \right)^2 \right] \tag{3.7}$$

ρ, c_p, k_{oil}, μ represent the mass density, the specific heat capacity, the thermal conductivity and the viscosity of the oil, respectively. x and z (parallel to the pad surface) and y (orthogonal to the pad surface) are the coordinates of the pad reference frame. u and w are the components of the oil velocity parallel to x and z, respectively. U and W are the average values of u and w, computed as following:

$$U = -\frac{h^2}{12\mu}\frac{\partial P}{\partial x} + \frac{1}{2}(U_1 + U_2) \text{ and } W = -\frac{h^2}{12\mu}\frac{\partial P}{\partial z} \quad (3.8)$$

where h is the oil film thickness.

Equation (3.7) accounts for the heat produced by viscous shear within the lubricant and must be integrated with the thermal exchange with the surrounding components. This results in a more realistic representation of the lubrication regime, especially when operating conditions involve significant thermal variations.

The procedure begins with the definition of the system geometry, the operating parameters such as the position and velocity of the runner, and the initial temperature of the lubricant, which is generally set equal to the inlet value. Based on this initial temperature, the viscosity of the fluid is calculated, as it depends strongly on thermal conditions. This viscosity is then used in the solution of the Reynolds equation to determine the pressure distribution across the oil film.

Once the pressure field is obtained, the energy equation is solved to update the temperature distribution. This step considers the heat generated by internal friction and the transfer of heat to and from the bearing surfaces. The outcome is a revised temperature field over the surface of the pad.

Using the new temperature values, the viscosity is recalculated. The algorithm then solves the Reynolds equation again with the updated viscosity. After each cycle, the pressure and temperature fields are compared with those from the previous iteration. If the changes between successive results fall below a predefined threshold, the process is considered to have reached convergence.

This iterative method continues until the computed values for pressure and temperature stabilize. At that point, the solution reflects a thermally consistent and physically accurate model of the lubricant film, capturing the key interactions between fluid dynamics and heat transfer. *Figure 3.3* illustrates two of typical outputs of this solution, in particular pressure and oil film thickness over the bearing.

The code used here can also perform the analysis according to this hypothesis or not, being capable of solving modified Reynolds equation. A modified Reynolds equation is an extended or modified form of the classical Reynolds equation that incorporates more complex effects or more realistic conditions compared to the standard version. Such extensions may include, for example:

- Variations in viscosity due to pressure or temperature (non-constant viscosity)
- Effects of non-Newtonian fluids, where the relationship between shear stress and velocity gradient is nonlinear

- Compressibility effects, involving variable fluid density
- Turbulence effects and three-dimensional flow
- Advanced cavitation phenomena

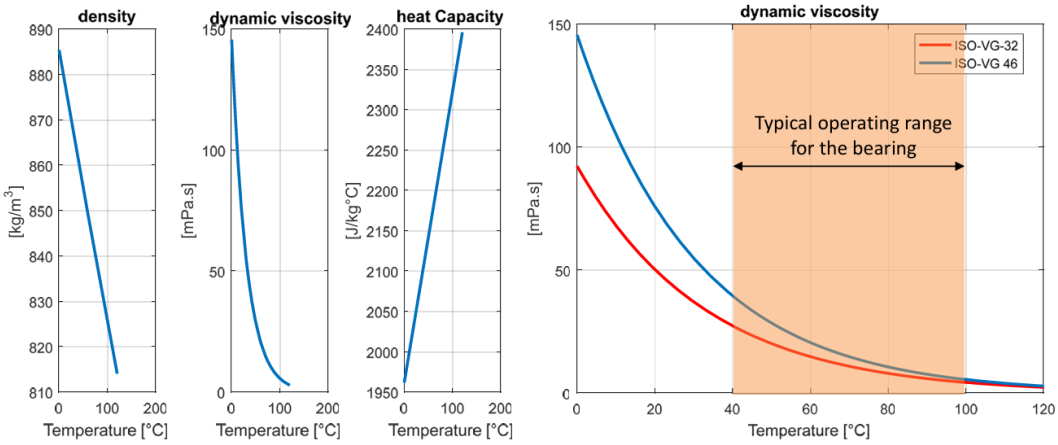

Figure 3.2: (a) density, viscosity and heat capacity of lubricant as a function of temperature; (b) particular of dynamic viscosity as a function of temperature

Cavitation is handled in the code using linear complementary problem method, which divides the domain in an active region where pressure is positive and the density is set to its nominal value, and in a cavitated one where the pressure is set to zero and the density is lowered. In the thrust bearing analysed here, cavitation has little impact on the pressure field. This is mainly due to the geometry of the film, which promotes a stable converging shape, and the relatively low sliding velocities W typical of these operating conditions, which tend to depressurize the oil sometimes, in particular when directed moving away from pads.

Operating under flooded conditions further reduces starvation risk. A continuous lubricant supply ensures full film coverage, preventing the development of low-pressure zones. The complete immersion of the pad raises the static inlet pressure, which helps counteract pressure drops along the pad and prevents local depressurization below the vapor threshold.

A stable oil supply also improves cooling. By limiting temperature variations within the film, viscosity remains more uniform, supporting a consistent pressure distribution. Together, these factors contribute to a stable and reliable lubrication regime.

At very high rotational speeds, such as those in turbochargers, centrifugal forces can shift the lubricant outward. This alters the film profile and affects local pressure and

temperature, potentially reducing load capacity and inducing also cavitation in inner zones. However, the effect is very small even in turbochargers, as reported also by [13] and can be here totally neglected.

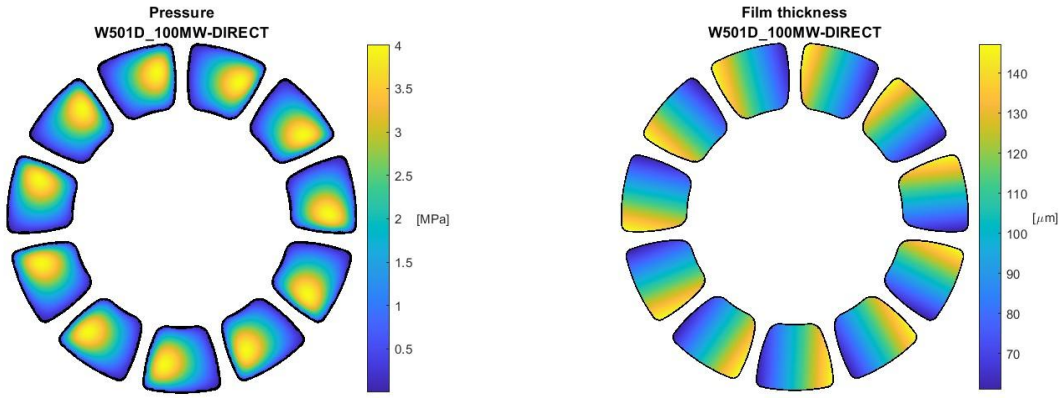

(a) (b)

Figure 3.3: Direct side: (a) pressure distribution; (b) film thickness

3.2 Fluid dynamic model: inputs and outputs

The core of this work is to evaluate the role played by the thrust bearing when coupled lateral and axial vibrations are observed, as done by Tian et al. in [19]. Fluid dynamic forces generated by the TB acting on the collar mounted on the shaft are incorporated into the rotordynamic model described in *Chapter 5.2* as external forces at the right side of the equation of motion. A schematic representation of inputs and outputs of the MATLAB code is shown in *Figure 3.4*. This kind of forces are definitely nonlinear as derived applying Reynolds theory and depend in principle on:

- Collar axial position, y
- Collar rotations around x and z axis, respectively ϑ and ψ, in *Figure 3.5*
- Derivative with respect to time of said position and rotations
- Rotating speed of the machine, Ω
- Oil inlet temperature, T

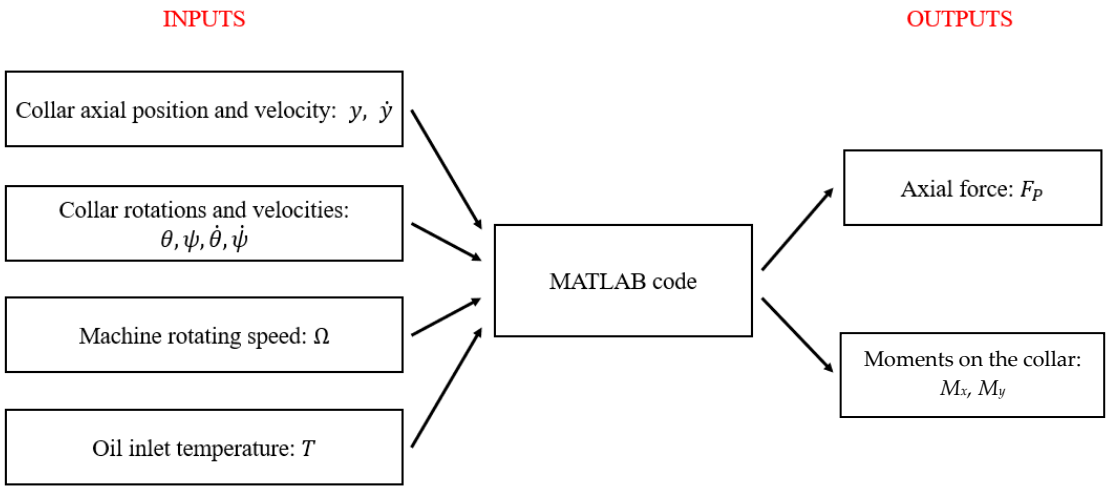

Figure 3.4: Input and output parameters of MATLAB code used

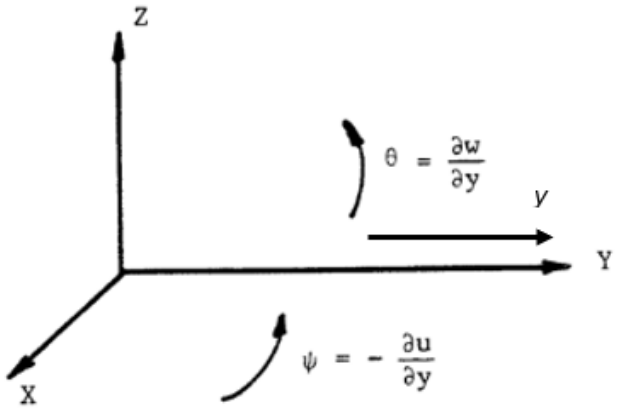

Figure 3.5: Lalanne reference frame [16]

To reduce the complexity of the analysis, the rotational speed is kept constant at 3600 rpm, even though it plays a significant role in oil pressurization during startup. This choice is justified by the fact that the turbine operates at this nominal speed under steady-state conditions, and vibration issues related to the SSV are typically not observed during transient phases, but rather at constant speed. In particular, SSV are large during the changes of machine active power load, which corresponds to a change in the axial load. Additionally, the oil inlet temperature is fixed at 45°C, supposing LEG type oil feeding system. However, for the application of the hydrodynamic (HD) model, a mean oil temperature of 60°C is considered, as the average exit temperature at the trailing edge of each pad is approximately 80°C. Another simplifying assumption in the simplified model is the omission of pad dynamics. Each pad is assumed to remain in static equilibrium with the runner at

every runner configuration, with no residual angular velocity about its pivot. This equilibrium is reached when the hydrodynamic force acting on the pad passes through its pivot line (it should be noted that this force acts on both the runner and the pads, pushing both). This assumption is considered reasonable because the pads respond at frequencies much higher than those of the runner. While the runner typically operates around 60 Hz or within the range of its dominant vibration modes, the pads exhibit dynamic behaviour at several hundred Hz. Consequently, the pads can adjust almost instantaneously to changes in the runner's state.

This simplification reduces the computational time of simulating the pads during integration but limits the model's ability to capture more complex dynamic phenomena, such as pad flutter or fluid film instabilities. To address this limitation, an extended version of the computational code has been considered. This enhanced version includes the pad dynamics, computing the same output variables while also determining the moments acting on the pads, based on the runner's state as well as the pads' angular positions and velocities around their pivots. Rather than guessing and iteratively solving for the oil film thickness distribution, the film thickness is directly obtained from the actual geometrical configuration. A brief introduction to how this formulation can be incorporated into the equations of motion, along with a discussion on its potential and implementation perspectives, is presented in *Chapter 10*. It should also be noted that there is a trade-off between including pad dynamics or neglecting them. Although considering pad dynamics requires simulating an additional 29 variables, the simulation time for a single runner-pads configuration is much faster compared to the iterative process of finding pad equilibrium, often taking around five to six seconds. Therefore, this trade-off must be carefully evaluated. Another limitation of including pad dynamics is that it introduces stiffness into the system due to the significantly different dynamic response times of the pads and the runner. This stiffness complicates numerical convergence and necessitates smaller time steps when using solvers like ode45. As a result, more robust but intrinsically less accurate solvers such as ode23tb, ode23t, or ode15s are often required to ensure stable integration.

A closed-form solution of the Reynolds equation is not available for complex geometries such as those found in a tilting pad thrust bearing, due to the nonlinear dependence of the equation on the oil film thickness h. For this reason, the pressure distribution, along with the resulting fluid dynamic forces and moments, is determined through a numerical approach implemented in a MATLAB code. This method involves discretizing the surface of each pad into a computational grid and approximating the spatial derivatives using a finite difference scheme.

The code takes as input the position and orientation of the collar, along with their time derivatives, and iteratively solves the Reynolds equation to compute the equilibrium pressure field for each pad.

The computational procedure for each pad begins with an initial estimate of the tilt angle, which defines the local oil film thickness $h(x, z)$ based on the pad's geometry and geometrical consideration of relative position between the runner and the pad. Using this film thickness, the Reynolds equation is solved numerically to obtain the pressure distribution within the lubricant film.

From the pressure and shear stresses distributions, the hydrodynamic forces acting on the pad are calculated by integrating the pressure over its surface area. The resulting moment is then evaluated by considering the offset between the force application point and the pad's pivot location.

Because the film thickness depends on the pad tilt, and the pressure distribution affects the forces that influence the tilt, the process is inherently nonlinear. After each iteration, if the equilibrium condition is not satisfied within a predefined tolerance, the tilt angle is updated (typically through a Newton-Raphson algorithm) and the Reynolds equation is solved again with the updated film thickness.

This iterative loop continues until convergence is reached, meaning the pressure distribution, film thickness, forces, and moments stabilize and the pad reaches equilibrium.

Because the collar is not perfectly aligned but exhibits two angular tilts, the gap between the collar and each pad varies. Consequently, the numerical solution must be performed individually for every pad on both the direct and reverse sides of the bearing.

The outputs of the code are:

- total net force *Fp*, calculated as the sum, considering sign, of all the forces of every pad, both of the reverse side and the direct one
- moments of the above-mentioned forces on x and z axis, respectively Mx and Mz

Any moment acting around the shaft's axis of rotation is not considered, as shaft torsional dynamics are neglected in the present analysis. Similarly, the radial force components along the x and z axes are assumed negligible due to their relatively small magnitude.

It is possible to visualize the distributions of temperature, pressure, and oil film thickness across the pads on both bearing sides. The code also provides the tilt angles

of the equilibrium positions reached by the individual pads. Moreover, the model can determine the equilibrium position of the system for assigned runner tilts by idealizing an axial displacement of the runner until the externally applied axial load is fully balanced and the velocities vanish. Once this equilibrium condition is achieved, the code allows the computation of linearized stiffness and damping coefficients. These coefficients, which describe the fluid dynamic response of the thrust bearing, are presented and discussed in *Chapter 4*. Computing linearized coefficients and equilibrium position requires some minutes, depending strongly on configuration and load.

It is worth to say that three different approaches can be used to compute the oil wedge temperature distribution over the pads.

1. The temperature is assumed to be constant across the entire pad surface and equal to the oil inlet temperature, which is set by the user.
2. The temperature is assumed to vary linearly along the direction of oil flow, from the inlet to the outlet, with both boundary temperatures defined by the user. To be consistent with model 1, an inlet temperature of 45 °C and an exit temperature of 120 °C for each pad can be assumed.
3. The temperature distribution is computed by the code itself through an energy balance, considering heat exchange within the oil film. This involves coupling a partial differential equation (PDE) to the Reynolds equation and solving the extended system numerically. The pad inlet temperature can be set at 45 °C, while the trailing edge temperature is then computed by the solver.

These three modes are listed in order of increasing accuracy and computational cost. As a reference, using a PC with 8 GB of RAM and a quad-core CPU operating at 2 GHz, the simulation of a single configuration, defined by specific positions and velocities, takes approximately 60 s in mode 1. In mode 2, where a linear temperature gradient is applied, the average simulation time increases slightly to around 1 min and 30 s. Mode 3, which includes full thermal modelling through the coupled energy balance, requires about 7 min per configuration due to the added computational complexity.

Transient simulations often result in significantly longer computation times, potentially lasting several days or even weeks, depending on the number of function evaluations required by the numerical integration scheme. For instance, simulating band-limited axial noise over an 11-second interval may require up to 250,000 solver calls within the ODE function. This aspect must be carefully considered when setting up long transient simulations to avoid excessive computational demand.

4 Results of fluid dynamic model

As already explained in *Chapter 3,* the pressure in the oil film generates forces on the runner, with the main resultants being F_y and the two moments M_x and M_z. Each of these are governed respectively by three different functions of the same six independent variables $(y, \vartheta, \psi, v_y, \dot{\vartheta}, \dot{\psi})$. Conceptualizing their behaviour and understanding the simultaneous influence of all parameters is complex. However, under certain conditions, specific input variables exhibit negligible influence on the system response. Mathematically, this corresponds to a vanishing partial derivative of the function with respect to those variables.

The interesting configurations are simulated, with the purpose of isolating and evaluating the sensitivity of the system with respect to key parameters. The following cases are analysed:

1) Force and moments, varying the axial displacement y and the angular tilt of the runner with respect to x axis, denoted with ϑ.
2) Force and moments, varying the axial displacements y and both ϑ and ψ.
3) Force and moments, varying the angular tilt ϑ and $\dot{\vartheta}$.

Plots provided in the following pages represent force and moments as a function of several key variables, while keeping the other ones fixed, as listed above.

4.1 Axial force and moments varying y and ϑ

The main purpose of this analysis is to understand how the axial force varies nonlinearly with axial displacement, as this direct contribution along the force direction is expected to have a significant influence, showing rather pronounced gradients at the extremities. Additionally, the objective is also to highlight the coupling effect introduced by the thrust bearing, since any rotation can also affect and modify the axial load and any axial displacement is able to change the value of the moment applied to the collar. The final goal is to highlight that, although with

small values in magnitude, the rotation about x axis is able to generate a moment in z axis.

Figure 4.1a shows the axial force as a function of axial displacement y and angular tilt ϑ. When the angular tilt is held constant, the magnitude of the force increases as the runner is displaced either to the left or right. Specifically, displacement in the positive direction (close to reverse side) results in a decrease in force (reverse side pushes the collar on the left), whereas displacement in the negative direction leads to an increase. Notably, the direct side generates significantly higher forces compared to the reverse side.

Asymmetric design of the bearing results in an asymmetric force generation. Thus, the zero-displacement position, located at the centre of the clearance, does not correspond to a zero-force condition. For example, with an angular tilt of 10^{-4} rad, a displacement of approximately 78 μm is necessary to make the net force null. The total axial clearance is 350 μm, with the zero-value placed in the middle of the clearance itself, as shown in *Figure 7.2*; direct side is on the left and reverse side is on the right.

The force exhibits a more limited but non-negligible dependence on ϑ with respect to y. Since both the direct and reverse sides are pressurized under a given tilt, the resulting force depends on which side contributes more effectively. Within the displacement range of approximately 42 to 58 μm, the force becomes largely insensitive to changes in angular tilt. Beyond this range, moving towards 160 μm, the force decreases with increasing tilt. This occurs because the angular tilt reduces the lubricant film thickness more significantly on the reverse side than on the direct side. Conversely, on the direct side, a given tilt results in a greater force response than on the reverse side. Even when the runner is centered at zero displacement, the presence of an angular tilt increases the net force due to the higher force contribution from the direct side. Finally, it is clear that as the motion moves toward either the direct or reverse direction, the range of allowed rotations decreases. From the diagram, the number of feasible points is reduced accordingly, with only two or three points remaining when the axial displacement is large in magnitude. This phenomenon is explained in *Chapter 7.3* .

Figure 4.1b shows the moment M_x as a function of y and ϑ. For $\vartheta = 0$, when the fluid film is uniformly distributed, no moment is observed. The moment behaves as an odd function with respect to the angular displacement ϑ, for a fixed axial displacement y. This behavior arises from the geometric symmetry of the two sides of the thrust collar about the x axis.
For a fixed ϑ, the magnitude of the moment increases as the displacement moves toward either the direct or the reverse side.

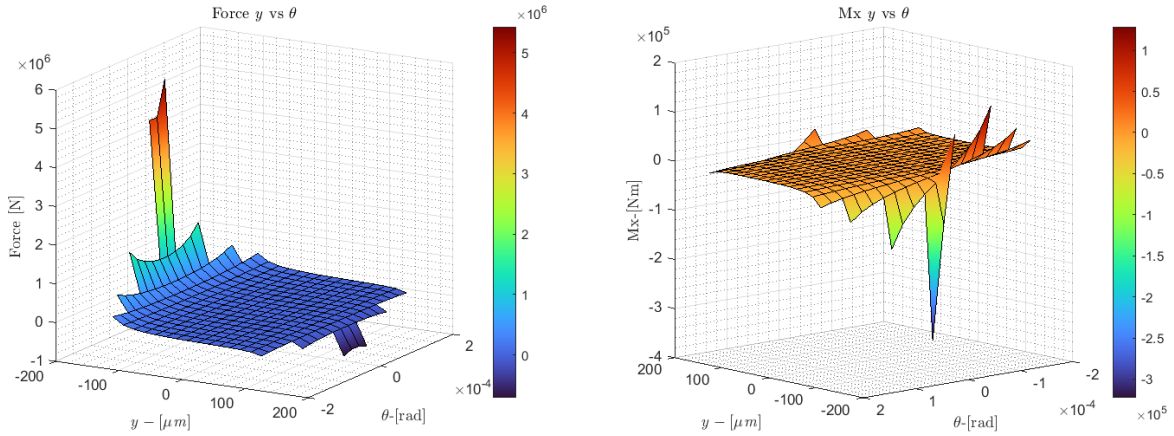

(a) (b)

Figure 4.1: (a) F_y vs y and ϑ and (b) M_x vs y and ϑ

Figure 4.2a is extracted from *Figure 4.1b* and shows M_x as a function of ϑ when $y = -126$ µm. The sign of the moment depends on the sign of the rotation: specifically, a positive rotation induces a negative moment, and conversely, a negative rotation produces a positive moment.

Figure 4.2b is extracted from *Figure 4.1b* and shows M_x as a function of y when $\vartheta = 1 \cdot 10^{-5}$ rad. Displacement toward the direct side results in higher moment values due to the increased load acting on the runner. The curve appears mirrored when $\vartheta = -1 \cdot 10^{-5}$ rad is considered.

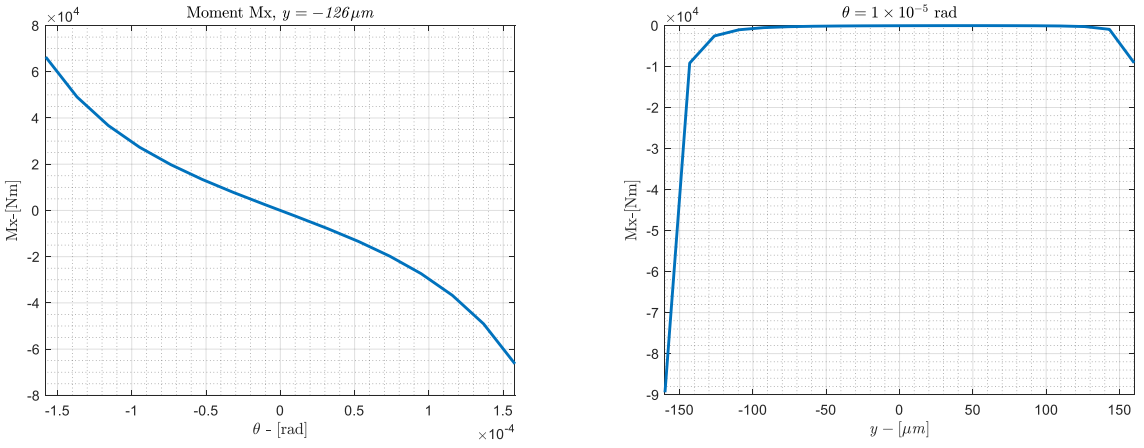

(a) (b)

Figure 4.2: (a) $M_x$vs ϑ, fixing y and (b) M_x vs y, fixing ϑ

Figure 4.3 shows M_z (orthogonal to M_x) as a function of the same variables y and ϑ. Clearly, the magnitude of the moments is relatively small, as the coupling between a rotation and the moment in a direction orthogonal to that rotation is weak. Nevertheless, the behaviour concerning both trends and sign is consistent with those of the *Mx* moments. Similar considerations can be done for changes of angle ψ.

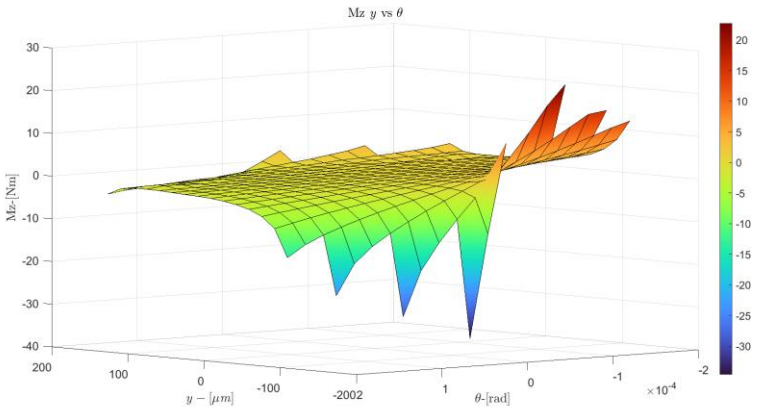

Figure 4.3: M_z vs y and ϑ

4.2 Axial force and moments varying y, ϑ and ψ

The objective in this case is to highlight the axial symmetry of the thrust bearing. This analysis also reinforces the findings presented in the previous two case studies. The symmetry is so pronounced that, for a given thrust spatial configuration, the two rotations and the corresponding moments about the x and z axes in quadrature, and correlating the resultant moment with the derived equivalent angle, the results closely match those obtained in *Chapter 4.1* and *Chapter 4.3*.

Assigning a displacement and two rotations is feasible only within a limited domain, as the system state cannot assume arbitrary values, because admissible rotations and axial displacement are not independent. This constraint will be further discussed in *Chapter* 7. The space of permissible parameter combinations can be visualized as a three-dimensional barrel-shaped region in *Figure 4.4*.

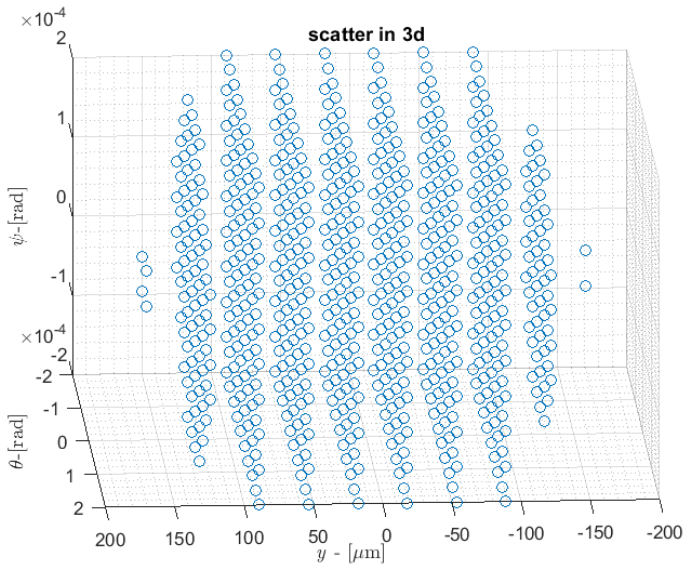

Figure 4.4: permissible combinations y and ϑ

To make the analysis clearer and reduce the total number of independent variables without distorting the plots, a new moment is defined as the magnitude of vectorial sum of M_x and M_z:

$$M_{quad} = \sqrt{M_x^2 + M_x^2} \tag{4.1}$$

Similarly, a new tilting angle is defined, accounting for both ϑ and ψ:

$$\vartheta_{quad} = \sqrt{\vartheta^2 + \psi^2} \tag{4.2}$$

Because of the definition, M_{quad} and ϑ_{quad} are strictly non-negative.

Figure 4.5a shows the force as a function of y and ϑ_{quad}. As in *Figure 4.1*, the nonlinear and asymmetric dependence of the force with respect to y is evident. High values of the force are observed approaching the direct side, while toward the reverse side the force assumes smaller values. Increasing the value of ϑ_{quad}, the allowable axial displacement reduces together with the magnitude of the force.

Concerning ϑ_{quad}, the dependence of the force on it is weak. Because of the asymmetric design of the bearing, increasing the rotation ϑ_{quad}, a net axial force is generated, even not significant, as explained in *Chapter 4.1.*

Figure 4.5b shows the moment M_{quad} as a function of y and ϑ_{quad} and can be compared with *Figure 4.1.* Only the positive side of the diagram relative to the vertical axis should be considered here, as the focus is on the correlation between the magnitude of any rotation and the corresponding moment magnitude. Larger rotation values are possible when combining rotations in quadrature compared to

the limit of a single rotation alone. Therefore, the limit value is not simply $2 \cdot 10^{-4}$ rad as in the two cases in *Chapter 4.1* and *Chapter 4.2*, but can be higher.

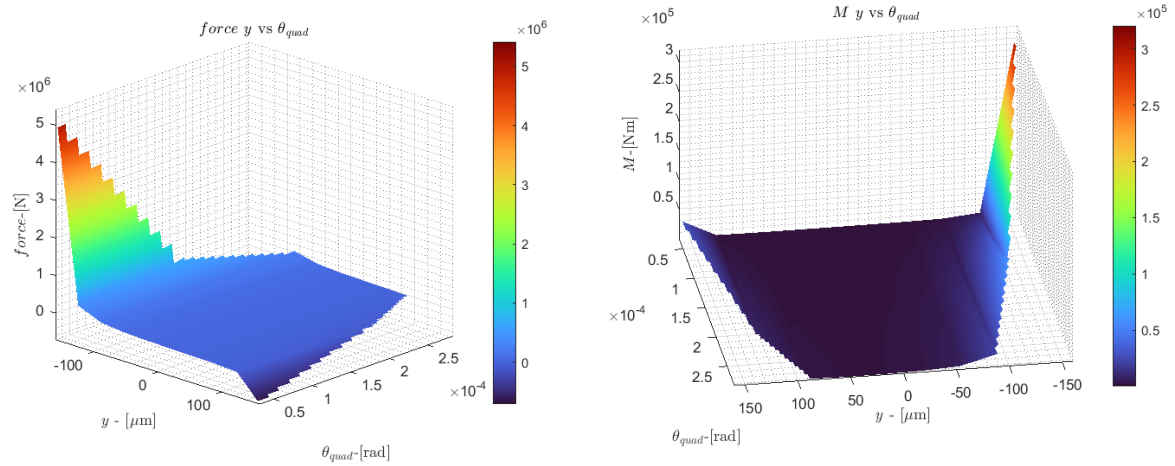

(a) (b)

Figure 4.5: (a) F_y vs y and ϑ_{quad} and (b) M_{quad} vs y and ϑ_{quad}

4.3 Axial force and moments varying ϑ and $\dot{\vartheta}$

Any moment generally depends more strongly on the rotation about the same axis, as previously noted. However, the velocity $\dot{\vartheta}$ also plays a significant role. The purpose of this analysis is to estimate the order of magnitude of the influence that these direct terms have on the moment and to further emphasize the coupled behaviour. This is especially relevant because net axial forces of several thousand Newtons can arise at positions where the net axial force is nearly zero when rotations are absent.

Figure 4.6a shows the axial force as a function of ϑ and $\dot{\vartheta}$, fixing: $y = 78$ µm. The force versus $\dot{\vartheta}$ relationship exhibits an approximately linear behaviour, with the slope depending on the sign of the angular rotation: a negative rotation corresponds to a positive slope, and viceversa.
When $\dot{\vartheta} = 0$, the force as a function of ϑ is consistently negative, reflecting the dominant response of the reverse side. When angular velocity is held constant, the force versus angular displacement curve is approximately parabolic, with steeper gradients at higher magnitudes of rotation. The combined effect of positive angular velocities and rotations significantly amplifies these gradients. Additionally, it is noteworthy that this behaviour is symmetric about a 45° inclined line in the force-angular velocity plane.

This is because the chosen direction moves towards the direct thrust side, allowing a better appreciation of the restoring moments. The moment increases with both increasing θ and $\dot{\theta}$, indicating that they have a similar effect. The minimum and maximum magnitudes are observed at the extremes.

It can also be noted that one effect tends to flatten the other when one is positive and the other is negative: beyond a certain point, the moment no longer increases for large positive angles combined with very negative angular velocities, and vice versa. This indicates that the effects of relative position or runner with respect to pad and squeeze velocities of oil film thicknesses are equally important, both having the ability to flatten the trend once a certain threshold is surpassed.

The trend is linear for any fixed rotation: as the angular velocity increases, the moment decreases at all angular displacements. Similarly, the dependence on ϑ is approximately linear under these conditions.

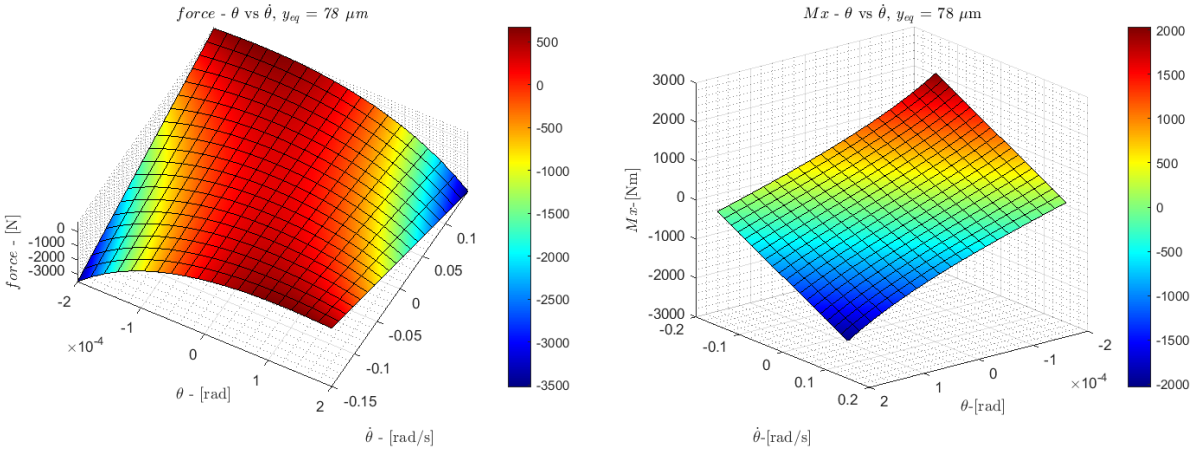

(a) (b)

Figure 4.6: (a) F_y vs ϑ and $\dot{\vartheta}$ and (b) M_x vs ϑ and $\dot{\vartheta}$

5 Rotordynamic model

5.1 Machine description

Although the SSV phenomenon appears in various machines, from small turbochargers to large industrial turbines, this numerical analysis investigates a medium-scale gas turbine with a nominal power output of 100 MW, representative of models such as the Westinghouse W501D. The following section outlines the main technical features of the machine to support the development of the numerical model discussed in the subsequent chapters.

The turbine features a continuous steel shaft measuring 17 m in length. From left to right, with respect to the *Figure 5.1*, the shaft carries a four-stage turbine, a combustor, a compressor, the rotor of an electric generator (not illustrated), and an exciter unit (also not shown), which engages during startup. The relevant engine parameters are reported in *Table 5.1*. The engine is supported by four journal tilting pads bearings and one tilting pads double-sided thrust bearing, placed between the compressor and the generator. Since it is designed for the American electric grid, the rotating speed is 3600 rpm (60 Hz). The model assumes the presence of a residual nominal unbalance in the rotor. Supporting structure is totally neglected in the following analysis and the case deformation is not considered for the dynamic simulation.

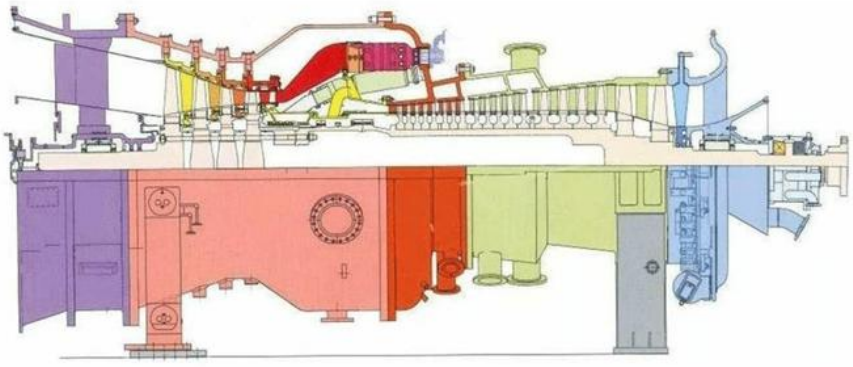

Figure 5.1: W501D machine: particular of turbine and compressor

Rotor length [m]	17.52
Power [MW]	~100
Number of turbine stages	4
Number of compressor stages	18
Number of journal bearings	4
Number of thrust bearings	1
Rotational speed [rpm]	3600
Rotor mass [kg]	48 758

Table 5.1: Main engine parameters of modelled gas turbine

5.2 Rotordynamic model

The standard rotordynamic model computes the displacements and rotations at selected points of interest as functions of time by solving a set of second-order differential equations that incorporate all relevant force contributions, particularly:

1. Inertial forces, which vary linearly with the second derivative of displacement, namely acceleration.
2. Damping forces, gyroscopic effects, and certain aerodynamic components, which vary linearly with the first derivative of displacement, referred to as velocity.
3. Elastic restoring forces, including shaft stiffness, linearized bearing coefficients, Alford forces, and similar contributions, which vary linearly with the displacement.
4. Additional forces that do not fall into the previous categories, such as those independent of displacement and its derivatives (e.g., weight) or those exhibiting nonlinear behaviour (e.g., hydrodynamic forces generated within the bearing fluid film).

Summing all the contributions listed above produces a set of second-order differential equations, known as the equations of motion. These equations hold fundamental importance as they express the governing law that describes the system evolution. The model outputs the generalized displacements, expressed in terms of amplitude and phase (direction).

In the present work, only a subset of the contributions listed above is considered. Specifically, the effects originating from blades and seals, which introduce some coupling among radial directions and could have a destabilizing effect, are excluded,

as is casing modelling. These simplifications allow focusing on the coupling effect of the thrust bearing and facilitate isolating its influence more effectively.

It is important to acknowledge that linear dependence represents an idealization rarely achieved in real machines. When dealing with nonlinear differential equations, numerical methods generally provide the only viable solution, albeit with a high computational cost. Conversely, adopting linearized coefficients, which remain constant within the operating range considered, accelerates calculations but introduces an approximation error. The choice between linearized and fully nonlinear models depends on the system's degree of linearity, specifically whether assuming small displacements under given excitation is acceptable. If displacements become excessively large, linearity no longer applies, and the resulting approximation error requires evaluation on a case-by-case basis. This work presents two analyses, linear and nonlinear, followed by a detailed comparison of the most relevant results.

5.2.1 FEM model

Finite Element Method (FEM) is a typical technique, very common in industrial fields, to deal with static and dynamic analysis of complex components and structures. A complete mathematical explanation can be found in [16] and [21]. As the name suggests, the method relies in subdividing the structure in a finite number of parts or elements, contrary to the continuous approach, which uses infinite elements infinitesimal. FEM provides always an approximation of the real behaviour of the system (that is continuous), but tends to the real solution increasing the number of elements. In fact, continuous approach is suitable for simple geometries, but difficult to implement for complex ones, with discontinuities, also in terms of materials and properties.

Each element is defined by (two or more) extremity points, called *nodes*. The behaviour of every point inside the element, in terms of displacements and velocities, is described by analytic functions of displacements and velocities of nodes, which are called *degrees of freedom* of the system or *dofs.* Nodal values of displacements and velocities are the only direct outputs of the algorithm.

Many different element types are available in the literature, varying in geometry (beam, triangles, tetrahedrons…) and the functions, known as *shape functions*, describing them (linear, quadratic…). In this work, beam elements (Timoshenko beam) and cubic shape functions are selected, standard choice for rotordynamic models, like the one presented here. An example of element is shown in *Figure 5.2.*

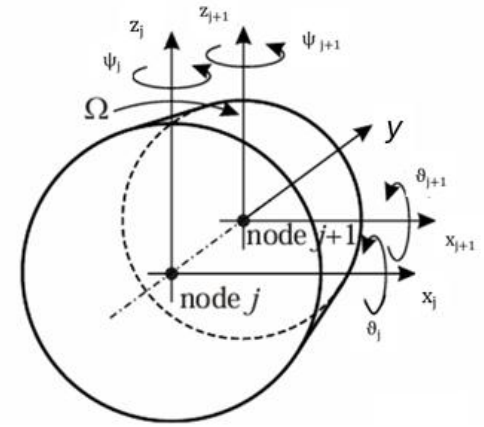

Figure 5.2: Cylindrical FEM element and its degrees of freedom

This kind of element is mono-dimensional, defined by two nodes, each node with 4 *dofs*. Each element must have constant cross section and homogeneous material properties, subjected to shear and bending. The torsional flexibility of the shaft is totally neglected, as the torsional behaviour is decoupled from the axial and radial dynamics for the considered case.

The discretization of the shaft into finite elements follows a specific criterion: a new element is defined at every change in cross-section. However, despite of this condition, an element cannot be longer than a critical length. It worths remember that the right number of elements is a trade-off between accuracy and speed of calculation.

When a beam of this type moves in dynamic equilibrium (i. e. inertia forces are of the same order of magnitude as the elastic forces), displacement functions take the form of an infinite sum of sines and cosines and hyperbolic sines and cosines.

However, numerical algorithms cannot deal with infinite summations, thus another approximation is needed: cubic displacement functions are sufficiently accurate if and only if the element behaves as a rigid body. To ensure this condition, the first natural frequency of the element must be much greater than the one at which the element itself is excited. Mathematically it can be written as:

$$\left(\frac{\pi}{L}\right)^4 \gg \frac{\omega^2}{\frac{EI}{m}} \tag{5.1}$$

where E is the material Young modulus, I is the inertia moment of the section, m is the mass density per unit length, L is the element length; ω is the maximum pulsation in rad/s at which the above approximation is valid, or in other words, the maximum value at which the system is supposed to be excited. For the current case $\omega = 3600$ rpm.

Practically, it means that the length of the element cannot be greater than:

$$L \ll \pi \cdot \sqrt[4]{\frac{EJ}{\omega^2 m}} \tag{5.2}$$

For a circular cross-section, the above expression can be rearranged as following:

$$L \ll \pi \sqrt[4]{\frac{ED^2}{8\omega^2 \rho}} \tag{5.3}$$

where D is the diameter of the section and ρ is the material mass density.

The critical length L is then calculated for each element of the shaft. A safe value of $L = 1000$ mm is then chosen, obtained by applying a safety factor to the smallest computed length among all elements. This value is adopted for every element, resulting in a total of 41 elements.

If two adjacent elements have two diameters very different, a correction of the model proposed is required. The element with the greater diameter cannot store the elastic energy homogeneously over the section: in fact, such a discontinuity modifies the displacement field and the corresponding stress field. The most external fibres do not participate to the storing of the elastic energy and to the generation of the corresponding force. To consider this effect, a reduced diameter is considered, smaller than the real one, but greater than the one of the adjacent elements. An example is shown in *Figure 5.3*. In particular, the maximum stiffness diameter is defined by:

$$D_{stifness,k} = L_{k-1} + L_k + D_{stifness,k-1} \tag{5.4}$$

where L is the element length and k is the element number.

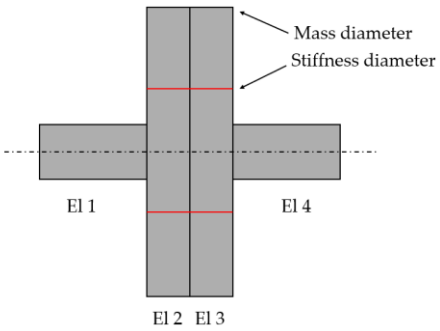

Figure 5.3: Fibers participating to elastic energy and difference between mass and stiffness diameter

The critical length criterion is also verified by considering these reduced diameters in the formula.

To further simplify the analysis, the turbine blades are modelled as rigid disks, one per stage. The exact blade profile is not available due to industrial confidentiality, so an approximate value for the mass and moment of inertia is used. The contribution of each stage is then added to four specific nodes, as depicted in *Figure 5.6.*

At this stage, for each element the total kinetic energy and the total elastic energy are computed. These quantities depend on *dofs* of the nodes, collected in the following vectors:

$$\delta u = \begin{Bmatrix} u_j \\ \psi_j \\ u_{j+1} \\ \psi_{j+1} \end{Bmatrix} \text{ and } \delta w = \begin{Bmatrix} w_j \\ \theta_j \\ w_{j+1} \\ \theta_{j+1} \end{Bmatrix} \tag{5.5}$$

Derivation of the following equation is not provided here, but is reported in [16]. Finally, applying the Lagrangian approach, using matrix notation, the equation of motion for a single element is obtained:

$$([M] + [M_s]) \begin{Bmatrix} \delta\ddot{u} \\ \delta\ddot{w} \end{Bmatrix} + \Omega[G] \begin{Bmatrix} \delta\dot{u} \\ \delta\dot{w} \end{Bmatrix} + [K] \begin{Bmatrix} \delta u \\ \delta w \end{Bmatrix} = 0 \tag{5.6}$$

where $[M]$ and $[M_s]$ account for the inertia effect, $[G]$ accounts for the gyroscopic effect and $[K]$ is the stiffness matrix.

Damping effect is the most critical contribution to evaluate: in general, is not known or has a quite complex nonlinear expression. In many practical cases, damping is introduced through a damping matrix, whose coefficients depend on rotational speed and are estimated empirically. Another widely used approach is the so-called *Rayleigh* technique: damping matrix $\left[C_{damping}\right]$ is computed as a linear combination of mass and stiffness matrices, weighted by coefficients α and β.

$$\left[C_{damping}\right] = \alpha[M] + \beta[K] \tag{5.7}$$

All the terms depending on velocities can be grouped together:

$$[C] = \left[C_{damping}\right] + \Omega[G] \tag{5.8}$$

Once the model is developed for a single element and matrices are computed, the whole system of equations is built, with a procedure called *assembly*. This process considers that each node may be shared by two or more adjacent elements. During assembly, $[K]$ matrix of each node is placed inside the total $[K]$ matrix at rows and

columns corresponding to *dofs* to which is referred, as shown in *Figure 5.4*. In the same way mass and damping matrices are built element by element.

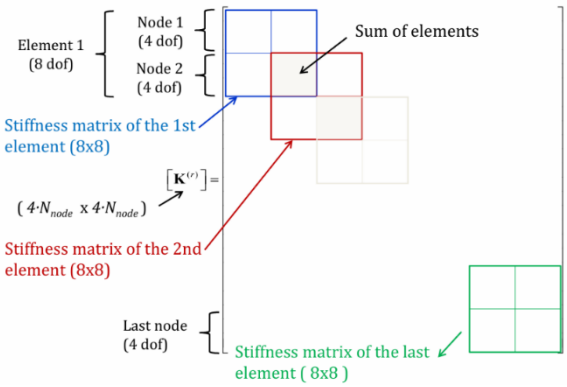

Figure 5.4: Assembly procedure for stiffness matrix

The model of the rotor is then completely linear.

The last step is to include in the equations all the other forces: unbalance, bearings… At this point, it is important to evaluate these forces and distinguish between those ones that can be included in matrices (i. e. linearly depending on displacement and its time derivatives) and those one that cannot. To deal with a force depending linearly on displacement, it is sufficient to add the constant of proportionality between the force and the displacement in the stiffness matrix, at the correct location. Similarly, the contribution of forces depending linearly on displacement time derivatives is introduced in the damping and inertia matrices. Conversely, nonlinear forces are considered placing their lagrangian components at the right side of the equation of motion. The right side is called *excitation*. It is important to remark that FEM algorithm allows considering only forces acting on nodes: if there are forces acting on points different from nodes or somehow distributed, they must be reported equivalently at nodes, using shape functions, as in the case of the weight contribution.

Mathematically, the contribution of excitations is introduced in the equation of motion by means of their lagrangian components:

$$\delta L = \{F\} \cdot \delta v \tag{5.9}$$

where δL is the virtual work produced by the lagrangian components $\{F\}$ times the node virtual displacement δv.

A classical example of periodic excitation is the unbalance force:

$$F_x = me\ \Omega^2\ cos(\Omega t + \phi) \tag{5.10}$$

$$F_y = me\,\Omega^2\,sin(\Omega t + \phi) \tag{5.11}$$

where m is the unbalanced mass and e is the eccentricity. The phase ϕ is the orientation angle with respect of x-z axis of the unbalance node is at the time t=0.

The final set of differential equations obtained, with as many equations as the number of *dofs* describing the system, is in matrix formulation:

$$[M]\{\ddot{x}\} + [C]\{\dot{x}\} + [K]\{x\} = \{F\} \tag{5.12}$$

where $\{x\}$ collects all the *dofs* of the system.

At this point, the system can be simplified to a fully linear one, enforcing nonlinear terms to be linear (*linearization*) around the equilibrium position, by means of a Taylor expansion. Or it is possible to maintain nonlinear terms, exploiting iterative algorithms to reach the solution.

When including the axial degree of freedom and thrust bearing effects, the matrices in the linear forcing formulation take the following form:

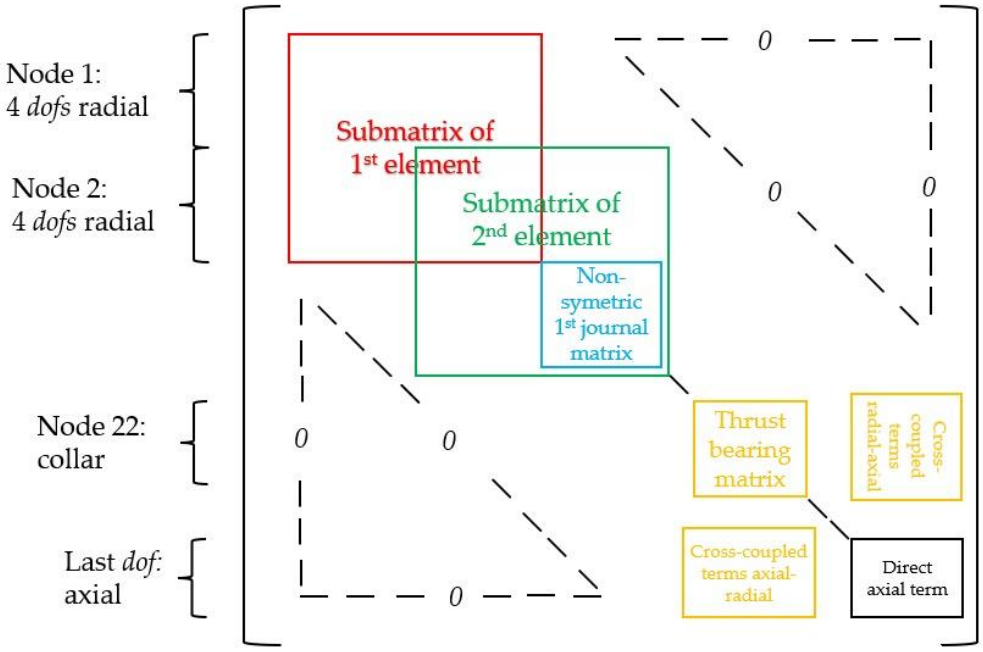

Figure 5.5: matrix general shape

In particular:

- The mass matrix is banded and symmetric. It does not include block contributions from the thrust bearing (highlighted in yellow in the *Figure 5.5*), nor the blue-highlighted blocks associated with the journal bearings. The last

row and last column consist entirely of zeros, except for the bottom-right element, which contains the rotor mass and represents the axial inertia.

- The stiffness matrix is initially symmetric and banded, up to the point where the bearing contributions are introduced. Once the stiffness terms from the bearings are added at the degrees of freedom corresponding to the relevant nodes, the matrix becomes non-symmetric. The last row and column are filled with zeros, except for the cross-coupled blocks introduced by the thrust bearing.
- The gyroscopic matrix $[G]$ is band and antisymmetric. It does not include any contribution from bearings, like the mass matrix. The antisymmetric structure typically introduces destabilizing effects in the system. Both the last row and column are composed entirely of zeros.
- The damping matrix $[C_{damping}]$ is sparse, containing only the contributions from the bearings. These bearing-related damping blocks have the same structural layout as the corresponding bearing stiffness blocks. For example, the damping matrix of the thrust bearing has the same block structure as its stiffness counterpart.

To improve clarity, the degrees of freedom at each node follow this order:

$$\{v_{node}\} = \begin{bmatrix} u \\ w \\ \theta \\ \psi \end{bmatrix} \tag{5.13}$$

$$[K_{journal}] = \begin{bmatrix} K_{xx} & K_{xz} & 0 & 0 \\ K_{zx} & K_{zz} & 0 & 0 \\ 0 & 0 & 0 & 0 \\ 0 & 0 & 0 & 0 \end{bmatrix} \tag{5.14}$$

As already pointed out, the matrix structure is equal comparing stiffness and damping, therefore only stiffness blocks are illustrated.

The direct stiffness axial term is:

$$[K_{thrust\_axialaxial}] = K_{yy} \tag{5.15}$$

The thrust bearing matrix instead is:

$$[K_{thrust\_radialradial}] = \begin{bmatrix} 0 & 0 & 0 & 0 \\ 0 & 0 & 0 & 0 \\ 0 & 0 & K_{\theta\theta} & K_{\theta\psi} \\ 0 & 0 & K_{\psi\theta} & K_{\psi\psi} \end{bmatrix} \tag{5.16}$$

The cross coupled axial radial term lies in the last row and in the position corresponding to the collar *dofs* has the shape:

$$\left[K_{thrust\_axialradial}\right] = [\,0 \quad 0 \quad K_{y\theta} \quad K_{y\psi}] \tag{5.17}$$

In a similar way, the cross coupled term radial-axial are in the last column and act on the thrust runner *dofs*:

$$\left[K_{thrust\_radialaxial}\right] = \begin{bmatrix} 0 \\ 0 \\ K_{\theta y} \\ K_{y\psi} \end{bmatrix} \tag{5.18}$$

After some numerical simulations with a very precise FE model, able to reproduce totally the machine geometry, the FE model is simplified. The number of elements is reduced especially in the compressor zone, while a relatively dense discretization is maintained in the thrust zone, object of the current analysis. The aim of this procedure is to reduce the total number of degrees of freedom (*dof*) of the system and thus speed up the numeric experiments. *Figure 5.6* shows the original model.

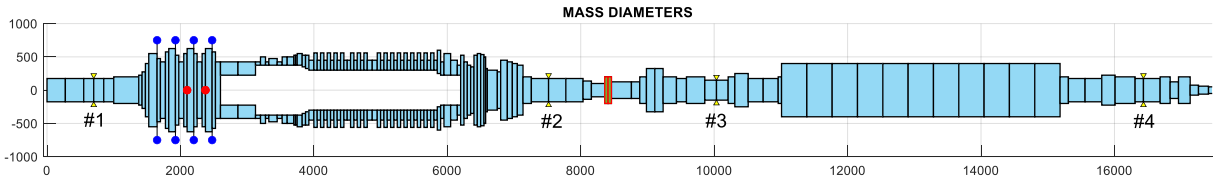

Figure 5.6: Original FEM model

When the diameters of adjacent elements are slightly different, they are replaced by a single equivalent element. The maximum length for each element is fixed at 1000 mm, as this value is well below the critical length in the non-reduced model. To compute the mass and stiffness diameters (both external and internal) of the new element, the following conditions are imposed:

- Conservation of mass
- Conservation of polar moment of inertia
- Conservation of flexural moment of inertia

After obtaining the new set of elements, the critical length is re-evaluated, confirming that all elements remain within safe limits. Although it is not possible to perfectly satisfy all of these conditions simultaneously, the best possible compromise has been achieved.

The final reduced model, consisting of 41 elements, is shown in *Figure 5.7*.

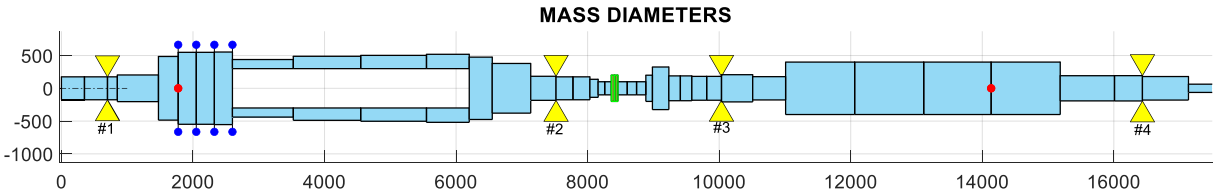

Figure 5.7: Reduced FEM model

From a comparison with the previous model, the reduced one appears sufficiently reliable. This comparison is based on the first mode shapes; in *Figure 5.8* is shown the comparison between the same mode shape obtained with a different number of finite elements.

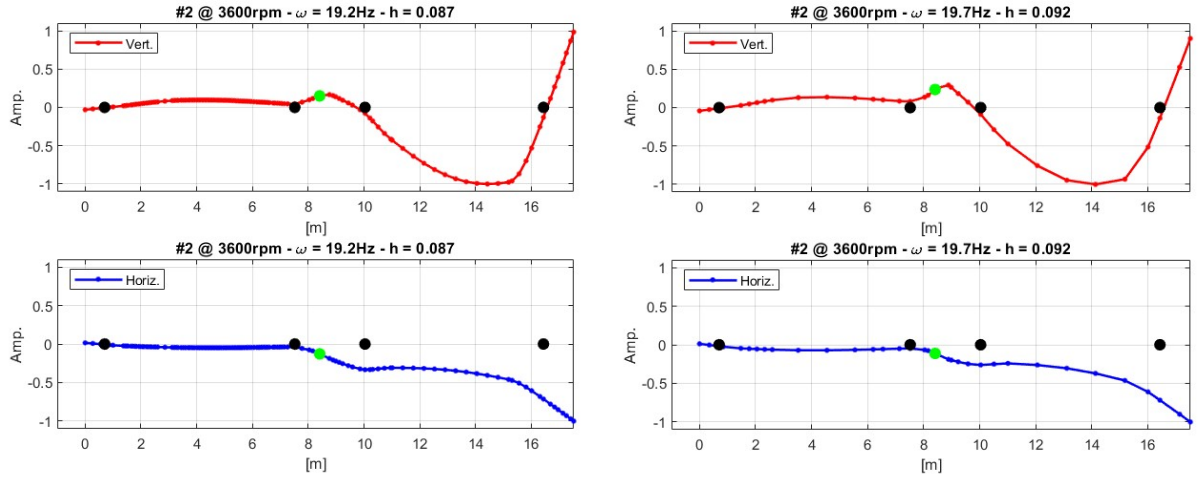

(a) (b)

Figure 5.8: Mode shape #2: (a) before reduction; (b) after reduction

The first five natural frequencies are very similar in the two analysis developed, as shown in *Table 5.2*, with a maximum error difference of 5,0% for mode #3.

Mode	Complete model: frequency [Hz]	Reduced model: frequency [Hz]	Difference %
1	19.22	19.68	2.4
2	21.18	21.41	1.1
3	24.84	26.08	5.0
4	29.84	30.64	2.7
5	42.02	42.41	0.9

Table 5.2: Comparison of lateral natural frequencies of complete and reduced models

5.2.2 Bearings model

The contribution of bearings is taken into account according to their nature, journal or thrust. Every TPJB is considered as a system of linear spring and damper with linearized coefficients introduced in matrices at the corresponding *dof*. The axial TPTB is modelled in two different ways: linear and nonlinear. In the linear approach, the TPTB is treated similarly to a journal bearing, represented as a system of linear springs and dampers. The nonlinear case is more complex: the exact nonlinear forces are computed by solving the Reynolds equation and they depend both on displacement and velocity of the thrust collar. All the forces are computed and then added in the trust collar node to assemble the equation of motion.

Due to the high computational cost of solving these equations in real time during the initial implementation, an alternative strategy is adopted. A dedicated dataset is generated offline, and both an interpolator and a neural network are trained. The resulting model employs either predictions from an Artificial Neural Network (ANN) or static force interpolation combined with a linearized damping contribution to approximate the nonlinear behaviour efficiently. Both the approaches are addressed in detail in *Chapter* 7. As said, TPTB used in the model is not *self-leveling*. For sake of simplicity, no other components (e. g. seals) are considered in this model.

Journal bearings are now considered. The linearized forces are modelled by the following matrices of linearized coefficients, depending both on the journal bearing static load and rotational speed of the shaft. Regarding notation, the first letter in a coefficient indicates the direction of the load, while the second letter represents the direction of the displacement.

$$K_{journal} = \begin{bmatrix} k_{xx} & k_{xz} \\ k_{zx} & k_{zz} \end{bmatrix}$$

$$C_{journal} = \begin{bmatrix} c_{xx} & c_{xz} \\ c_{zx} & c_{zz} \end{bmatrix}$$

Table 5.3 summarizes the three different cases described above, about hydrodynamic forces and moments generated by the thrust bearing.

	Linear model	Nonlinear ANN	Nonlinear interpolator
Stiffness	Linearized coefficients (constant) $k_{yy}\ k_{\theta\theta}\ k_{\psi\psi}\ k_{y\theta}\ k_{y\psi}$ $k_{\theta y}\ k_{\psi y}\ k_{\theta\psi}\ k_{\psi\theta}$	Nonlinear forces accounting for both stiffness and damping $F = F(y, \theta, \psi, \dot{y}, \dot{\theta}, \dot{\psi})$ $Mx = Mx(y, \theta, \psi, \dot{y}, \dot{\theta}, \dot{\psi})$ $Mz = Mz(y, \theta, \psi, \dot{y}, \dot{\theta}, \dot{\psi})$	Nonlinear forces $F = F(y, \theta, \psi)$ $Mx = Mx(y, \theta, \psi)$ $Mz = Mz(y, \theta, \psi)$
Damping	Linearized coefficients (constant) $c_{yy}\ c_{\theta\theta}\ c_{\psi\psi}\ c_{y\theta}\ c_{y\psi}$ $c_{\theta y}\ c_{\psi y}\ c_{\theta\psi}\ c_{\psi\theta}$		Linearized coefficients $c_{yy}\ c_{\theta\theta}\ c_{\psi\psi}\ c_{y\theta}\ c_{y\psi}$ $c_{\theta y}\ c_{\psi y}\ c_{\theta\psi}\ c_{\psi\theta}$

Table 5.3: Stiffness and damping forces and their dependencies in different models

The linearised formulation of the thrust bearing model is given by:

$$\begin{bmatrix} M_x \\ M_z \\ F \end{bmatrix} = \begin{bmatrix} c_{\theta\theta} & c_{\theta\psi} & c_{\theta y} \\ c_{\psi\theta} & c_{\psi\psi} & c_{\psi y} \\ c_{y\theta} & c_{y\psi} & c_{yy} \end{bmatrix} \begin{bmatrix} \dot{\theta} \\ \dot{\psi} \\ \dot{y} \end{bmatrix} + \begin{bmatrix} k_{\theta\theta} & k_{\theta\psi} & k_{\theta y} \\ k_{\psi\theta} & k_{\psi\psi} & k_{\psi y} \\ k_{y\theta} & k_{y\psi} & k_{yy} \end{bmatrix} \begin{bmatrix} \theta \\ \psi \\ y \end{bmatrix}$$

θ is the rotation about x axis , ψ rotation with respect to z axis and y the axial displacement.

The subscript of the moment indicates its direction.

5.2.3 Unbalance model

Unbalance is defined as the non-coincidence between the centre of mass of a section of the shaft and the centre of rotation of the same section; the distance between these two points is called *eccentricity*. In other words, the mass distribution is not symmetrical about the centre of rotation. As a result, when the shaft rotates, a centrifugal inertia force is generated. Moreover, the unbalance varies along the shaft axial coordinate. Therefore, it is common practice to represent it as equivalent concentrated unbalances located at specific nodes. In the considered model, just two unbalances contributions are considered for the entire rotor: one located at the turbine and one at the generator. These locations are chosen so that they can excite all the first vibrating modes of the machine.

A certain amount of residual unbalance is always present in real rotating machines: in fact, because of manufacturing processes, the shaft is not perfectly cylindrical and the blades often exhibit slight variations in mass. Therefore, the mass of the rotor is not uniformly distributed around the shaft line. Unbalance, generally, is expressed as the product between a mass and the eccentricity, in kgm. This excitation force is periodic with a frequency equal to the rotating one, called *fundamental,* and it is

referred to be *synchronous*. The turbine presented here rotates at 3600 rpm. For a rotating machine, the unbalance is one of the most exciting forces applied on the rotor and represents a non-negligible source of lateral vibration. In industrial field, it is a typical practice to reduce the amount of unbalance of a rotating machine, adding some masses in specific location of the rotor. This technique, called *rotor balancing*, is not discussed here for sake of brevity.

5.2.4 Blade excitation model

As shown in *Figure 5.9,* The working fluid generates aerodynamic forces acting on the blades of both the compressor and the turbine, which are treated as airfoils. The evaluation of these forces is quite complex, task often performed by means of Computational Fluid Dynamics (CFD) analysis. For the aim of this work, the phenomenon is well simplified by considering an equivalent force composed by a constant contribution and a random one, both in axial and radial directions.

$$F(t) = F_{const} + GWN(t) \tag{5.19}$$

where F_{const} is constant and $GWN(t)$ represents the Gaussian White Noise function. This noise, used to describe a random process, is defined Gaussian since its probably density is distributed as a gaussian curve; it is defined White since its spectral density is flat (it has the same amplitude at each frequency). Furthermore, the noise has been filtered between 5 and 120 Hz with a second order filter, to have a more effective excitation of the shaft modes. The result is then a band-limited noise.

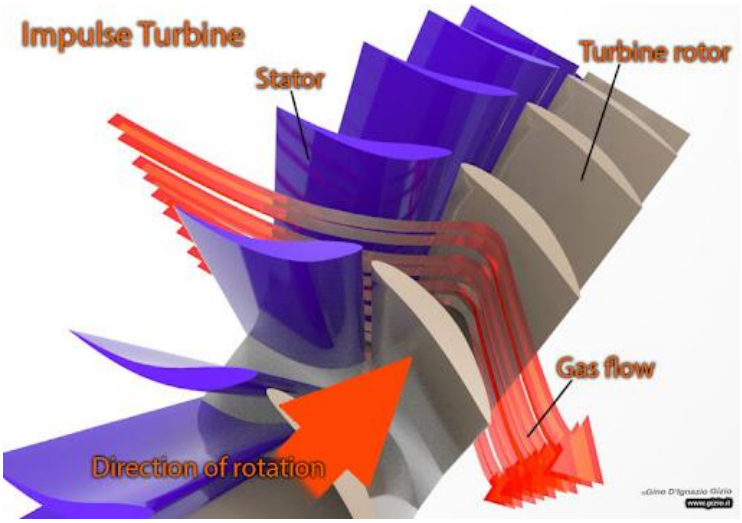

Figure 5.9: Example of working fluid flow inside a turbine stage

5.2.5 Axial dynamics

Since lateral dynamic is much more studied with respect to axial one, many rotordynamic models available in the literature neglect the axial *dof*. However, non-negligible axial forces arise from different types of machine elements, such as blades, rotor-stator cavities or disks, as reported by Bozzi et al. in [20]. Obviously, the model presented in this work must include somehow the axial displacement of the machine. Assuming the shaft is axially infinitely rigid, a single axial *dof* is sufficient to model the axial dynamics. Under this simplification, axial stiffness and damping are mainly due to thrust bearing, while the inertia corresponds to the mass of the entire rotor. This choice is justified by the following assumption: the first axial natural frequency due to shaft stiffness is expected to be much higher than frequencies at which axial exciting forces typically occur during operation. The only axial *dof* considered y is placed inside the displacement vector as the last element.

$$\{x_{total}\} = \begin{Bmatrix} x \\ y \end{Bmatrix} \tag{5.20}$$

5.3 Static equilibrium due to weight

When considered, the effect of gravitational load is computed applying the virtual work principle:

$$\delta L = \int_0^L -g\delta z dM = -\int_0^L g\rho S N_2 \delta w dy \tag{5.21}$$

Here, N_2 is the shape function associated with the vertical displacement field, and it is defined as:

$$N_2 = \begin{bmatrix} 1 - \frac{3y^2}{L^2} + \frac{2y^3}{L^3} \\ z - \frac{2y^2}{L} + \frac{y^3}{L^2} \\ \frac{3y^2}{L^2} - \frac{2y^3}{L^3} \\ -\frac{y^2}{L} + \frac{y^3}{L^2} \end{bmatrix} \tag{5.22}$$

Finally, the lagrangian component of the virtual work, corresponding to an equivalent nodal force vector, is obtained:

$$W_{ele} = -g\begin{bmatrix} \frac{M}{2} \\ -\frac{ML}{12} \\ \frac{M}{2} \\ \frac{ML}{12} \end{bmatrix} \tag{5.23}$$

The global force vector W is assembled by combining the contributions from all elements through the following matrix operation:

$$\{W\} = [M]\{G\} \tag{5.24}$$

where the vector G is:

$$G = \begin{bmatrix} 0 \\ -g \\ 0 \\ 0 \\ 0 \\ -g \\ 0 \\ 0 \\ : \end{bmatrix} \tag{5.25}$$

In this structure, the value *-g* is applied to the vertical *dofs* associated with translational motion, while the remaining entries correspond to degrees of freedom not directly affected by gravity.

Journal bearings are modelled as ideal hinges, where zero displacement is imposed at their locations. Consequently, at each node, either the displacements or the forces are null and known. From a static point of view, the problem is formulated as an hyperstatic problem. Reaction forces at bearings are computed solving it.

Taking into account the thrust bearing significantly increases the complexity of the problem. The tilting of the collar generates moments and modifies the static equilibrium. Consequently, because of this contribution, the governing equations become nonlinear. In fact, thrust moments depend nonlinearly on the current state of the runner, as follows:

$$M_{x\_thrust}(\theta, \psi, y) = M_{x\_thrust\_weight} + M_{x\_thrust\_state}(\theta, \psi, y) \tag{5.26}$$

where $M_{x\_thrust\_weight}$ represent the moment components previously evaluated, which arise from the weight of the system. $M_{x\_thrust\_state}(\theta, \psi, y)$ denote the moment components that depend explicitly on the current state of the runner. Such moments

are then updated in the above equation. Similarly, $M_{z\_thrust}(\theta, \psi, y)$ is computed and updated. As a result, a new formulation of the hyperstatic problem is required, in which reaction forces depend also on ϑ, ψ and y of the thrust node.

An extra equation is considered to ensure axial equilibrium:

$$F_{static} + F_{thrust}(\theta, \psi, y) = 0 \tag{5.27}$$

Equations are solved though the Newton-Raphson iterative procedure. The rotational angles ϑ and ψ from the thrust-free case are chosen as initial guess. From equation (5.27) the axial equilibrium position is computed. The axial load is then incrementally increased or decreased, and the solution from the previous load step is used as the initial guess for the next, following a *path continuation* strategy.

The results concerning the trends of ϑ, ψ and y as functions of the axial load are presented in *Chapter 4*.

5.4 Linear solution

Once the system is obtained, it is possible to solve it, as reported in [21]. The first step is to rewrite the system in the state-matrix form, adding an identity involving the vector of velocities:

$$\begin{cases} \{\ddot{x}\} = -[M]^{-1}[C]\{\dot{x}\} - [M]^{-1}[K]\{x\} + \{F_{ext}\} \\ \{\dot{x}\} = \{\dot{x}\} \end{cases} \tag{5.28}$$

Rewritten as:

$$\{\dot{z}\} = \begin{bmatrix} -[M]^{-1}[C] & -[M]^{-1}[K] \\ I & 0 \end{bmatrix} \{z\} + \{F_{ext}\} = [A]\{z\} + \{F_{ext}\} \tag{5.29}$$

where $\{z\} = \begin{Bmatrix} \dot{x} \\ x \end{Bmatrix}$.

Thanks to this transformation, it assumes the form of a first order set of differential equations, doubling the number of equations and consequently the dimensions of the system. The solution to such a system is the sum of the solution of the homogeneous system associated (i.e., the solution of the system with a zero right-hand side) plus a *particular solution*, that accounts for the external excitations.

A particular solution is any solution of the complete system, when the right-hand side is considered, and, generally, it exhibits the same functional form as the excitation itself. For instance, for a system excited with a typical cosine force,

$$\{F\} = \{F_0\}\cos(\Omega t) \tag{5.30}$$

the particular solution is a cosine with the same frequency of the exciting force:

$$\{x\} = \{x_0\}\cos(\Omega t + \phi) \tag{5.31}$$

For stable systems, the free response plays a relevant role only during the transient, that is the time interval when the free response and the excited one have almost the same order of magnitude. When the amplitude of the free response becomes negligible, the transient is considered vanished and the system is said to have reached the steady state.

The system of equations then becomes:

$$[M]\{\ddot{x}\} + [C]\{\dot{x}\} + [K]\{x\} = \{F_0\}e^{i\Omega t} \tag{5.32}$$

$\{x\}$ assumes then the same shape of the forcing term: $\{x\} = \{X_0\}e^{i\Omega t}$.

Since $\{X_0\}$ is a set of complex numbers, it contains information about both the amplitude and phase of the response. The steady-state response of the system depends both on the amplitude of the excitation and on the frequency at which the excitation is applied.

A typical trend of these functions, for the linear case of a multi-*dof* system, is reported in *Figure 5.10*.

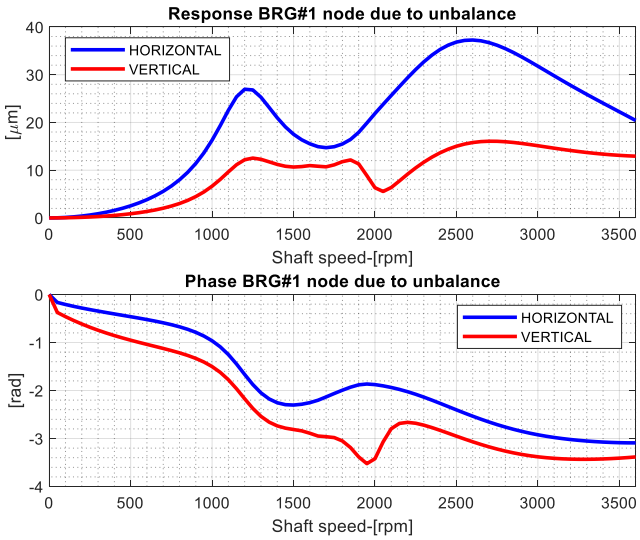

Figure 5.10: Unbalance response of the system in amplitude and phase as function of shaft rotational speed located at radial bearing #1.

5.4.1 Modal analysis

A convenient approach to study linear systems is the so-called *modal analysis*. Briefly, it considers the solution as a linear combination of eigenvectors of the system:

$$\{x\} = [\phi]\{q\} \tag{5.33}$$

where $[\phi]$ is the matrix collecting wholly or partly the eigenvectors (not time-depending) of the system, while $\{q\}$ collects the time-depending part of the response associated with those eigenvectors.

The objective is to change coordinates, from physical ones to modal ones. Multiplying the system by the transpose of eigenvector matrix, a new set of equations is obtained:

$$[\phi]^T[M][\phi]\{\ddot{q}\} + [\phi]^T[C][\phi]\{\dot{q}\} + [\phi]^T[K][\phi]\{q\} = [\phi]^T\{F\} \tag{5.34}$$

If the original system contains no terms explicitly depending on $\{\dot{x}\}$, and if the mass and stiffness matrices are symmetric, the transformation to modal coordinates leads to a fully decoupled set of equations. In this case, the transformed mass and stiffness matrices become diagonal, greatly simplifying the system solution. This property can be effectively exploited to reduce computational effort, as each mode can be analysed independently. Even in the presence of light damping, as is the case in the present study, this approach remains valid and efficient, offering a good approximation while preserving the dominant dynamic behaviour of the system.

Thanks to this approach, it is possible to select a subset of relevant modes, the ones having the associated eigenfrequency below a chosen threshold. This one is selected according to wanted degree of approximation, higher than the excitation one (in case of unbalance, the rotational speed of the machine); standard values are 1.5 or 2 times the excitation frequency. Modes with higher frequencies cannot be excited and their contribution to the solution is negligible.

A modal analysis is then conducted, in order to evaluate the most relevant natural frequencies of the system and to visualize mode shapes. The results are presented in *Chapter* 8.

The primary objective of this analysis is to identify the axial, horizontal or vertical mode shape; or if any mode occurs in more than one direction and is somehow coupled. The mode shapes are normalized between -1 and 1, following the approaches:

1) Normalization separately for each direction, i.e., vertical degrees of freedom normalized by the maximum imaginary part of vertical and axial displacement, and horizontal degrees of freedom normalized by the maximum imaginary part of horizontal and axial displacement.
2) Normalization with respect to the maximum imaginary part among vertical, horizontal and axial components.

To plot both the axial magnitude and the radial ones within the same plots, axial displacement of the entire machine is plotted as vertical bars, whose height is proportional to the axial displacement itself.

Finally, the mode shape evolution in time is plotted: both vertical and horizontal degrees of freedom vibrate at the eigenmode natural frequency. The amplitude of the cosine function is equal to the absolute value of complex modal component associated with that *dof*. The phase of each degree of freedom corresponds to the phase angle of its associated complex value. Also in this case the modal shape is normalized, as described above, to facilitate comparisons.

5.5 Nonlinear solution

Not always linear approximation is acceptable, due to different reasons: in this case, a more sophisticated model is required, paying in terms of computational resources consumed. The case described here is strongly nonlinear, about the thrust bearing forces. In particular, when the rotor vibrates axially, reaching both the extremities of the thrust clearance (350 μm), the assumption of small displacements around the equilibrium position is no more valid. Thus, linearized model is no longer representative of the actual system behaviour.

As previously discussed, no analytical expressions are available for the nonlinear thrust bearing forces and moments. Therefore, these quantities must be computed numerically, using a dedicated external code (as described in *Chapter 3.2*), and then placed at the right-hand side of the equations of motion in the correct row. Nonlinear models characterizing fluid film lubrication are available in the literature: an example is proposed by Huang in [22] to investigate the effect of lubricating oil temperature.

The initial condition for the time integration corresponds to the static deformation caused by gravity, which weakly depends on the axial load. For a detailed treatment of the required displacements, the reader can refer to *Chapter 8*. No initial velocities are imposed, so the shaft is initially at rest and in static equilibrium.

Regarding the pad dynamics integration (briefly described in *Chapter 9.3*), their rotation at the initial time instant ($time = 0$) is set consistently with each equilibrium

position. This choice ensures that the system is not unbalanced at the start of the simulation.

To solve the nonlinear system, various solution techniques are available, including Harmonic Balance and time integration methods. Mathematical theory of nonlinear rotordynamics is available in [21]. Here, time integration is proposed, thanks to its wide diffusion in the industrial field and reliability. When combined with Craig-Bampton reduction (see *Chapter 6*), the method becomes relatively efficient, allowing simulations on the order of 35 minutes. Basically, the procedure comprises the following steps:

- As in the case of the linear model, the system is rewritten in the form $\{\dot{z}\} = [A]\{z\} + F_{Nlin}$
- The nonlinear force F_{Nlin} is computed at the actual state of the system
- Selected the time step Δt, the state increment is computed as: $\{\Delta z\} = \{\dot{z}\} \cdot \Delta t$
- The state is updated as: $\{z(t_{i+1})\} = \{z(t_i)\} + \{\Delta z\}$
- The procedure is repeated until the end of the time interval selected for the analysis is reached.

This procedure is performed automatically by the MATLAB built-in *ode* solver, based on Runge-Kutta methods. This solver offers improved accuracy and adaptive time stepping, making it more robust and efficient than the simplified Euler approach. The user simply provides, as inputs, the function describing the system, the time interval and the initial conditions; as output, the code computes the evolution of the system in time. A very typical issue of this method is the correct time step selection: a wide time step can lead to divergence of the computed solution from the real one (numerical instability); on the contrary, a too small time step can lead to accumulation of numerical error, badly approximating the solution. *Ode45* adapts automatically and dynamically the time step, in order to solve, if possible, these issues. This ensures an optimal balance between accuracy and computational efficiency, within the tolerances specified by the user. It is also possible to impose the maximum step size at 1×10^{-4}, to accurately capture noisy or transient behaviour. When analysing a phenomenon with a certain frequency content, the imposed sampling frequency used to evaluate the signal must be at least twice the highest frequency component, in accordance with Shannon's theorem, to avoid aliasing effects.

The choice of the integrator is also important and strictly depends on the nature of the problem. An overview is provided in *Table 5.4*.

Solver	Method Type	Name Meaning	Advantages	Drawbacks	Time Behavior	Recommended Use
ode45	Explicit, embedded Runge-Kutta 4th/5th order	"45" embedded pair of Runge-Kutta formulas: the 5th-order for solution, 4th-order estimates the local error	General-purpose, accurate, widely used, automatic step sizing	Not suitable for stiff or highly transient problems.	Medium computational cost. Performs well on moderately fast or smooth systems.	General-purpose, non-stiff vibration analysis
ode23	Explicit, embedded Runge-Kutta 2nd/3rd order	"23" = Embedded Runge-Kutta pair: 3rd-order for solution, 2nd-order for error estimation	Fast on simple models, low CPU time	Less accurate; more steps needed. Poor with high-frequency content.	Very fast on short or smooth simulations.	Basic, quick simulations; low-accuracy needs
ode23t	Implicit, trapezoidal rule (modified)	"t" = Trapezoidal method	Handles mild stiffness and discontinuities	Not ideal for sharp transients.	Moderate time cost.	Mildly stiff, smooth time evolution
ode23tb	Implicit, Rosenbrock method (order 2)	"tb" = Combines Trapezoidal and Backward Euler (BDF-like method)	Efficient on moderately stiff problems	Less effective for highly nonlinear or fast-changing dynamics.	Balanced time/accuracy trade-off.	Semi-stiff systems with moderate time/frequency behavior
ode15s	Implicit, variable-order BDF (backward differentiation formula)	"15s" = Variable-order up to 5. "s" = Stiff systems	Powerful for very stiff, large-scale systems	Computationally expensive for non-stiff problems.	Slow but robust on large or multiscale problems.	Strong stiffness, long-duration or high dynamic range simulations
ode113	Explicit, Adams-Bashforth-Moulton (multistep)	"113" = Variable-order Adams method (up to 13)	Very accurate for smooth, slow-changing systems	Inefficient for short-term fast dynamics.	Slow for fast dynamics; best for very smooth long simulations.	Long-term, smooth behavior where high accuracy is needed
ode15i	Implicit, DAE solver (differential algebraic equation)	"i" = Implicit solver for Differential-Algebraic Equations	Supports algebraic constraints; suitable for DAE models	Setup is complex; requires implicit formulation.	Performance depends on system stiffness and DAE complexity.	Constrained systems; DAE modeling

Table 5.4: Benchmark of the integrators commonly used in rotordynamics.

In order to compare the linear case with the nonlinear one, the response is evaluated in the frequency domain: the spectrum is computed by a Fourier Transformation of the system response in the time domain. Typically, a nonlinear system excited at a certain frequency responds with several frequencies, integer multiples of the one of the excitation, called *fundamental*. The amplitude of the response generally decreases as the harmonic order increases. Clear examples of this phenomenon are available in *Chapter 9.*

The frequency response of the system, in terms of amplitude and phase, is very meaningful. It differs significantly from the linear case and, at this point, a brief description is mandatory. The curve representing the amplitude, function of the frequency, has a peak in the resonance zone bent to the right due to the stiffening behaviour of the nonlinear spring. The curve is called *backbone*, due to this characteristic form, as shown in *Figure 5.11*. In the descendent branch of the curve after the resonance, two different solutions coexist at the same frequency: this phenomenon, typical of nonlinear systems, is called *bistability*.

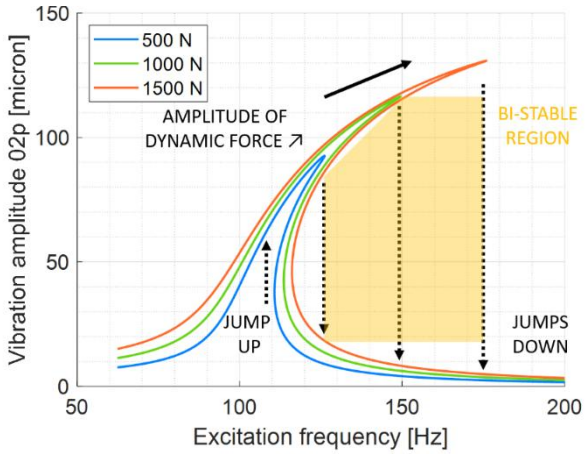

Figure 5.11: Typical response of a nonlinear system; particular of bent peak and bi-stable region

6 Craig-Bampton approach

6.1 Introduction

Solving for the full state is too computationally expensive, considering that:

- each node has 4 degrees of freedom (2 radial displacements u and v and the rotations θ and ψ with respect to x and z axis)
- 42 nodes are present in the rotor
- 1 dof is added to simulate the axial dynamics
- the equations of the system are written in the state space form $\dot{x} = f(x) + Fnl$, where F_{nl} represents the forces acting on the system, nonlinear because of the thrust bearing. x contains than in order the velocities and then the generalized displacements, as seen in previous chapters.

Total nodes	44
Total radial *dofs*	$44 \cdot 4 = 168$
Total system *dofs*, including axial *dof*	$168 + 1 = 169$
Total number of equations	$169 \cdot 2 = 338$

Table 6.1: Degrees of freedom of the system

This brings to a system of 338 equations, that is quite computationally expensive when using a time integration method, and it requires also a relevant amount of temporary memory.

In the literature, several techniques are available to mitigate this issue: essentially, they aim to reduce the total number of *dofs* of the whole system, trying to minimize the approximation error, that should be considered when the system order is reduced. From a numerical point of view, another beneficial effect is the reduction of condition number of the matrices. High condition numbers may lead to numerically unstable eigenvalues. However, simply reducing the number of elements cannot be a viable strategy, because it makes the structure stiffer and sometimes cuts some

frequencies that could be relevant in the analysed case. Thus, Component Mode Synthesis is a way to reduce the state without losing physical meaning, and it is relatively easy to be implemented. This technique is widely applied in rotordynamic, aeronautic and automotive field. Once the complete system is replaced by another one almost equivalent, but with a significant reduction in matrices and vectors dimensions, it can be solved using standard techniques (e.g. time integration), saving significantly computation resources.

The main objective of this procedure is to store offline the mass, stiffness and damping matrices in a smaller form, with very little loss in terms of accuracy. As reported in [23] and [24], this is very convenient in multibody analysis or when dealing with transients or high frequencies.

Overview of methods commonly used to reduce the model.

- Guyan reduction, or static condensation: it consists in dividing the *dofs* in master and slave ones. The system is rewritten, through some mathematical passages, using only master *dofs*, neglecting totally the slave ones. The solution considers only generalized coordinates of master *dofs*, while behaviour of slave ones is obtained by a matrix multiplication from the computed solution. The drawback of this method is: although the stiffness matrix representing the elastic behaviour of the whole structure is well defined and exact, the mass matrix is approximated, leading to a significant error in dynamic simulations, where inertia effects cannot be neglected.
- Modal approach: it is very used when dealing with linearized dynamic problems, thanks to its simplicity; it only requires evaluating the eigenvectors of the system. Furthermore, it brings to a set of decoupled equations, if the original matrices are symmetric. This property is exploited to reduce the computational effort. Moreover, relevant modes are only the one associated in a range of frequencies near the one excited, bringing to reduced square matrices mxm, where m is the number of selected modes. The drawback is that this technique does not describe any rigid displacements, and thus it does not work if constraints are added or removed; it is also impossible to simulate nonlinearities because of the linearized approach.
- Craig-Bampton method (also called *dynamic condensation*): this approach mixes the benefits of the two above-mentioned procedures:
    - Accounting for both mass and stiffness matrixes
    - Problem size is defined by the considered frequency range

- Possibility for different boundary conditions at the interface (unlike modal decoupling)

Basically, it distinguishes between master and slave nodes and their *dofs*: the master ones are explicitly calculated, while the slave ones are omitted during the calculation procedure, but are related to the master ones through a transferring matrix; the static behaviour is *exact* at the master nodes. Conveniently, they can be chosen as point of measurement, to compare the solution obtained with signals from sensors. It is also good practice to consider as master nodes those ones where forces are applied. All the remaining degrees of freedom are defined as slaves. In order to characterised also the dynamic behaviour of the system, some modal generalised coordinates (according to wanted degree of accuracy) are added to coordinates representing the *dofs* of the master nodes. In this way a system with a reduced number of generalised *dofs* is obtained, able to represent both the static and the dynamic behaviour of the real system. F. Palloni in [23] underlines some advantages and disadvantages.

Advantages:

- Good accuracy of the model
- Few modes are required at boundary *dofs* constrained, even to simulate the behaviour at high frequencies
- The position and the number of master nodes and consequently of master *dofs* is not so strictly important, and the above-mentioned considerations are enough to avoid distortions.

Disadvantages:

- More equations are required with respect to a pure modal approach or static condensation.
- The resulting matrices are neither diagonal (as could be in a modal approach), neither sparse as in the starting model, due to the dense static part, necessary to compute the displacement at slave nodes caused by displacements at master nodes.

6.2 Mathematical description

Here is provided a description of the Craig-Bampton algorithm, from a mathematical point of view, focusing on how to build the matrices involved.

Starting from the dynamics equations of the system, which can be written in the ordinary form:

$$[M]\{\ddot{v}\} + [C]\{\dot{v}\} + [K]\{v\} = \{Q\} \tag{6.1}$$

where $\{v\}$ is the vector of generalized system coordinates and $[M]$, $[C]$ and $[K]$ are mass, damping and stiffness matrices, respectively. $\{Q\}$ is the vector of externally applied loads. Details about equation (6.1) are present in *Chapter 5.3.*

As previously mentioned, the strength of the Craig reduction method lies in selecting a subset of degrees of freedom, typically the constrained ones and expressing the remaining degrees of freedom in terms of these master coordinates. From this point onward, the subscripts m and n will refer to master and slave degrees of freedom, respectively.

To apply this procedure, equation (6.1) must first be reordered so that the first m rows correspond to the equations related to the master degrees of freedom, while the remaining rows correspond to the slave degrees of freedom. Indeed, the system matrices are constructed starting from the original matrices. It is advisable to arrange both the master and slave degrees of freedom in ascending order according to their original numbering. These reordered sets then define the new state variables.

This reordering facilitates the assembly of the matrices in equation (6.2) below, where the state vector is formed by concatenating the master and slave *dofs* in the reordered sequence. The system matrices are partitioned into four submatrices, with the order of the subscripts indicating the force direction: the first subscript refers to the direction of the force, and the second to its cause. For example, in the matrix M_{mn}, the element at position (5,2) represents the inertia force acting on the fifth reordered master degree of freedom caused by the activation of the second reordered slave degree of freedom. If, in the reordered sets, the second slave degree of freedom corresponds to original *dof* 7 and the third master degree of freedom corresponds to original *dof* 35, then the element at position (2,3) in M_{nm} equals the element at row 7, column 35 in the original mass matrix M.

Similarly, the first m components of the vector on the right-hand side of equation (6.2) are taken from the original vector $\{Q\}$ at the positions indicated by the reordered master degrees of freedom and inserted into the entries corresponding to their position within the full state vector containing both master and slave degrees of freedom.

$$\begin{bmatrix} M_{mm} & M_{mn} \\ M_{nm} & M_{nn} \end{bmatrix} \begin{bmatrix} \ddot{v}_m \\ \ddot{v}_n \end{bmatrix} + \begin{bmatrix} C_{mm} & C_{mn} \\ C_{nm} & C_{nn} \end{bmatrix} \begin{bmatrix} \dot{v}_m \\ \dot{v}_n \end{bmatrix} + \begin{bmatrix} K_{mm} & K_{mn} \\ K_{nm} & K_{nn} \end{bmatrix} \begin{bmatrix} v_m \\ v_n \end{bmatrix} = \begin{bmatrix} Q_m \\ Q_n \end{bmatrix} \tag{6.2}$$

Subscript m and n are referred to master *dofs* (describing the static modes) and modes of the free structure, once fixed the master *dofs* (the component modes), respectively.

In a purely static case, no velocities and accelerations are present:

$$\begin{bmatrix} K_{mm} & K_{mn} \\ K_{nm} & K_{nn} \end{bmatrix} \begin{bmatrix} v_m \\ v_n \end{bmatrix} = \begin{bmatrix} Q_m \\ Q_n \end{bmatrix} \tag{6.3}$$

To evaluate the displacements of slave nodes, then:

$$[K_{nm}]\{v_m\} + [K_{nn}]\{v_n\} = \{Q_n\} \tag{6.4}$$

$$\{v_n\} = [K_{nn}]^{-1}\{Q_n\} - [K_{nn}]^{-1}[K_{nm}]\{v_m\} = \{v_n\}^n + \{v_n\}^m \tag{6.5}$$

In the case of no load applied ($\{Q_n\} = 0$) in the slave *dofs*, it holds:

$$\{v_n\} = -[K_{nn}]^{-1}[K_{nm}]\{v_m\} = [B]\{v_m\} \tag{6.6}$$

The application of matrix B to the mass matrix (that means solving the system only for the v_m coordinates) brings to a non-negligible approximation of the mass matrix itself, so, to characterize dynamically the system, *component modes* are required. *B* is called in the literature "boundary node functions" or "boundary modes". *B* is capable then of describing the coupling between rigid modes or even static displacements of master *dofs* to the displacement of inner ones, representing then the static part of the condensed system, a sort of "superelement".

Mode shapes of the structure, once constrained master *dofs*, are computed: master dof displacements are imposed equal to 0 and an eigenvalue problem of the remaining free structure, containing all the slave *dofs*, is solved; in this way, a modal basis is extracted, also called the *Craig-Bampton basis* or "*Component Mode Synthesis*" or "*Fixed base mode shapes*". Damping can be neglected for extracting this base, and it follows:

$$[M_{nn}]\{\ddot{v}_n\} + [K_{nn}]\{v_n\} = 0 \tag{6.7}$$

With harmonic response $Vn = \phi_n q_m e^{i\omega_0 t}$, the eigenvalue problem is solved in this form:

$$([K_{nn}] - {\omega_0}^2[M_{nn}])\{\phi_{nn}\} = 0 \tag{6.8}$$

$\{vn^n\}$ can be then described by a superposition of some of these undamped modes, through a set of generalized coordinates, stored in a column vector of dimension n, named from now on as $\{u_n\}$. $[\Phi]$ is *Craig-Bampton basis* and is defined as the matrix whose columns are the selected fixed mode shapes.

$$[\Phi] = [\phi_{nn\_1}, \phi_{nn\_2}, \dots, \phi_{nn\_n}] \tag{6.9}$$

$$\{v_n\}^n = [\Phi]\{u_n\} = \sum_{j=1}^{n} \phi_{nn\_j} u_{n\_j}\,. \tag{6.10}$$

As a rule of thumb, the threshold of the number of modes is set at the mode whose associated angular frequency corresponds to at least 1.5 the maximum angular frequency (measured then in rad/s) of any excitation applied to the system.

Having N_{dof} degrees of freedom, the following coordinate transformation is performed, with $\{q\}$ representing the reduced coordinates, while $\{v\}$ is the same in equation (6.2):

$$\{v\} = [H]\{q\} \tag{6.11}$$

v contains all the N_{dof} physical coordinates of the structure. H is the transformation matrix, relating Craig coordinates to physical ones.

The vector of reduced coordinates $\{q\}$ is defined in this way:

$$\{q\} = \begin{Bmatrix} u_m \\ u_n \end{Bmatrix} \tag{6.12}$$

Of course, $\{v_m\} = \{u_n\}$ and there is no influence of the slave *dofs* on the master *dofs*. $\{u_n\}$ are the modal coordinates defined in equation (6.10).

The explicit form of $[H]$ is obtained:

$$\{v\} = \begin{Bmatrix} v_m \\ v_n \end{Bmatrix} = [H]\{q\} = \begin{bmatrix} I & 0 \\ B & \Phi \end{bmatrix} \begin{Bmatrix} u_m \\ u_n \end{Bmatrix} = [H]\{q\} \tag{6.13}$$

$[H]$ is not a squared matrix: $[I]$ is of dimension mxm, $[\Phi]$, defined in equation (6.6), is nxn and $[B]$, defined in equation (6.9), is nxm. $[H]$ is then of dimension $N_{dof} \times (n+m)$.

Since matrix $[H]$ does not depend on time, it holds

$$\{\dot{v}\} = [H]\{\dot{q}\} \text{ and } \{\ddot{v}\} = [H]\{\ddot{q}\} \tag{6.14}$$

Substituting these equations into $[M]\{\ddot{v}\} + [C]\{\dot{v}\} + [K]\{v\} = \{Q\}$ (6.1),

$$[M][H]\{\ddot{q}\} + [C][H]\{\dot{q}\} + [K][H]\{q\} = \{Q\} \tag{6.15}$$

Pre-multiplying by the transpose, it brings to:

$$[H^T][M][H]\{\ddot{q}\} + [H^T][C][H]\{\dot{q}\} + [H^T][K][H]\{q\} = [H^T]\{Q\} \tag{6.16}$$

that results in:

$$[m]\{\ddot{q}\} + [c]\{\dot{q}\} + [k]\{q\} = \{F\} \tag{6.17}$$

This is a squared system of equations of $(m+n)\times(m+n)$. $[m], [c]\ and\ [k]$ are computed once and can be used in integration without changing them, because they do not depend on time neither on the state. $\{F\}$ can depend on both the time and generalized state because of the nonlinearity. In state space form, this equation becomes:

$$\{\ddot{z}\} = [A]\{z\} + \{F_{craig}\} \tag{6.18}$$

$$\{\ddot{z}\} = \begin{Bmatrix}\ddot{q}\\ \dot{q}\end{Bmatrix},\ [A] = \begin{bmatrix}-[m]^{-1}[c] & -[m]^{-1}[k]\\ [I] & [0]\end{bmatrix},\ \{z\} = \begin{Bmatrix}\dot{q}\\ q\end{Bmatrix},\ \{Fcraig\} = \begin{Bmatrix}[m]^{-1}\{F\}\\ [0]_{(m+n)x1}\end{Bmatrix} \tag{6.19}$$

In the particular case presented, master *dofs* are chosen as the axial displacement of the rotor and the two rotations at the thrust bearing position, denotated previously as θ and ψ, because these ones are quantities of interest and because forces and moments are associated to these *dofs*. Displacements in the x and z at the two unbalanced nodes also are chosen, because energy is put in the system there. Radial displacements of journal bearings are not chosen as master *dofs*: the reacting forces at the bearings are consider through their linearized coefficients, which depend only on the turbine angular velocity. Once calculated, they are constant through all the simulation range, since the rotational speed of the turbine is fixed; they are incorporated within the matrices $[c]$ and $[k]$.

As initial conditions for this problem, it holds: $[H]\{q_0\} = x_0$ and $[H]\{\dot{q_0}\} = \dot{x_0}$, where x_0 and $\dot{x}_0$ are the initial generalized displacements and velocities, with the coordinates repartitioned as described before. In order to evaluate $\{q_0\}$, since $[H]$ matrix is generally not square and cannot be inverted, Moore-Penrose left pseudo-inverse is required: pre-multiplying both equation members times the transpose of $[H]$ and the inverse of $[H^T][H]$:

$$([H^T][H])^{-1}[H^T][H]\{q_0\} = ([H^T][H])^{-1}[H^T]x_0 \tag{6.20}$$

It leads to:

$$\{q_0\} = ([H^T][H])^{-1}[H^T]x_0 \tag{6.21}$$

The same is valid for the initial velocities.

The force is computed in each time step in physical coordinates and then brought back to Craig coordinates by the transformation:

$$\{F\} = [H^T]\{Q\}. \tag{6.22}$$

The dimension of the generalized state, at the very end, is $2 \times (m + n)$. Physical coordinates are obtained applying the following transformations:

$$\{\dot{v}\} = [H]\{\dot{q}\} \text{ and } \{v\} = [H]\{q\} \tag{6.23}$$

6.3 Validation

Simulations using dynamic condensation with varying numbers of modes are compared to a time-domain case where a 2.5 kN axial force at 20 Hz acts along the shaft, while previously mentioned unbalances provide radial excitation. The total duration of 5.5 seconds allows the system to reach steady state.

Model reduction significantly reduces computation time: solving the full system takes about 21 hours, whereas the reduced model with 20 modes requires only 14.7 minutes. To assess the impact of model order, simulations with 20, 30, and 40 modes were performed. The corresponding results are presented in *Table 6.2*.

Number of modes considered	Simulation time
20	14.7 min
30	28.6 min
40	34.7 min

Table 6.2: Simulation time for different numbers of modes considered

At this point, errors are computed to evaluate the performance of Craig reduction in reproducing the time history. The reference condition used for error assessment is obtained from the integration of the full, unreduced system. To properly assess the magnitude of the absolute error, it is plotted alongside the reference solution for selected degrees of freedom, at each time instant. The plot features two y-axes: the left axis represents the absolute error, while the right axis represents the reference values, each with their respective units of measurement.

However, analysing only the absolute error is not sufficient, especially when large differences in order of magnitude are present. In such cases, the relative error provides a more meaningful insight, but has its own limitation: when the reference value approaches zero, the relative error becomes very large and potentially misleading. To prevent such distortions, a threshold is set for the reference value. For

the reference values falling below this threshold, the corresponding relative error is not plotted. In such cases, it is more appropriate to consider only the absolute error.

Like the absolute error, the relative error is also plotted together with the reference values, using two separate y-axes. This allows the reader to understand both why certain relative error values are missing and what the true values are in those cases.

Finally, to directly compare the absolute and relative errors at the same time points, subplots have been created. This visualization facilitates a more thorough analysis of cases where the absolute error is large, but the relative error is small, and vice versa, enabling a comprehensive evaluation of the error.

An example is provided in *Figure 6.1*, illustrating that the error associated with one of the master degrees of freedom remains minimal even when only a few modes-such as the 20 used in this case are employed.

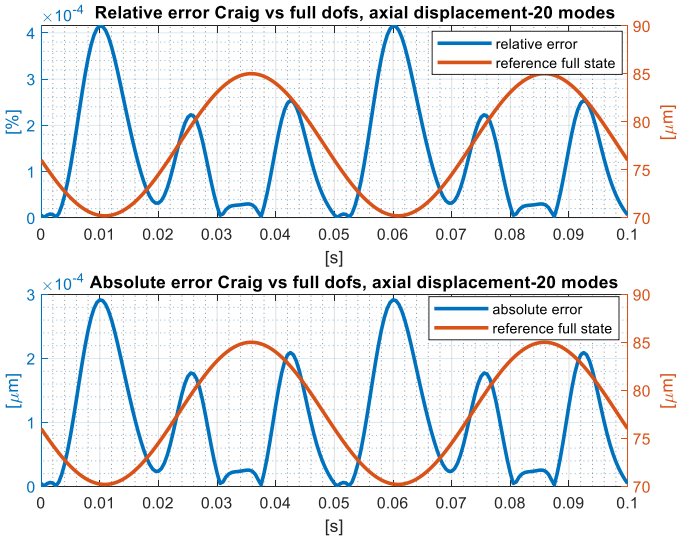

Figure 6.1: Craig reduction (20 modes) compared to complete model considered as reference, in terms of relative error (above) and absolute error (below) of axial displacement

The evaluation can be performed for all degrees of freedom. However, for brevity, only a selection of *dofs* is represented: radial displacement z of third journal bearing and angular velocity $\dot{\psi}$ at the fist journal.

Initially, 20 modes are considered. In this case, relative errors exceed 35%, although the absolute error remains an order of magnitude lower than the reference (10^{-6} rad). Regarding the angular velocity about the vertical axis at the first journal, the relative error often exceeds 50%, with the absolute error and the reference value

being of the same order of magnitude (10^{-3} rad/s). This clearly indicates that retaining only 20 modes is insufficient.

A significant improvement is observed when the reduction is performed with 30 modes. The absolute error in the radial displacement z at bearing 3 drops to about 10^{-7} rad approximately an order of magnitude lower than the reference, and relative errors mostly stay below 20%, validating the accuracy of the approximation.

For the angular velocity $\dot{\psi}$ at bearing #1, absolute errors are about one order of magnitude smaller than the reference. However, closer inspection reveals that when the reference value is approximately 0.5 mrad/s at 0.025 s, the relative error rises to 70%, which raises doubts about the overall accuracy. The resulting errors are still then quite large in some cases, although they suggest that increasing the number of modes further is the correct approach.

Finally, reduction is performed considering 40 modes. In general, the relative error in the radial displacement z at the third bearing remains well below 20, except when the reference values are particularly low. The absolute error is roughly two orders of magnitude smaller than the corresponding reference value. For the angular velocity $\dot{\psi}$ at journal #1, the relative error is consistently below 10%, provided the reference value is not too small. Absolute errors are almost two orders of magnitude lower than the reference. As for $\dot{\psi}$ at the thrust bearing, the error remains below 10% in most cases. This is largely due to the fact that ψ is a master degree of freedom.

Based on these results, summed up in *Table 6.3*, it can be concluded that the optimal configuration for minimizing approximation error is the one adapting 40 modes. This results in a cutoff frequency of 1000 Hz, defined as the highest damped frequency of the modes. Such a high-frequency cutoff is necessary to accurately capture both physical and numerical transients that occur at the start of any simulation. During this initial transient phase, high-frequency content may be generated, which can lead to divergence errors or numerical instability if not properly accounted for. It is also worth noting that errors in velocities tend to be slightly higher due to amplification effects in higher-order derivatives, since errors scale with vibration frequency. Nonetheless, they generally remain below 20%.

Number of modes	Radial displacement z (bearing 3)	Angular velocity (bearing 1)
20	Absolute error ≈ 10^{-6} rad Relative error up to 35%	Absolute error ≈ 10^{-3} rad/s Relative error >> 50%
30	Absolute error ≈ 10^{-7} rad Relative error < 20%	Absolute error ≈ 10^{-4} rad/s ~70% relative error at 0.025 s
40	Absolute error = 10^{-7} rad Relative error < 10%	Absolute error ≈ 10^{-5} rad/s Relative error < 10%

Table 6.3: comparison of the errors varying the modes

7 Artificial Neural Network

7.1 Introduction

Artificial Neural Networks (ANNs) are advanced computational tools that have seen remarkable development in recent years. Grounded in solid mathematical foundations, they are widely applied across various domains, from ICT to engineering, offering valuable support to human operators, particularly in tasks that are repetitive in nature. Further details can be found in [25] and [26].

An ANN is a computer-based system inspired by the functioning of the human brain, where different neurons are connected among each other. A visual representation is provided in *Figure 7.1* .It is capable of processing large volumes of data to abstract and generalize concepts. Starting from a limited set of known cases, it attempts to derive a general model that encompasses a broader range of possible situations. This ability to generalize allows for a reduction in the number of experiments needed, as the ANN can infer untested cases from those it has been trained on.

The learning process involves analysing input data to construct a model that captures the underlying behaviour of a given phenomenon. Once trained, the network can also predict outcomes for new, unseen data. Depending on their design, some networks operate quantitatively, handling numerical inputs and outputs, while others function qualitatively, classifying or interpreting complex inputs such as images, speech, or text. This work focuses on the former type: networks designed for numerical data.

To clarify this concept, consider a case where two variables are dependent, but the exact nature of their relationship is unknown, since it could be linear, nonlinear, or otherwise. Using a dataset containing multiple known values, the ANN can derive an abstract mathematical model describing the relationship. This model can then be used to predict outcomes even for data points not included in the original dataset. Although this is similar to interpolation, the underlying mechanisms of an ANN differ significantly.

The complete process can be broken down into four main phases:

1. Dataset preparation: compiling a collection of known cases, typically from experiments.
2. Dataset presentation: feeding the data into the ANN.
3. Training: enabling the network to learn from the data and construct a representative model.
4. Validation and testing: assessing the model ability to generalize and make accurate predictions.

At the heart of this methodology is bioinspired training, which mimics human learning. The network is composed of interconnected nodes called *neurons*, organized into layers. Each neuron receives inputs from neighbouring neurons, processes them through an activation function, and outputs the transformed information. This layered architecture and learning mechanism form the basis for the network capacity to model complex systems.

A sufficiently deep network, comprising enough layers and equipped with appropriate nonlinear activation functions, can theoretically approximate any continuous function. Each input to the network is multiplied by a weight and adjusted by adding a bias term. The output of a neuron in one layer serves as the input for neurons in the subsequent layer. Ultimately, the output of the final layer represents the output of the entire network.

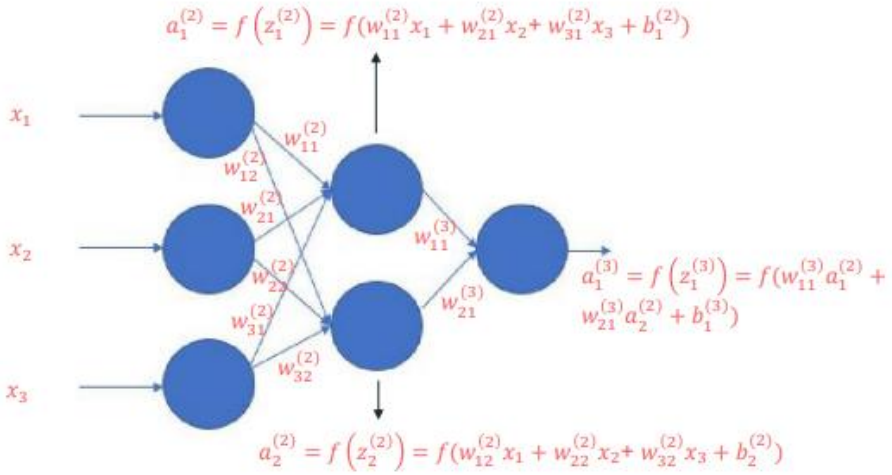

Figure 7.1: schematic representation of the working principle of an ANN

Training process is divided in epochs and each epoch is passed when all batches of the dataset are investigated. Weights and bias are iteratively recomputed to minimize the error of the network and increase the precision of the model, through a back propagation algorithm:

$$w_k \to w'_k = w_k - \eta \frac{\partial L}{\partial w_k} \tag{7.1}$$

$$b_l \to b'_l = b_l - \eta \frac{\partial L}{\partial b_l} \tag{7.2}$$

where $\eta = \epsilon / ||\nabla L||$ is the learning rate.

Steps of the algorithm:

1. Input X: set the corresponding activation $a^{(1)}$ for the input layer.
2. Feedforward: for each $l = 2,3, \dots, L$ compute $z^{(l)} = w^{(l)} a^{(l-1)} + b^{(l)}$ and $a^{(l)} = f\left(z^{(l)}\right)$.
3. Output error $\delta^{(l)}$: compute the vector $\delta^{(l)} = \nabla_a L \odot f\left(z^{(l)}\right)$.
4. Backpropagate the error: for each $l = L-1, L-2, \dots, 2$ compute $\delta^{(l)} = \left(w^{(l+1)}\right)^T \delta^{(l+1)} \odot f'\left(z^{(l)}\right)$.
5. Output: the gradient of the cost function is given by $\frac{\partial L}{\partial b_j^{(l)}} = \delta_j^{(l)}$ and $\frac{\partial L}{\partial w_{jk}^{(l)}} = a_k^{(l-1)} \delta_j^{(l)}$.

When the error is sufficiently small the network is trained.

It is important to clarify the distinction between training, validation, and test datasets. The training dataset is a substantial portion of the overall dataset and is used to adjust the network's internal parameters during the learning process. The test dataset, by contrast, is not used during training. It serves exclusively to evaluate the performance of the trained network, providing insight into its generalization ability, how well it performs on previously unseen data. The validation dataset is often a subset of the training data and is used during training to monitor the model's performance and help prevent overfitting. It provides feedback on how well the network is learning and whether the learning process is proceeding correctly. Monitoring the errors associated with training, validation, and test datasets is essential, as will be further discussed. For example, if none of these errors decrease after a certain number of epochs, it may indicate a vanishing gradient problem.

Another common issue is overfitting, which becomes apparent when only the training error continues to decrease, while validation and test errors stagnate or increase. These two issues will be addressed in more detail in the following sections.

Various algorithms and toolboxes are available to automatically implement an artificial neural network (ANN). In this work, the MATLAB Deep Learning Toolbox is used. Below is a list of parameters and components that the user can define or modify:

1. Activation function: Defines the input-output relationship of a single neuron and has a significant impact on the behaviour of the entire network. Common choices include sigmoid, ReLU, and tanh functions.
2. Number of layers and neurons: The network architecture determines its expressive power and generalization capability. Increasing the number of neurons and layers typically enhances performance, but at the cost of higher computational complexity and potential risk of overfitting.
3. Loss function: This is the metric used to evaluate the network's performance by quantifying the error between predicted and actual values. It guides the adjustment of weights and biases during training. A common example is the Mean Squared Error (MSE).
4. Training algorithm: Determines how the network updates its parameters during learning. The choice of algorithm influences convergence speed, stability, and final accuracy. Popular options include Levenberg-Marquardt and Bayesian Regularization.

Naturally, even when all parameters are properly configured and optimized, the quality of the training process heavily depends on the quality of the dataset. A dataset that is too small, unbalanced, or poorly representative of the problem space will inevitably result in a low-performing network and inaccurate predictions. Simply put, a network cannot learn effectively from poor-quality input data.

Chatterton and Pennacchi in [27] use the net to predict static and dynamic characteristics of a TPJB, in order to reduce the flow rate, granting safe conditions.

Katsaros KP, Nikolakopoulos PG. in [26] develop a performance prediction model for hydrodynamically lubricated tilting pad thrust bearings operating under incomplete oil film with the combination of numerical and machine-learning techniques.

In this work, an artificial neural network (ANN) is employed to predict the behaviour of the thrust bearing. The evaluation of hydrodynamic forces in various configurations is highly time-consuming, primarily due to the nonlinearity of the Reynolds equation, which requires iterative numerical methods to solve. Moreover, no analytical relationship exists between these forces and the bearing position or velocity. ANN can be then conveniently used: a relatively small set of representative

cases is simulated and used to train and validate the network. Once trained, the ANN can rapidly estimate hydrodynamic forces in fractions of a second, effectively acting as a fast-response interpolator. The quality of the ANN predictions depends significantly on its architecture and training algorithm. Adjusting these elements can notably improve output accuracy, making the model suitable for practical use. However, selecting the optimal configuration is not straightforward: few definitive guidelines exist, and in many cases, a trial-and-error approach proves more effective than purely theoretical design methods.

7.2 Net for force and moments predictions

A fully connected feed-forward neural net is chosen. The objective fully means that each neuron of a layer is connected to all the neurons of the previous or following layer. These regression numeral nets are widely used, because of their simplicity less demanding computational resources with respect to other nets, like recurrent or convolutional ones. The Levenberg Marquardt Algorithm is selected for the training. The datasets are split into training, validation, and testing with these ratios: 0.80/0.15/0.05. The mean squared error is assumed as the loss function, the hyperbolic tangent as the activation function for the hidden layer and the initialization by Nguyen and Windrow is selected for initialization of the weights. Nguyen and Windrow initialization helps preventing from vanishing gradient and speeds up the convergence. The input and output parameters are normalized between -1 and 1 considering the values of the training dataset. Normalization helps during training. For the output layer, simple linear activation function was used. The performance of the net is evaluated by means of 30 random points. Once the network has been trained and created, it is stored as a variable in a *.mat* file. This file is loaded inside a MATLAB function. Predictions are done according to the following steps:

1. Input data are normalized, considering the same ranges used during training.
2. The net outputs normalized values.
3. The outputs are denormalized, considering the output ranges during training, to have quantities with physical meaning.

The mean square error, defined in normalized output, is defined in this way:

$$MSE = \sum_{i=1}^{nout} \frac{1}{nout} \sum_{j=1}^{npoints} \frac{1}{npoints} (\widetilde{y_{ij}} - y_{ij})^2 \qquad (7.3)$$

where $\widetilde{y_{ij}}$ is the prediction of the net, whereas y_{ij} is the true value.

Two main methods for training are investigated:

- Levenberg–Marquardt (trainlm), that tries to minimize the MSE at outputs

- Bayesian regularization (trainbr), that tries to minimize the MSE at outputs and the weights.

Generally, trainlm is faster than trainbr, but can provide a net able to predict very well only some values, also because it is prone to overfitting. Trainbr is instead much slower, but capable of predicting well in average.

Early stopping has been adopted by interrupting the network training when the validation error does not improve significantly over 100 epochs, in order to prevent overfitting. Additionally, training is stopped when the gradient falls below $2 \cdot 10^{-4}$ to avoid unnecessary computation in the presence of vanishing gradient.

Some consideration can be drawn.

- An excessive number of neurons may lead to overfitting, a condition where the training error continues to decrease while validation and test errors remain constant. This phenomenon can also stem from an insufficiently large dataset. In such cases, the network tends to assign disproportionately large values to weights and biases, thereby losing its generalization capability and effectively memorizing only a limited subset of the data. Techniques such as Bayesian regularization, dropout, or L2 regularization can be employed to mitigate this issue.
- The quality and representativeness of the dataset are of fundamental importance. A robust approach to effectively sampling the input space involves combining Latin Hypercube Sampling (LHS) with a full factorial design, which helps to capture the variability of the system across the entire domain.
- Another critical challenge is the vanishing gradient problem, where error signals fail to propagate efficiently through the network during training. This typically occurs in deep architectures where the gradients diminish across layers, or when activation functions such as the sigmoid are used, due to their near-zero derivatives at extreme input values. The issue may also arise from poorly initialized weights, particularly when values are too small. Proper weight initialization, along with the selection of suitable activation functions (e.g., ReLU), can help alleviate this effect.
- Finally, it is important to note that the trained neural network remains valid only within the domain defined by the training data and the specific system configuration. Consequently, when evaluating scenarios outside this domain, such as different runner diameters or reduced clearances, a new network must be trained to ensure reliable predictions.

7.3 Net limitations

It must be reminded that pads are considered always in equilibrium positions because their dynamics is considered much faster than the one of the runner.

The six input variables cannot assume arbitrary values due to physical constraints inherent to the system. For instance, the axial displacement of the runner, assumed to be oriented vertically with no angular misalignment, cannot exceed ± 160 μm, where the clearance is ± 175 μm. Exceeding this limit would result in unacceptably high pressures that surpass material capabilities. This limitation is further accentuated by the mechanical configuration of the system: the pads, which are free to rotate about their pivots to balance the axial load, may come into contact with the runner if it approaches them too closely. In such scenarios, extremely high pressures are generated, producing large restoring forces or moments that effectively prevent the system from reaching such configurations. Moreover, under these conditions, the numerical solver fails to reach convergence during the equilibrium computation of the pads. This often leads to unphysical results, such as negative oil film thicknesses. Additionally, the external excitations required to force the system into such extreme states would significantly exceed those encountered in practical applications. Consequently, the axial position of the runner is constrained within a physically meaningful range, bounded between -160 μm and $+160$ μm.

Even though ϑ_{lim} and ψ_{lim} are assumed to be equal to 2×10^{-4} rad (twice the static rotation caused by deformation under no load), another consideration concerns the possible rotations. Initially, a simplifying assumption can be made by referring to the drawing in *Figure 7.2*.

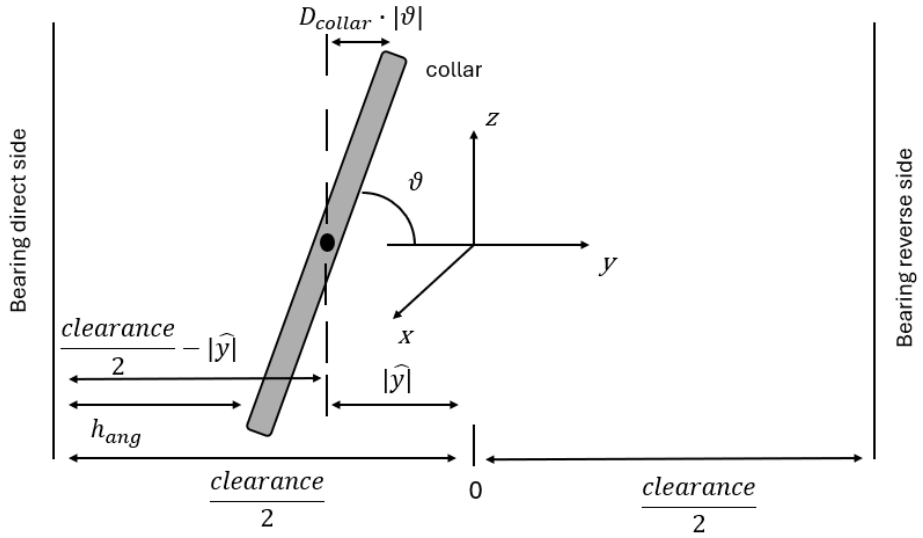

Figure 7.2: main geometrical parameters of the thrust bearing

$|\hat{y}|$ represents the axial displacement of the runner. A deeper analysis would require considering also the thickness of the runner, but it can be neglected, since it is much smaller than the radius of the runner and the clearance.

It is clear that h_{ang} should be higher than h_{min}. The value h_{min} has been imposed to 5 μm, although it gives rise to numerical instabilities due to the high generated forces. All the simulations are doubled checked and they are labelled as "FAILED" when the critical condition$h_{ang} \leq h_{min}$ happens.
The runner is free to tilt around two axes orthogonal to each other, the rotations are small and can be represented by vectors. Given that the runner is axially symmetric, any possible total allowed rotation is given by:

$$\phi_{eq} = \sqrt{\vartheta^2 + \psi^2} \tag{7.4}$$

Considering:

$$h_{ang} = \frac{cl}{2} - |\hat{y}| - \frac{D_{collar}}{2} \left| \phi_{eq} \right| \leq h_{min} \tag{7.5}$$

The mathematical expression for computing then the maximum angle ϕ_{eq} is then available.

Since $\phi_{eq} = \sqrt{\vartheta^2 + \psi^2}$ and ϑ and ψ are independent, this implies that ψ could depend on ϑ or viceversa. Therefore, it is necessary to fix one rotation or impose them equal when building the plans, if the threshold of h_{min} is exceeded. It has been decided to impose then $\vartheta = \psi = \vartheta_{eq}$, resulting in:

$$\phi_{eq} = \sqrt{2}\, \vartheta_{eq} \tag{7.6}$$

The adjusted limit

$$\vartheta_{eq\_lim} = \frac{\sqrt{2}\,(\frac{cl}{2} - |\hat{y}| - h_{min})}{D_{collar}} \tag{7.7}$$

substitutes ϑ_{lim} and ψ_{lim} in the plan creation, but only locally in the FAILED conditions. The very same state is assumed except for the rotations, whose values are computed considering the same current level (in the factorial plan) or the same coefficient (for Latin or random plans) applied to a range $[-\vartheta_{eq\_lim}, \vartheta_{eq\_lim}]$ instead of $[-\vartheta_{lim}, \vartheta_{lim}]$ for ϑ or $[-\psi_{lim}, \psi_{lim}]$ for ψ.

It should be noted that this adjustment to the plan does not guarantee that the specific configuration will not result in FAILED condition: the concurrent rotation of the pads could further reduce the minimum oil film thickness at the pads, making it

smaller than the reference value h_{min}, thus rendering that configuration unusable. However, these conditions are quite rare and they can be easily managed

7.4 Velocities estimation

Very rough estimations have been made for the velocities. The main drawback is that they are theoretically defined over the entire range from $-\infty$ to $+\infty$. Some approaches are present in the literature: Chasalevris and Louis in [28] propose a change of variables for radial bearings, but this method is not suited for thrust bearings. Novotný in [29] considers only positive axial velocities up to a not well-defined threshold value.

The basic idea behind these limit values is that vibrations when no static load is applied to the runner occur at frequencies no higher than 30 Hz in the axial direction and more than 60 Hz in the radial direction. Assuming harmonic motion, the maximum velocity can be estimated as the displacement or rotation multiplied by the angular frequency $\omega = 2\pi f$. Equation $\dot{\vartheta} = 60 \cdot 2 \cdot 10^{-4} \cdot 2 \cdot \pi = 0{,}08\, rad/s$ (7.8) is used to compute the maximum angular velocity, given that the maximum allowed rotation of approximately 2×10^{-4} rad when the runner is at the middle of the clearance by geometrical considerations.

$$\dot{\vartheta} = 60 \cdot 2 \cdot 10^{-4} \cdot 2 \cdot \pi = 0{,}08\, rad/s \tag{7.8}$$

Applying a safety factor, the value has been conservatively increased to 0.15 rad/s. Since there is no compelling reason to assume a different limit for $\dot{\psi}$, the same threshold has been applied. The axial velocity is computed according to (7.9), considering that, when the runner is centred, the allowed stroke is approximately 175 μm.

$$\dot{y} = 2 \cdot \pi \cdot 30 \cdot 175 \cdot 10^{-6} = 0.03\, m/s \tag{7.9}$$

and with the same logic a safety margin has been considered, leading to 0.4 m/s. In the case where the load is -200 kN and thus the position is approximately -100 μm, the allowed maximum stroke of 75 μm. The eigenfrequency is at 50 Hz more or less, leading to maximum velocity of 0.02 m/s. One could think at this point that the value for the rotations can be critical. Nevertheless, a combined effect of rotations of order of 2×10^{-4} rad at both frequencies (60 Hz and 50 Hz) is not possible because of the very high damping in correspondence of the direct side. It can therefore be concluded that the established upper limit is safe, even in this configuration.

7.5 Dataset

Building a correct design plan is of paramount importance. There is a trade-off between the accuracy in describing the full parameter space and the overall simulation time, especially considering that each simulation may take on average around one minute, depending on the available computational resources. Parallelization can help address this issue by evaluating multiple configurations simultaneously, effectively speeding up the execution by a factor equal to the number of cores available.

- Full factorial plan. This experimental design approach involves discretizing each variable across a defined range and systematically evaluating every possible combination of these discrete values. The discrete values that each variable assumes are referred to as levels. Given m variables each with n levels, the total number of experimental runs or simulations required in a full factorial design is n^m.

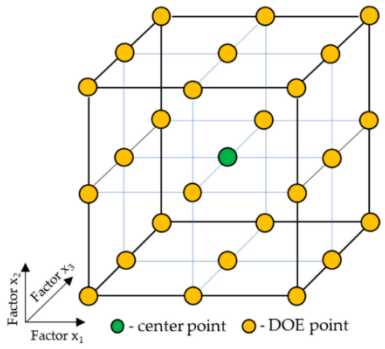

Figure 7.3: schematic representation of a full factorial plan with 3 factors

One major limitation of this approach is that each variable is restricted to a finite set of discrete values. Consequently, models like neural networks trained on such datasets tend to perform well only at those specific points included in the training data, while exhibiting limited ability to generalize across the continuous domain. Therefore, the full factorial plan alone may not be sufficient for robust model training. In this study, the *fullfact* function provided by MATLAB has been employed to generate the design matrix.

- Latin hypercubic sampling. Each variable's range is divided into a predefined number of equal sub-intervals. Within each sub-interval, a random value is selected. These values are then randomly permuted independently for each variable. The final sampling plan is constructed by combining one value from each variable exactly once: once a variable value is selected to form a plan point, it cannot be used again. For example, in a Latin Hypercube Sampling

with 8 levels (LHS8), each variable is sampled in such a way that the probability of selecting a value within any given sub-interval is exactly 1/8, ensuring uniform marginal distributions across the sampling space.

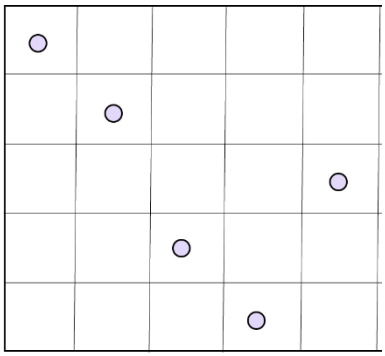

Figure 7.4: schematic representation a latin hypercube sampling

This simplified representation refers to the two-dimensional case. However, the underlying concept remains applicable in the multi-dimensional (nD) context. The Latin Hypercube Sampling (LHS) approach offers more uniform and efficient coverage of the parameter space and is widely used for this reason. By combining the full factorial and LHS plans, a more comprehensive and structured exploration of the hyperspace is achieved. The *lhsdesign* function provided by MATLAB has been used to generate the Latin Hypercube plan.

To evaluate the network predictive capabilities on previously unseen data, an independent test dataset was generated using MATLAB rand function. The way the input space is covered through this random sampling is illustrated in *Figure 7.5*.

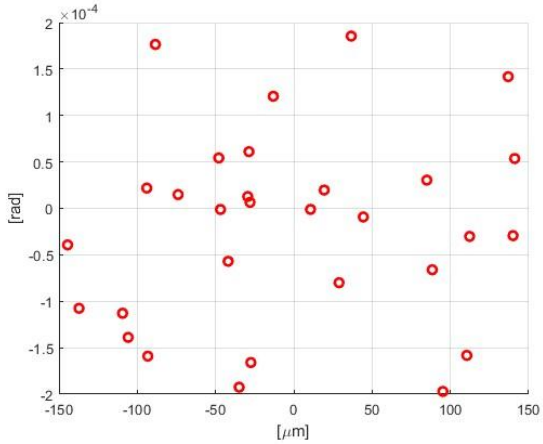

Figure 7.5: example of a plan, varying axial displacement and tilting angle

The plan is built, also considering that the minimum number of simulations should be 30 times higher than the number of the parameters involved in the net, as a rule of thumb the number of parameters can be computed as:

$$\sum_{i=1}^{l-1}(n_i n_{i+1} + n_{i+1}) \tag{7.10}$$

where n is the neuron number, I represents a layer and l number of layers. Simulations associated with the factorial plan that result in FAILED conditions are excluded from the training set. Ultimately, approximately 130000 valid samples have been generated: around 80000 using Latin Hypercube Sampling (LHS) and about 50000 from the factorial plan.

It is not feasible to visualize the full hyperspace. Only combinations involving up to three variables can be meaningfully plotted. For example, *Figure 7.6a* and *Figure 7.6b* shows in a 2D plane just the allowed combinations of two variables, while the others could assume in principle a range of values.

It is important for the reader to understand that a single point in the plan may represent just one discretization value per variable. This highlights the strength of such experimental designs: they allow effective coverage of the parameter space without requiring an infinite number of points.

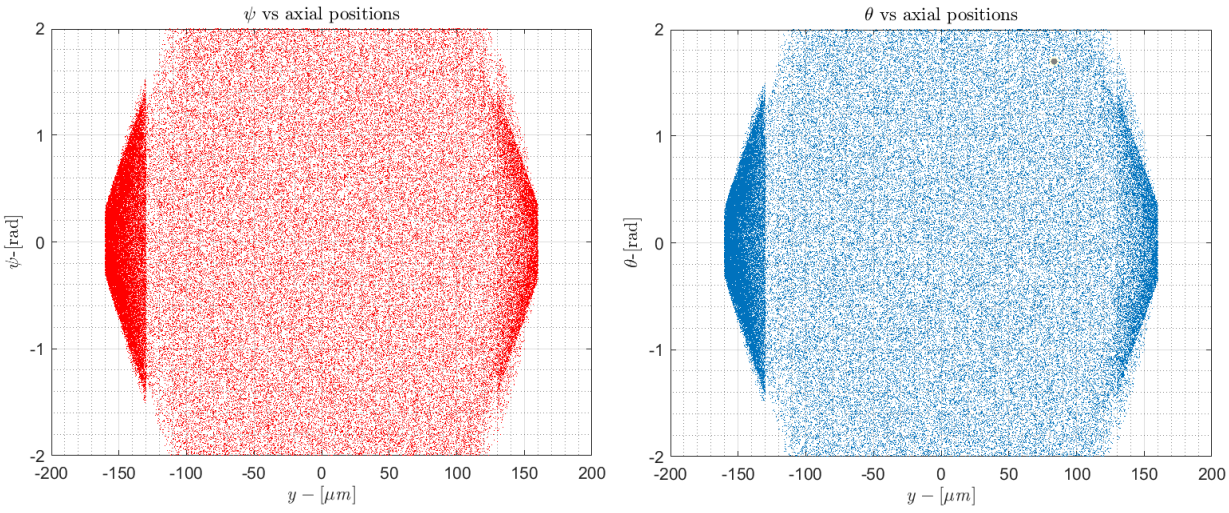

(a) (b)

Figure 7.6: (a) Example of a plan, varying axial displacement y and tilting angle ψ, covering completely the allowable space. (b) Example of a plan, varying axial displacement y and tilting angle ϑ, covering completely the allowable space

The peculiar barrel shape is given by the necessary cuts already explained. The high density of points at the extremes of the axial position is due to the need for increased sampling near the boundaries in order to capture significant nonlinearities. Although

the general approach is to uniformly cover the input space, this refinement has led to improved performance of the neural network.

0-1 normalization is performed according to $X_{normalized\_input} = \frac{X_{input} - X_{min}}{X_{max} - X_{min}}$ (7.11).

$$X_{normalized\_input} = \frac{X_{input} - X_{min}}{X_{max} - X_{min}} \quad (7.11)$$

where X_{max} and X_{min} are the minimum and maximum values of the corresponding variable in the training dataset. The same normalization is applied to the output variables.

When using the net, predictions are denormalized:

$$X_{prediction} = X_{normalized\_output}(X_{max} - X_{min}) + X_{min} \quad (7.12)$$

The normalization between -1 and 1 and the corresponding denormalization are also shown:

$$X_{normalized-input} = 2\frac{X_{input} - X_{min}}{X_{max} - X_{min}} - 1 \quad (7.13)$$

$$X_{deromalized\_output} = 0.5(X_{normalized_{output}} + 1)(X_{max} - X_{min}) + X_{min} \quad (7.14)$$

7.6 Net architecture analysis

All reported MSE values refer to the validation error, which indicates the network's performance during training. All the networks discussed in this section have been trained using the trainbr algorithm.

It can be observed that increasing the number of neurons consistently leads to longer simulation times, as shown in *Table 7.1*, where different architectures are investigated.

Architecture	Training time per epoch
40 40	1 min 41 s
50 50	2 min 45 s
60 60	4 min 40 s
30 30 30	55 s
40 40 40	2 min

Table 7.1: simulation times for some net architectures

It can be noted that, for a fixed number of hidden layers, increasing the number of neurons per layer significantly increases the simulation time. Although the 30-30-30 configuration has more network parameters than the 40-40 setup, the latter requires more time to run. This suggests that the number of neurons per hidden layer is the main factor affecting simulation time. Therefore, to reduce simulation time while maintaining accuracy, increasing the number of hidden layers is preferable.

Table 7.2 illustrates an analysis of MSE error varying the architecture of the net.

Architecture	**Parameters**	**Best MSE validation**
50 50	3053	5.7×10^{-7}
40 40	2043	2.3×10^{-6}
60 60	4263	2.0×10^{-7}
70 70	5673	2.9×10^{-7}
50 40 30	3713	2.0×10^{-7}
64 32 16	3107	1.1×10^{-6}

Table 7.2: MSE validation errors under different architectures

It is evident that, once the number of layers is fixed, the total number of parameters is the main factor making the error reduced, as can be observed when increasing from 40 to 50 to 60 neurons per layer. A similar trend is seen when increasing parameters with three hidden layers. However, exceeding the optimal number of parameters leads to an increase in MSE error due to overfitting, as exemplified by the 70-neuron case showing higher error compared to 60 neurons. The recommendation is then not to exaggerate with neurons.

Increasing the number of hidden layers does not necessarily improve performance when the total number of parameters remains similar, as seen in the comparison between the 50-50 and 64-32-16 configurations. The recommendation is thus to keep the number of hidden layers low and increase the number of neurons per layer. Nevertheless, training time can become very long, so a compromise must be reached.

To increase the allowable number of neurons while avoiding overfitting, the dataset size must also increase accordingly: ideally, the number of training points should be at least 30 times greater than the number of network parameters. However, training with larger datasets significantly slows down the process, so the choice depends on priorities and available resources.

As previously mentioned, Bayesian regularization helps mitigate overfitting. In this analysis, the maximum recommended number of parameters to avoid overfitting is around 4500. For instance, a network with six hidden layers of 30 neurons each

(totalling 4953 parameters) has been trained: the trainlm method reached a threshold gradient with an error of about 1.8×10^{-7}, while trainbr achieved 9.5×10^{-8}.

Increasing the number of layers too much is not always beneficial. For example, a network with 10 hidden layers of 21 neurons (4371 parameters, below the threshold) suffered from vanishing gradient issues, as the error plateaued around 5.8×10^{-7}, higher than in other configurations. Nonetheless, trainlm is faster overall, allowing, for example, a 3-hidden-layer network with 64, 32, and 16 neurons to train in about 1 minute and 20 seconds, compared to 2 minutes and 54 seconds with trainbr.

7.7 Analysis of net errors

In order to understand the effectiveness and the powerful of a net of giving exact predictions even working with 6 inputs, some examples are considered in the following. The errors in the predicted forces and moments are evaluated in the following analyses:

1. Varying y and ϑ, with all other variables set to zero.
2. Varying ϑ and $\dot{\vartheta}$, with $y = -100$ μm and the remaining variables set to zero.
3. Varying $\dot{y}$ and $\dot{\vartheta}$, fixing at $\vartheta = 1 \times 10^{-4}$ rad and $y = 78$ μm, while all other inputs are held at zero.

Figure 7.7a shows the absolute error of force prediction for the case 1). The highest absolute errors on the axial force prediction occur on the direct side, with values reaching nearly 4000 N. However, as shown in the relative error plot below, the maximum percentage error in that region is only 0.65%, making the error acceptable. At 126 μm, the absolute error reaches even 2460 N, but the corresponding relative error is approximately 3.2%, which is still very low. At 110 μm, the absolute error is about 1385 N, but the percentage error indicates that it is not actually significant.

Figure 7.7*b* depicts the corresponding relative errors. Some configurations not shown in the plots exhibit errors greater than 20%, with true force values below 500 N. From the relative error, it can be concluded that the error is acceptable since it remains below 10% in all cases, except when the true force is quite small: at $y = 75$ μm, the relative percentage error exceeds 40%. However, considering the absolute error, the maximum absolute error in this position is 300 N, which can be regarded as acceptable due to the inertia of the shaft. Apart from this, the highest errors occur near the reverse side.

The absolute error in M_z generally stays below 300 Nm, with peaks up to 600 Nm occurring only under conditions that are unlikely in real operation (1.57×10^{-4} rad

and y = -130 μm). Given the rarity of such configurations, these errors are not considered critical.

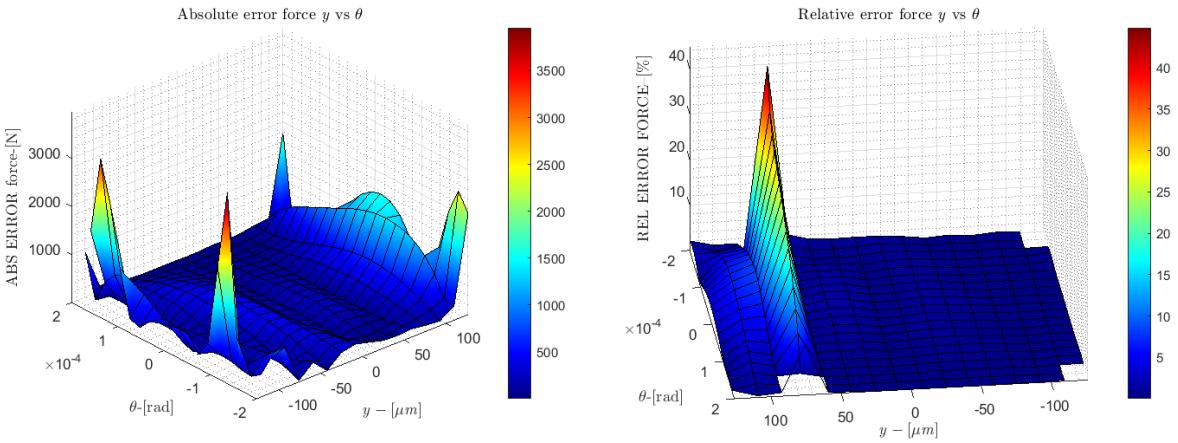

(a) (b)

Figure 7.7: (a) Absolute error of the axial force as a function of y and ϑ. (b) Relative error of the axial force as a function of y and ϑ

CASE 2

The absolute error in M_x remains mostly below 200 Nm, while the relative error stays under 20%, except in rare extreme conditions characterized by both high rotations and angular velocities, where it reaches 50%. Since such scenarios are unlikely in practice, the predictions are considered generally reliable.

CASE 3

The absolute error in axial force predictions remains very low, typically under 70 N where forces are small, and around 360 N when the relative error peaks at 14%. Overall, the relative error stays below 16%, confirming good predictive accuracy.

7.8 Considerations about the net

The first trained network demonstrated good performance up to 130 μm, which was initially chosen as a conservative training range due to known failure issues occurring in the tail regions. However, this range has proven too narrow, as the predictions become unreliable beyond this interval—particularly in scenarios where the system is driven into resonance and the collar displacement exceeds 130 μm, such as in the case where the static axial load is approximately 0 N and the shaft is subjected to axial excitation at 16 Hz. In such cases, the axial stiffness and damping

are relatively low, resulting in significant axial vibrations that bring the collar close to the reverse side. Similar behaviour is observed for negative static axial loads and under resonance excitation, where the collar tends instead to approach the direct side.

Subsequently, the input ranges were expanded, but the prediction quality deteriorated significantly. This is likely due to the strong nonlinearity of the underlying functions, which would require a substantially larger dataset to accurately capture the dynamics and to mitigate issues such as vanishing gradients and overfitting.

Increasing the number of neurons is generally the most effective approach to improve model capacity; however, this leads to significantly longer training times and often causes overfitting, especially when the number of parameters exceeds approximately 30 times the size of the dataset. Moreover, adding more layers helps to better capture nonlinearities, but it introduces the vanishing gradient problem. This problem occurs during backpropagation when the error signals propagated from the output layers toward the earlier layers become progressively smaller. As a result, the gradients associated with neurons in the deeper layers tend to diminish, making their weight updates very small or negligible. This gradient shrinkage effectively slows down or even stops the learning process in these layers, limiting the network's ability to capture complex nonlinear relationships. Consequently, while deeper architectures can in principle model more complex functions, their training is often hampered unless mitigated by specific architectural choices or larger datasets.

Architectures inspired by nested or “matryoshka” structures, with many neurons in the first layers and less neurons in the following can alleviate some of these issues, by combining the positive effects of both directions. However, this possibility can only offer limited improvement and should be considered more as a recommendation than a definitive solution. The recommended approach is to add more points to the dataset, thereby enabling a proper increase in the network’s parameter count without losing net performance.

Nevertheless, larger datasets potentially involving hundreds of thousands more data points require longer training times, which further increases computational costs. Therefore, careful consideration is necessary to evaluate whether such efforts are justified. A potential future development could focus on deepening the investigation of this network, expanding the dataset as much as possible until the percentage errors fall below 2%.

7.9 Interpolator

In this chapter, the use of an interpolator, as alternative to ANN, is proposed, similarly to Chasalevris and Louis in [28].

Due to inherent limitations, it is not feasible to build an interpolator using all six variables simultaneously. Specifically:

- The scatteredInterpolant function in MATLAB supports up to three input variables.
- Although Intern, which performs n-dimensional spline interpolation, could theoretically be used, it presents three major challenges:

    1. It requires a regular grid of data points, which necessitates the use of a dense full factorial plan to populate the space uniformly.
    2. Handling and predicting FAILED conditions are complex. This typically results in a different number of valid samples in each dimension, making it practically impossible to construct a regular grid with consistent resolution across all dimensions.
    3. While limiting the domain might partially mitigate the second issue, doing so introduces risks related to incorrect extrapolation near the boundaries.

Given these difficulties, a reduced interpolator is constructed using only three variables: the axial displacement y and the two rotations at the collar ϑ and ψ. This setup corresponds to interpolating static force configurations, which can then be used to approximate the system behavior under various static loads. The training of the interpolator is carried out using a combined Latin Hypercube Sampling (LHS) and full-factorial design, similar to the approach adopted for the neural network.

To replicate dynamic behaviour, damping coefficients are introduced. These coefficients depend on ϑ, ψ, and y and thus require interpolation. However, rotational values caused by unbalance are typically an order of magnitude smaller than those due to static deformation at the thrust node. Therefore, it is a reasonable simplification to interpolate the damping coefficients as a function of the axial displacement y only, using linear interpolation.

Since the axial displacement y is directly linked to the static axial load, this approach allows for dynamic coefficients to be mapped to any load condition in the range of -200 kN to 50 kN.

Finally, because the damping matrix used in dynamic condensation cannot be updated online, damping contributions are introduced as generalized concentrated forces. This is consistent with the model structure, where the runner state is represented through a generalized master coordinate.

For instance, the term $c_{\psi y}\, v$ is obtained in the same way as $M_{zy} = -c_{\psi y}\, v$, shifting at the right side the term.

The interpolator has been trained on a dataset containing the same number of points as the network, generated by combining Latin Hypercube Sampling (LHS) and a full factorial design. Input and output normalization were applied consistently with the network.

It is also worth noting the differences in average computation times: for a set of 100 configurations, the Reynolds code requires 1 hour and 40 minutes, the network takes 1.72 seconds, and the interpolator only 0.22 seconds. Therefore, it can be concluded that the interpolator is extremely fast in making predictions

7.10 Analysis of interpolator errors

As a reminder, the formulas for absolute and relative error used in the upcoming diagrams are provided below.

$$ERR_{ABS} = \left|X_{predicted} - X_{true}\right| \tag{7.15}$$

$$ERR_{REL}(\%) = \frac{\left|X_{predicted} - X_{true}\right|}{X_{true}}\, 100 \tag{7.16}$$

Prediction errors of the interpolator are evaluated by fixing the rotation angle ψ to 0 at computing the forces and the two moments. The evaluation is carried out over a range where the axial displacement y spans from -160 to 160 μm and the tilt angle ϑ from -2×10^{-4} rad to 2×10^{-4} rad. This is equivalent to computing the static forces using the network, assuming all velocity components are zero. The choice of fixing one variable to zero is discussed in detail in *Chapter 4*, allowing for a clearer interpretation of the problem.

Errors are shown in terms of both absolute and relative values, with respect to the reference values obtained from the Reynolds code.

The absolute error in the force increases towards the two ends of the range, particularly on the direct side, as it can be noted in *Figure 7.8a*. However, a careful evaluation of the relative error is necessary to determine whether these deviations are quantitatively significant. The relative error of the force as a function of y and ϑ is shown in *Figure 7.8b*. The voids in the diagram correspond to conditions where the

absolute value of the true force is less than or equal to 500 N and the relative error exceeds 20%. Overall, the prediction can be considered accurate, as the percentage error remains below 10% across most of the domain, except in the region around $y = 75$ μm, where the true force magnitudes are relatively low. However, even in that area, the maximum absolute error is approximately 70 N, which is still small in practical terms. It can therefore be concluded that the force predictions are reliable.

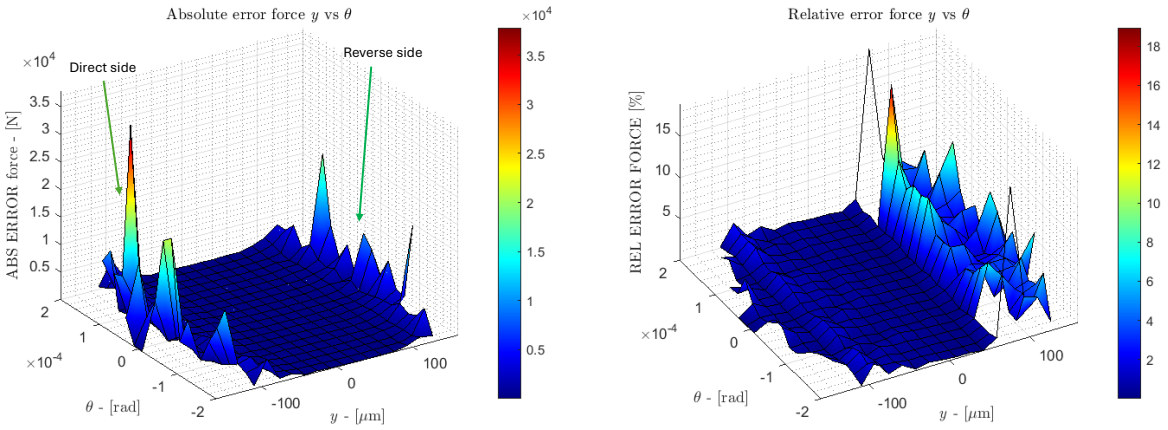

(a) (b)

Figure 7.8: (a) absolute error of the force as a function of y and ϑ; (b) relative error of the force as a function of y and ϑ

The absolute error of the moment M_x is always below 3000 Nm (occurring in the direct side) and remains under 150 Nm within the range y = −75 μm to 110 μm. On the reverse side, the error reaches up to 1700 Nm. The relative error is generally under 6.5% with slightly higher values on the reverse side, but always below 14%.

For M_z ,the absolute error stays below 40 Nm across all configurations, rising to 200 Nm only on the direct and reverse sides. The relative error of M_z is not reported, as the true values are near zero and would lead to misleadingly large percentage errors.

8 Results of the linear model

In this chapter the results of the linearized dynamic analysis are presented. Specifically, the following outputs are included:

- Static deflection and bearing reaction forces
- Campbell diagram (or frequency–speed sensitivity map) and frequency–load sensitivity map
- Root locus diagram
- System response to unbalance and unbalance-induced orbits
- Mode shape visualization

Two different configurations are analysed:

- without the thrust bearing and axial *dof*;
- with the thrust bearing and axial degree of freedom (*dof*) activated.

This comparative approach allows for a detailed assessment of the influence of the thrust bearing and axial dynamics on the overall behaviour of the machine.

Additionally, further investigations are performed, by varying:

- the location of the thrust bearing along the shaft.
- the position and magnitude of the unbalance (by applying it to different nodes).

These variations are intended to evaluate the sensitivity of the dynamic response of the system to changes in these parameters.

It is useful to briefly recall the purpose of the main diagrams used in the analysis.

- Campbell diagram shows the evolution of damped eigenfrequencies of the system as a function of the rotor speed. It helps identify critical speeds.
- Stability map shows the variation of the non-dimensional damping (h-factor), as a function of the static load acting on the thrust bearing.

- Sensitivity map shows the variation of eigenfrequencies as a function of the applied static load.

8.1 Thrust bearing free case

8.1.1 Static deflection and bearing reaction forces

In the initial stage of the analysis, the dynamic coefficients of both stiffness and damping of the four journal bearings are evaluated as a function of the shaft rotational speed; an example is shown *Figure 8.1*.

The direct z terms k_{zz} and c_{zz} (in red in *Figure 8.1*) that are those in vertical are significantly larger than the other coefficients in horizontal x direction. This is due to the high vertical loads acting on the journal bearings. The cross-coupling terms are relatively small, indicating that the bearings are not particularly prone to instability, despite not being of the tilting-pad type.

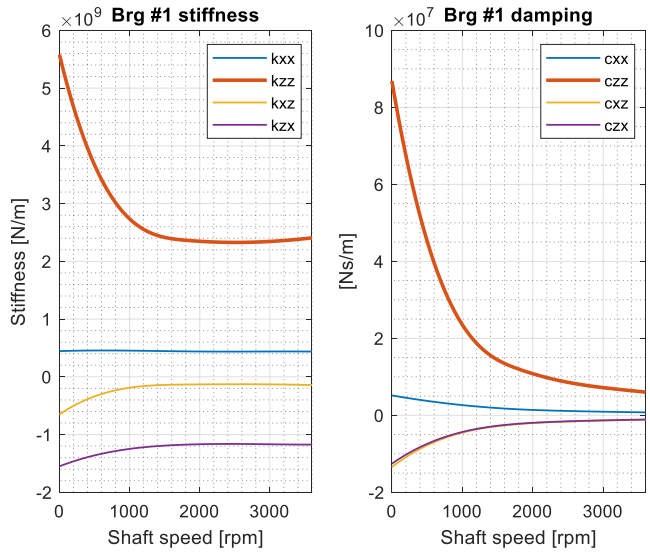

(a) (b)

Figure 8.1: (a) Stiffness and (b) Damping coefficients of the first journal bearing

8.1.2 Campbell diagram and mode shapes

It is important to note that eigenmodes appear in complex conjugate pairs. Additionally, some modes are heavily damped, with negligible imaginary components. As the shaft speed varies, certain mode shapes may vanish or undergo

significant changes, and the ordering of modes can shift. This can lead to substantial variations in the frequency content associated with a particular mode shape. This phenomenon is particularly pronounced in the presence of anisotropic bearing effects, gyroscopic coupling, or axial–radial interaction and is well known in rotor dynamics. To follow the evolution of the modes through the different shaft speed a mode tracking technique is commonly used. In this study, a tracking method based on the Modal Assurance Criterion (MAC) is employed.

Table 8.1 reports the first eleven damped natural frequencies and the corresponding non-dimensional damping factor *h*. Since the rotating speed of the machine 60 Hz, only natural frequencies up to 120 Hz are relevant for the analysis: higher frequencies are neglected because they do not participate to the system response. Generally, the higher the frequency is, the more the complexity of the mode shapes increases.

Mode number	**Shape**	**Direction**	**Damped frequency [Hz]**	**h factor**
1	Generator bending	Both directions, more horizontal	19.58	0.03
2	Turbine and compressor bending	Both directions, more horizontal	20.13	0.04
3	Generator bending	Vertical	26.21	0.05
4	Turbine and compressor bending	Vertical	30.86	0.06
5	Double-bending mode characterized by rigid-body coupling deflection	Both directions, mainly horizontal	38.07	0.13
6	Generator tilting	Both directions, mainly horizontal	44.61	0.16
7	Exciter deflection	Horizontal	76.72	0.27
8	Rigid-body coupling deflection, generator tilting and exciter deflection	Vertical	77.65	0.06
9	Double-bending mode characterized by rigid-body coupling deflection	Horizontal	84.99	0.08
10	Complex shape	Vertical	89.52	0.15
11	Complex shape	Horizontal	113.66	0.11

Table 8.1: Modes at 3600 rpm with damped natural frequency below 120 Hz

The following figures show some of these modes. The coloured green dot indicates the position of the thrust bearing. Very similar shapes can be observed in both

directions vertical and horizontal, thanks to the coupling between them introduced by the cross terms of the journals and in minor part from gyroscopic effect.

The first mode in *Figure 8.2* mainly affects the generator, as is evident from the response.

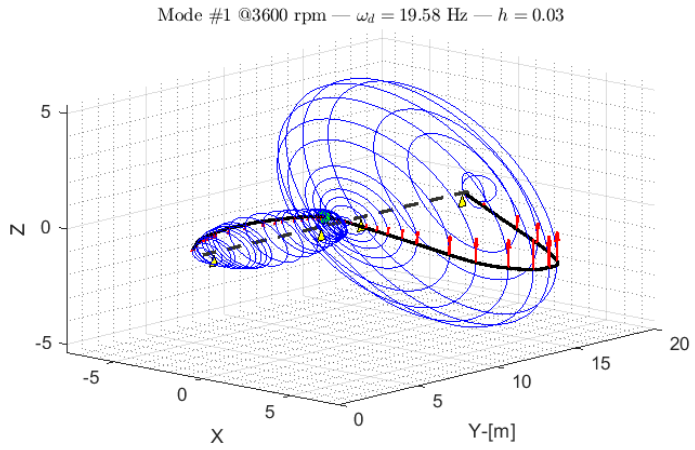

Figure 8.2: Mode shape #1

Also, the second mode in *Figure 8.3* is prevalently horizontal and is bending more the turbine and compressor part.

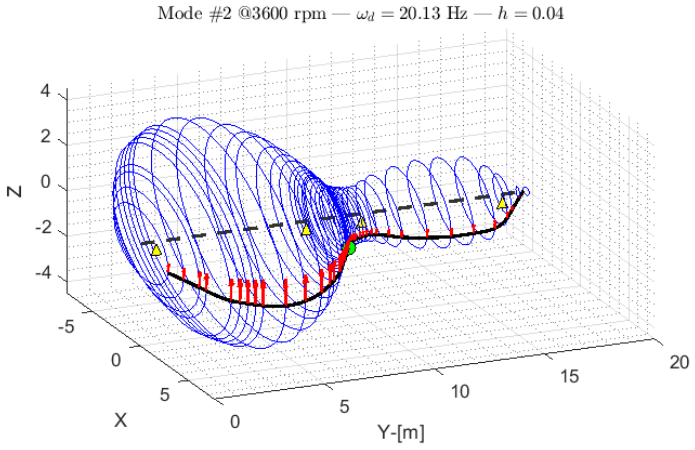

Figure 8.3: Mode shape #2

The fourth mode in *Figure 8.4* influences more the turbine and is mainly vertical.

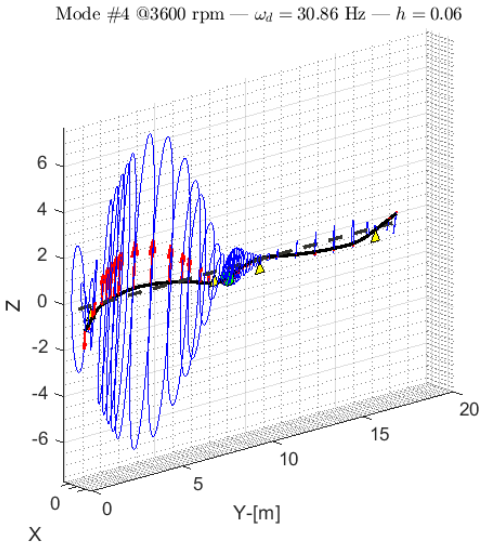

Figure 8.4: Mode shape #4

Mode 6 in *Figure 8.5* exhibit a nodal point (i.e., a point with no displacement), located between the span of the turbine journals and also between the span of the generator journals.

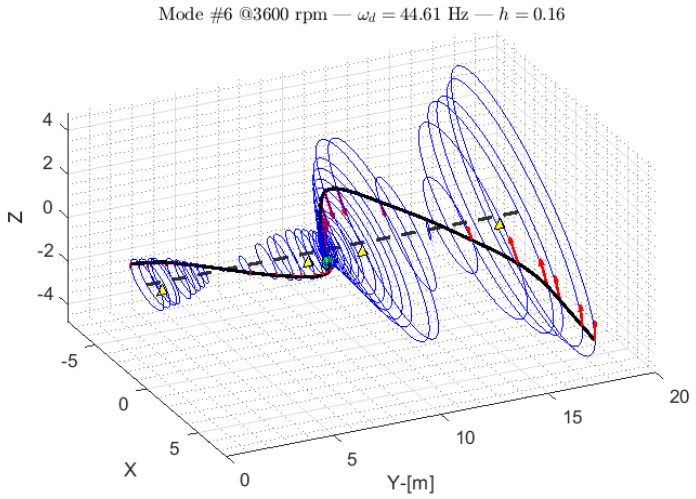

Figure 8.5: Mode shape #6

Mode 8 in *Figure 8.6* resembles a typical vibration mode of hinged beams, characterized by nodes at the locations of the bearings.

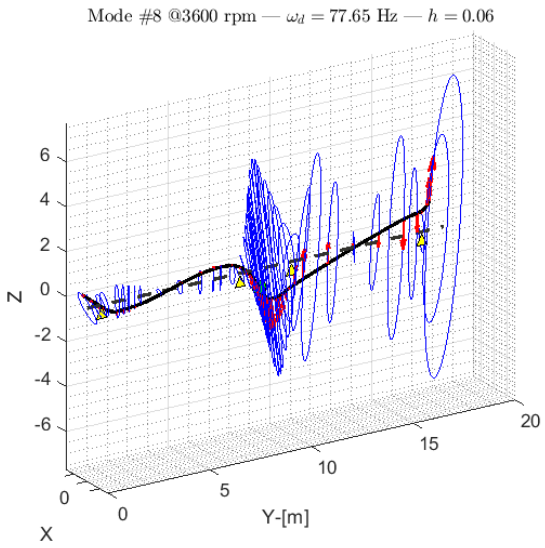

Figure 8.6: Mode shape #8

Mode 9 in *Figure 8.7* predominantly exhibits horizontal displacement, with two nodal points located within the spans of both the generator and the turbine. The shaft extremities show significant vibration amplitudes, which is typical of higher-frequency modes where the increased complexity of the mode shape results in more nodes. Notably, this mode causes considerable displacement at the flange located between bearings 2 and 3. The associated change in concavity at this location can be critical, as it may lead to fatigue-related issues over time. Therefore, it is important to avoid excessive excitation of this mode. The system exhibits high damping at this frequency, which effectively limits the dynamic response, making this mode noncritical under normal operating conditions.

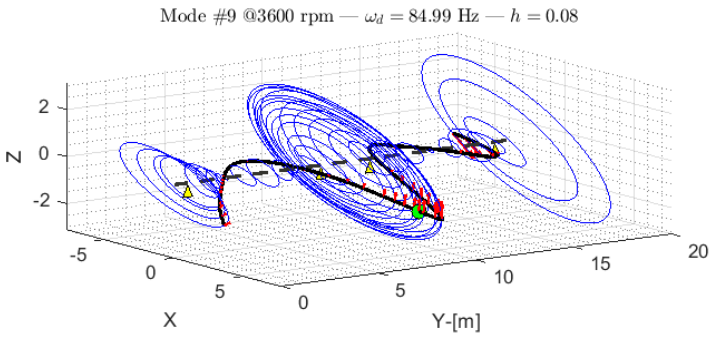

Figure 8.7: Mode shape #9

Mode 10 in *Figure 8.8* exhibits a relatively unusual vertical deformation pattern, which is consistent with the increased complexity of mode shapes at higher frequencies.

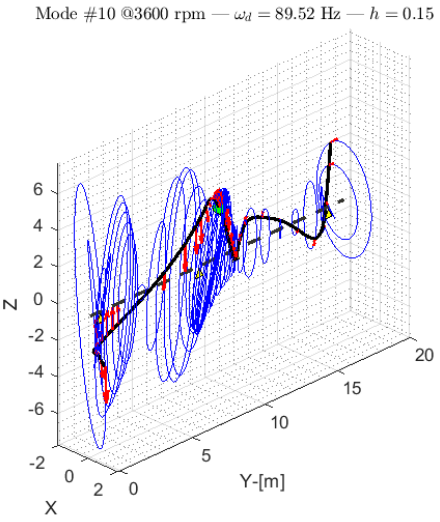

Figure 8.8: Mode shape #10

Figure 8.9 shows the first twelve modes as a function of the shaft speed. This diagram allows to evaluate critical speeds: the points where the response curves intersect the 1x excitation line, representing synchronous excitation. At these shaft speeds, the system operates under resonance conditions, thrust leading to possible amplified vibration amplitudes. Additionally, the diagram allows to classify modes as backward whirling or as forward whirling, according to their local slope negative or positive, respectively.

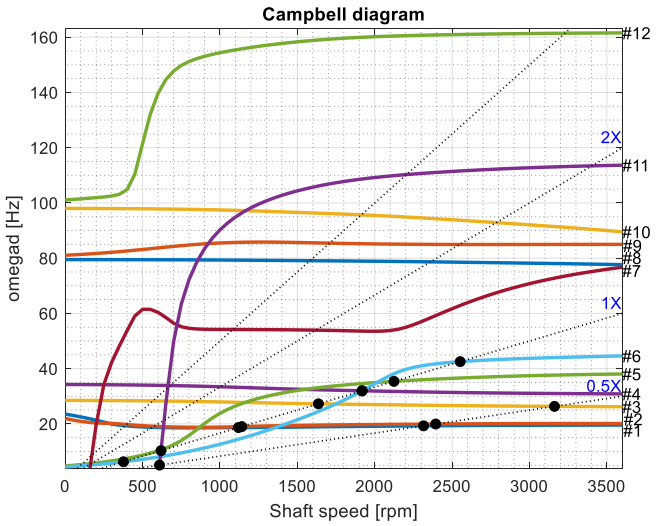

Figure 8.9: Campbell diagram reporting the first 12 modes

8.1.3 Unbalance response

The shaft unbalance considered in this analysis is 0.3 kgm at node 6, located near a turbine stage, and 0.2 kgm at node 37, within the generator. Both phases of the unbalances are supposed equal to 0. These regions are the most likely to introduce unbalance due to their significant mass and inertia. A visual representation of the unbalance locations is provided in *Figure 8.10*, where they are indicated by red dots.

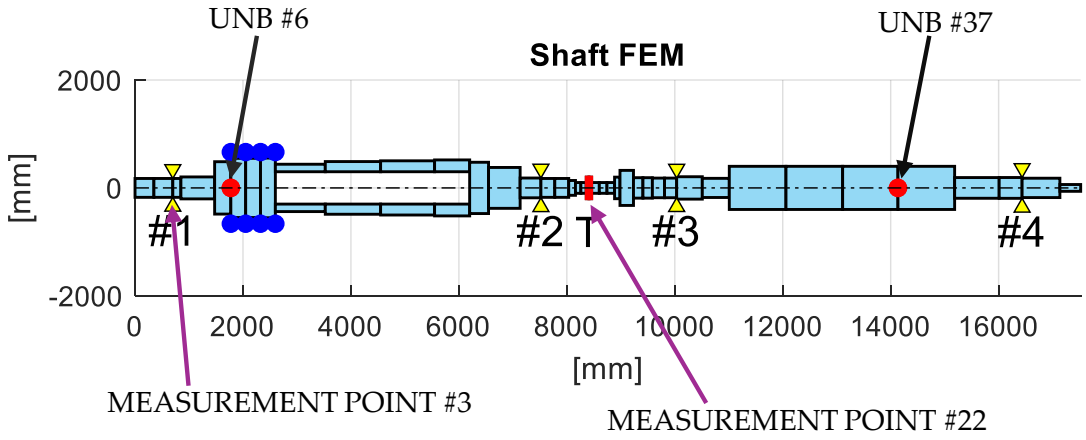

Figure 8.10: Unbalance point locations and measurement points

Figure 8.11 shows the system response for radial displacements x and z and tilting angles ϑ and ψ at the thrust node (node 22). It is evident that eigenfrequencies occur, for example regarding the z displacement, at 20.00 Hz, 26.67 Hz, 31.67 Hz and 41.67 Hz. It is important to note that the thrust node principally undergoes translation rather than rotation, like indicated by the relatively large displacement values and very low rotational values. This behaviour is also evident in the static sag analysis, where the thrust point is near a local maximum displacement position. It can be argued that in practical applications the thrust bearing is often positioned between the two journals, likely to reduce the coupling effects caused by the thrust itself.

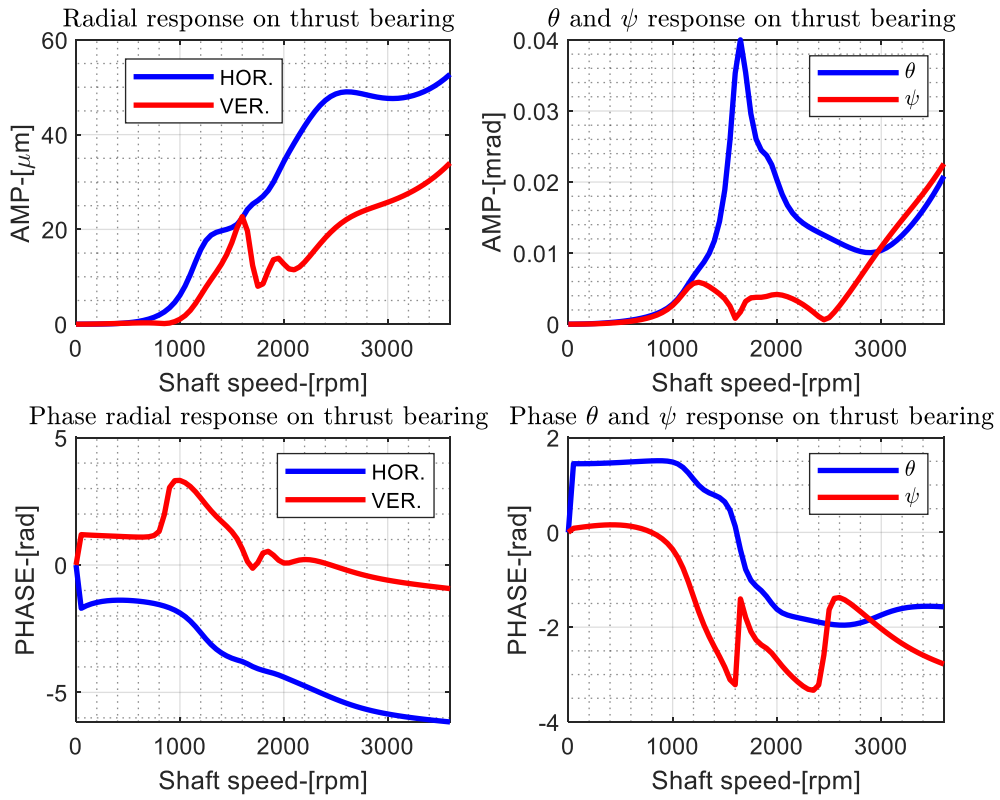

Figure 8.11: Response due to unbalance (amplitude and phase) at thrust bearing node for (a) radial displacements and (b) tilting angles

The same analysis is performed at first journal bearing (located at node 3), for radial displacements; results are shown in *Figure 8.12*. As previously noted, the shaft is stiffer in the vertical direction, which is reflected in lower displacements with respect to horizontal displacements. Peaks occur at approximately 1200 rpm, while the behaviour near 2500 rpm is less distinct due to significant damping. In vertical direction, there is a peak in correspondence of 1850 rpm. Analysis of the minima in the phase derivative of the response in vertical direction indicates eigenfrequencies at approximately 19.17 Hz, 33.33 Hz and 40.83 Hz.

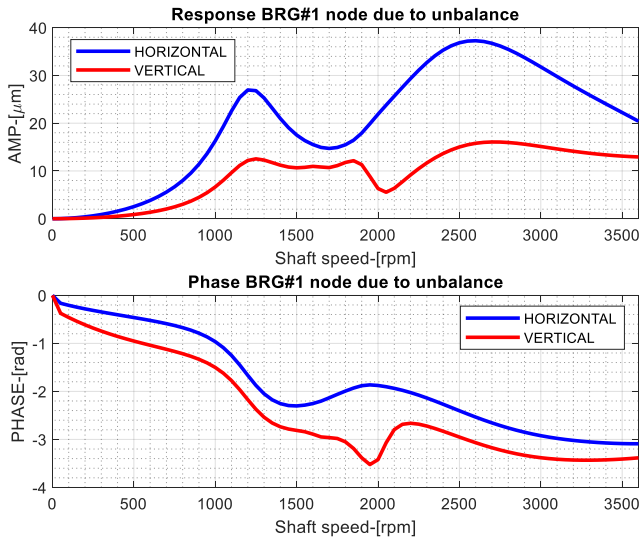

Figure 8.12: Displacement response due to unbalance (amplitude and phase) at first journal bearing

8.1.4 Shaft shape and orbits due to unbalance excitation

The unbalance response is plotted as a function of time. *Figure 8.13* shows a 3D representation of the orbits of each node caused by unbalance excitation. According to modal approach (see *Chapter 5.5.1*) the response is the sum of all the modes considered $\{\phi\}_j$, each one weighted by its modal coordinates q_j.

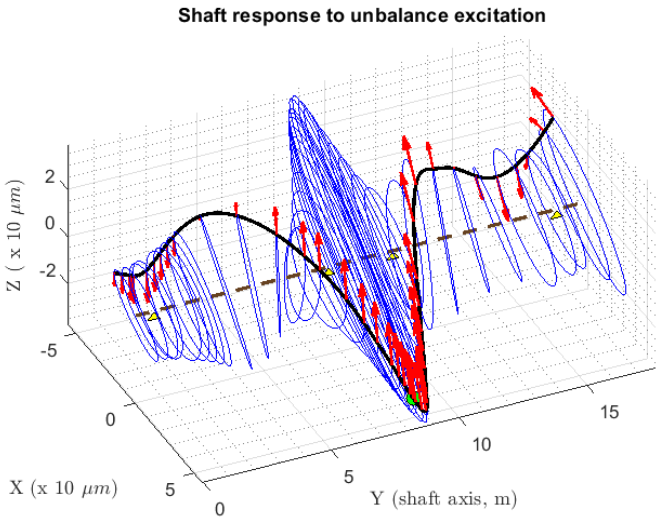

Figure 8.13: Shaft radial deformation caused by unbalance excitation

Some observations can be made. The maximum amplitude of displacement occurs in correspondence of the central part, reaching 50 μm horizontally. Horizontally, is worth noting that mode 5 and mode 9 exhibit a seagull-shaped deformation. However, they are relatively well damped. Their contribution may nonetheless be amplified when excited because one mode activation can force the other and vice versa. Understanding the contribution of other mode shapes is quite challenging because they also significantly influence the response, also given that their frequencies are close to each other.

8.2 Thrust bearing activated

8.2.1 Static deflection and bearing reaction forces

As previously discussed, the thrust bearing also has a limited influence on the radial response. This effect may become more pronounced by increasing the runner diameter or reducing the clearance, leading to a more coupled and more linear system behaviour. In this model, analyses of the linearized responses around several static equilibrium positions are carried out. The method used to determine the static equilibrium is explained in *Chapter 5.4*. The overall static deflection at different static axial loads is illustrated in *Figure 8.14.*

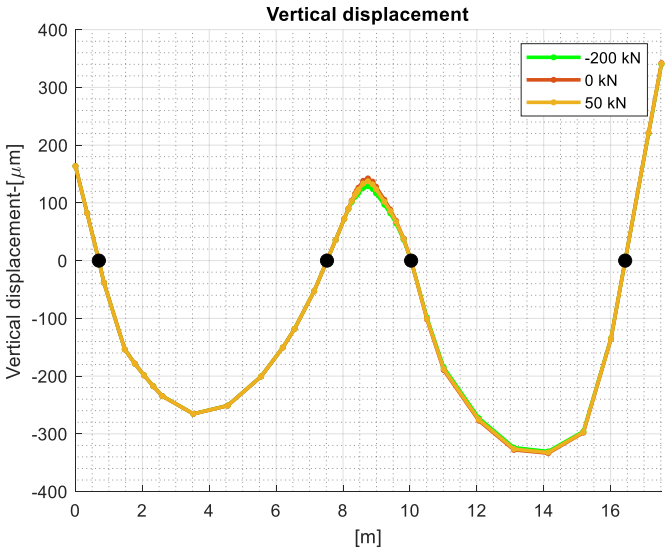

Figure 8.14: Static deflection at -200 kN, 0 kN and 50 kN

The influence on the vertical displacement is evident only between the second and the third journal bearings. A zoom is provided in *Figure 8.15*.

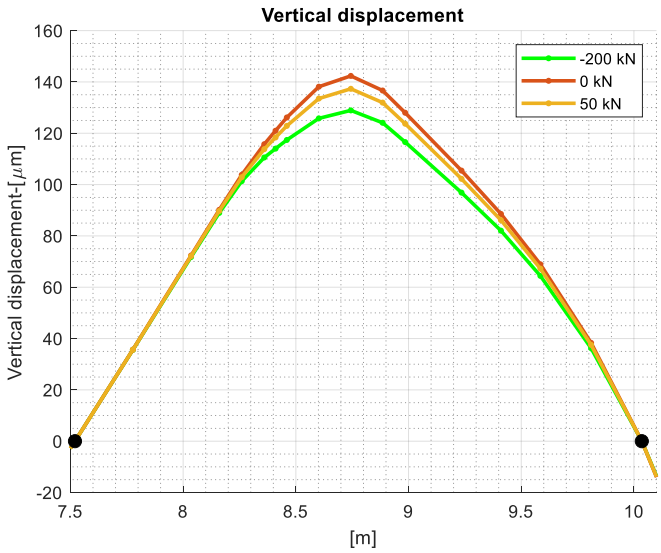

Figure 8.15: Zoom of the vertical displacement due to gravity at -200 kN, 0 kN and 50 kN

As evident from these diagrams, when the thrust rotational stiffness reaches its minimum at a load of -15.8 kN, there is a maximum vertical displacement observed. This occurs because, as the axial load changes significantly, the moment applied to the thrust bearing tends to align the runner in vertical direction, making straighter the shaft. Without this effect, the angular displacement would be greater due to the upward deflection of the span between the bearings under the influence of gravity. In the case where no axial degrees of freedom are considered and no thrust bearing is present, the rotation ϑ should be $1.06 \cdot 10^{-4}$ rad. The trend with the thrust activated is shown in *Figure 8.16a*. In *Figure 8.16b* the moment M_x is illustrated as a function of the axial load.

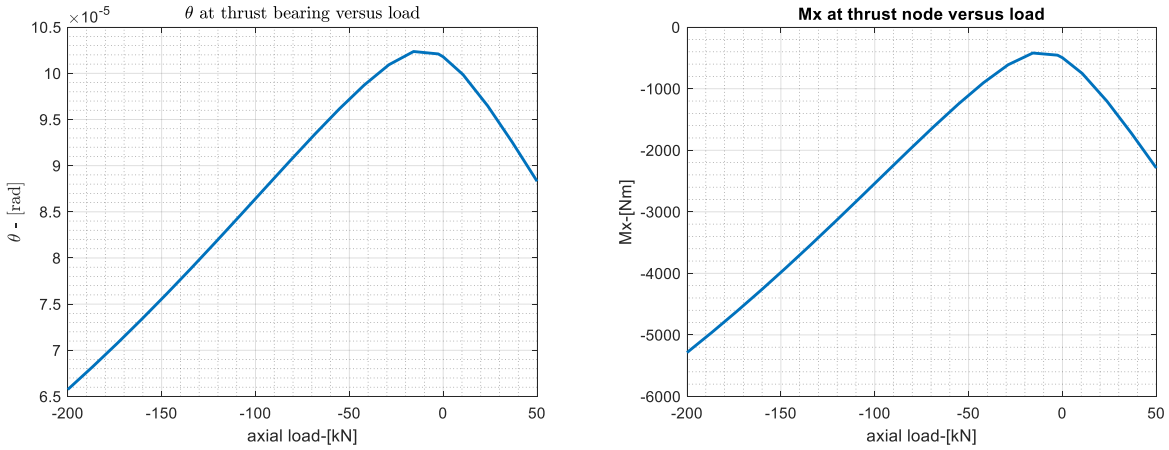

(a) (b)

Figure 8.16: (a) Tilting angle due to weight at the thrust node as a function of axial load; (b) Moment M_x due to weight as a function of axial load

Figure 8.17 shows the S-shape axial displacement trend resulting from the external load. It can be noticed that this working range is largely less than the axial semiclearance, of 175 μm, with the range spanning from −103 μm to 124 μm. Furthermore, it is clear the nonlinearity of the axial stiffness of the bearing.

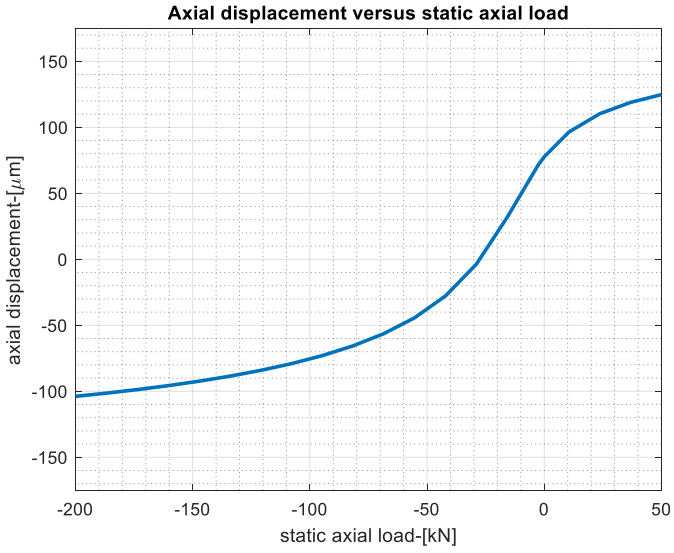

Figure 8.17: Axial displacement as a function of load

Due to the application of these moments, also the reactions on journals should vary. However, the effect is very poor and is mainly appreciable in the second and third bearing, as reported in *Figure 8.18*.

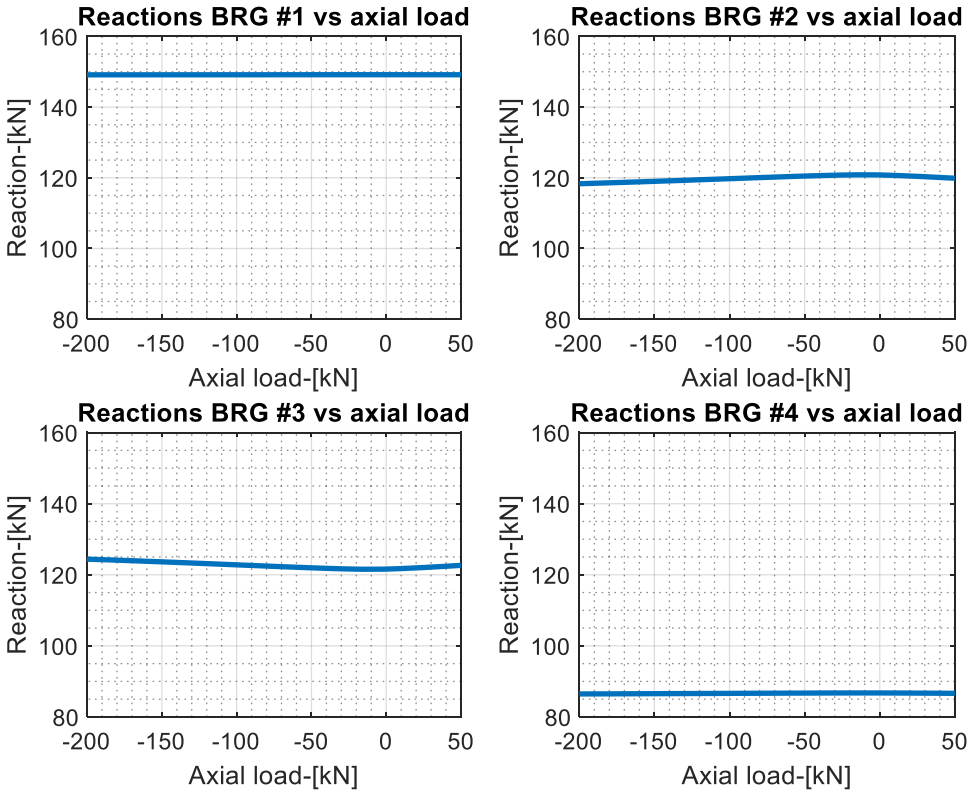

Figure 8.18: Reaction forces at journal bearings as a function of axial load

The percentage variation with respect to thrust free case is summarized in the following *Table 8.2*.

BRG 1	BRG 2	BRG 3	BRG 4
-0.03%	-2.30%	2.55%	-0.36%

Table 8.2: Percentage variation of reaction forces of journal bearings between no-thrust and thrust cases

Figure 8.19 shows the stiffness and damping coefficients of the second journal bearing as a function of axial load. The most significant variations in the dynamic bearing coefficients are instead observed in the direct zz terms. In the second bearing, k_{zz} decreases about 4%, whereas c_{zz} decreases about 2% as the axial load changes from -15 kN to -200 kN. In bearing 3, the k_{zz} increases about 4%, whereas c_{zz} increases about 2.3% with the same load change. These variations are negligible and the integration model can be disregarded.

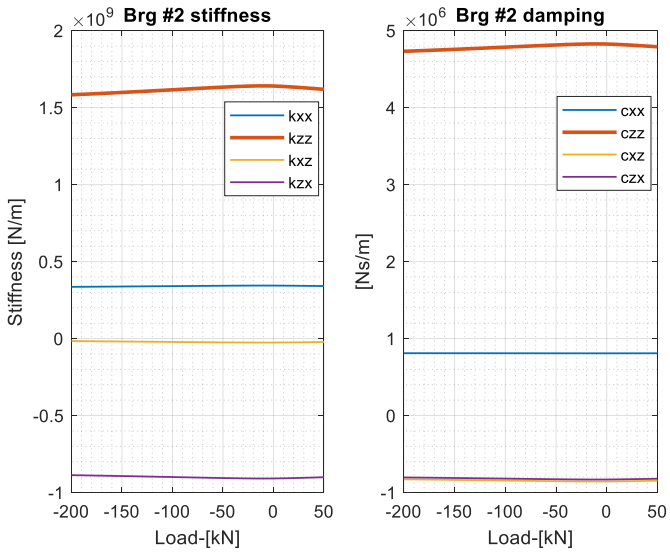

Figure 8.19: (a) Stiffness and (b) Damping coefficients of the second journal bearing as a function of axial load

In contrast, variations of linearized thrust bearing coefficients are significant changing static axial load. The following figures show damping and stiffness coefficients as a function of applied axial load, separately for extra-diagonal and diagonal terms. In *Figure 8.20* and *Figure 8.21* represent the direct damping and stiffness coefficients as a function of the externally applied static axial load.

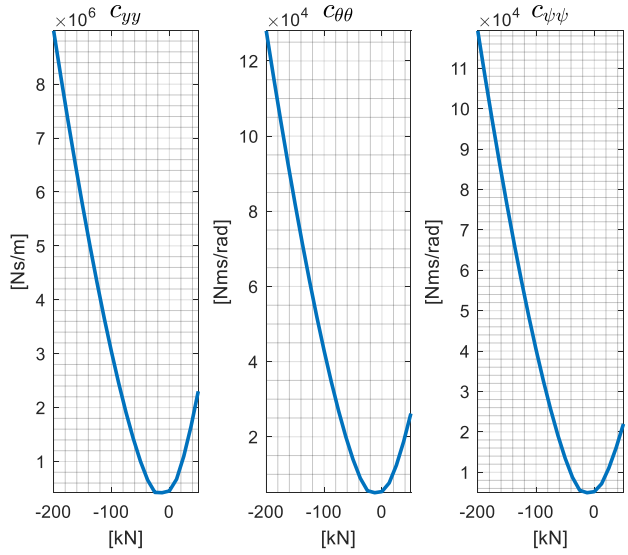

Figure 8.20: Direct damping terms as a function of the axial load

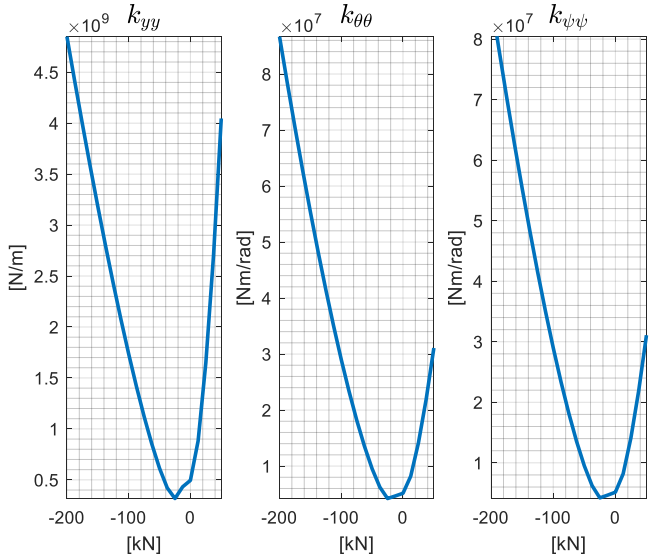

Figure 8.21: Direct stiffness terms as a function of the axial load

The direct terms increase toward both sides, with a function exhibiting positive concavity. It is worth to note that close to null axial load, stiffness and damping are very low. This results in a low damped natural frequency at low frequency when axial load is close to zero. The cross terms change sign, as they represent derivatives of the underlying functions. Given the complexity of the functions, these trends are expected and justifiable. For a more detailed investigation of some of these trends, the reader may refer to *Chapter 4*. Therefore, it is not appropriate to treat these coefficients as constant values based solely on the initial position, since they vary along the clearance. As an example, *Figure 8.22* illustrates the variation of the damping cross terms. Although cross stiffness terms are not shown, they follow similar trends.

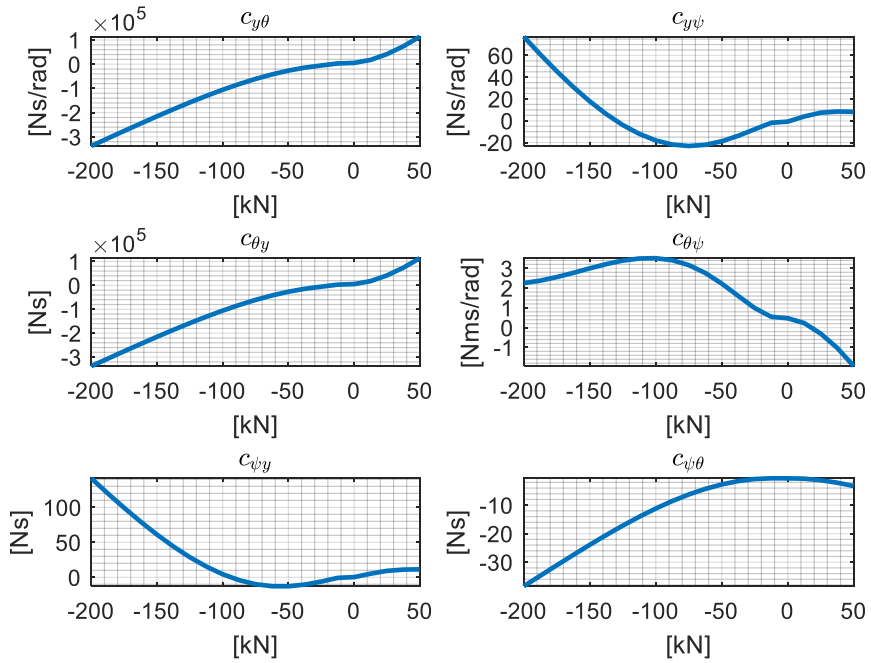

Figure 8.22: Cross-term damping coefficients as a function of axial load

8.2.2 Sensitivity map

About the sensitivity map (similar to a Campbell diagram), mode tracking is carried out in both forward and backward directions, depending on the system operating load conditions. A discretization of the possible static axial loads is performed and corresponding modes are identified across the different load cases. *Figure 8.23* is the frequency-load sensitivity map of the eigenfrequencies as a function of the static thrust load. Clearly, a greater effect is seen when the direct side is loaded. Mode 6, identified by the sky-blue colour, is the axial mode and exhibits the most significant change.

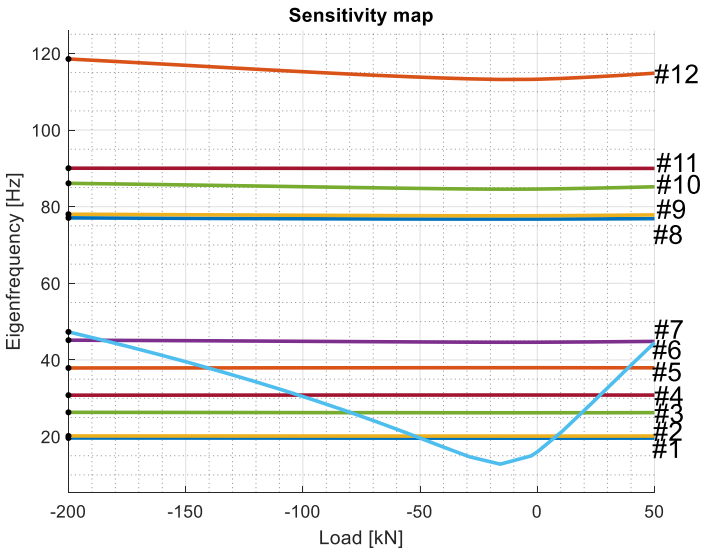

Figure 8.23: Sensitivity map of the first 12 eigenfrequencies with respect to axial load

For each mode considered (first eleven modes), four different cases are analysed:

1. Variation of the eigenfrequency at -200 kN with respect to no-thrust case
2. Variation of the eigenfrequency at -200 kN with respect no-loaded thrust
3. Variation of the non-dimensional damping factor at -200 kN with respect to no-thrust case
4. Variation of the non-dimensional damping factor at -200 kN with respect to no-loaded thrust.

The following synoptic *Table 8.3* compares the above-mentioned cases analysed.

Modes	Case 1)	Case 2)	Case 3)	Case 4)
1	0.29 %	0.27 %	-2.02 %	-1.36 %
2	0.18 %	0.19 %	-1.06 %	1.36 %
3	0.46 %	0.41 %	2.00 %	1.60 %
4	-0.16 %	-0.12 %	6.05 %	1.02 %
5	-0.42 %	-0.18 %	-3.58 %	0.92 %
6	1.22 %	1.19 %	0.43 %	0.43 %
7	0.46 %	0.40 %	1.24 %	1.27 %
8	0.50 %	0.51 %	21.28 %	18.87 %
9	1.31 %	1.78 %	21.76 %	18.15 %
10	0.58 %	0.08 %	2.05 %	1.92 %
11	4.23 %	4.67 %	13.36 %	16.04 %

Table 8.3: Percentage variation of first 11 eigenfrequencies and corresponding non-dimensional damping factors between different analysed cases

It is quite evident that modes 6, 9, and 11 exhibit more than a 1% change in their frequency content. This variation is clearly reflected in the corresponding mode shapes. Specifically, when no thrust bearing is mounted, the rotation angles in both directions are significant. Their combined effect results in a large overall rotational amplitude at that node. The bearing introduces high restoring moments that stiffen the system: as a consequence, the associated natural frequencies increase.

Regarding damping, the situation is more complex. It is possible that the angular velocities associated with these modes are relatively high, roughly estimated as the product of the rotation angles from the normalized mode shapes times their frequency content. As a result, under higher loads, the great angular motion may lead to stronger squeezing effects, which in turn produce higher damping.

The axial eigenfrequencies occurrence is strongly affected by the load applied on the thrust bearing, as shown in *Figure 8.24*.

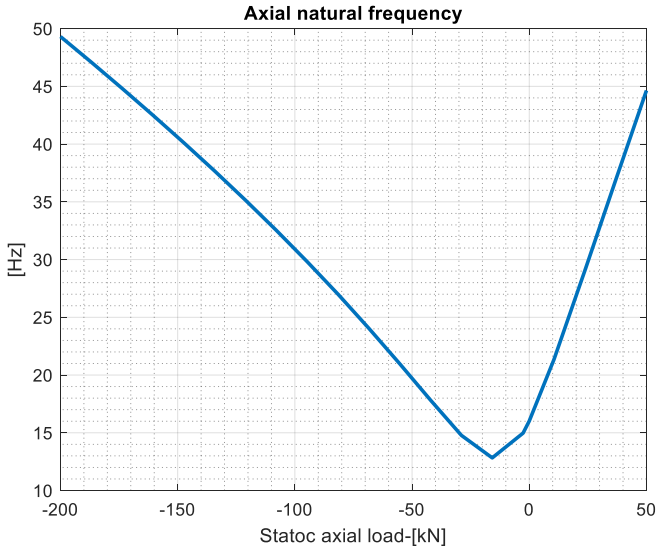

Figure 8.24: Axial natural frequency as a function of axial load

In *Figure 8.25* two Frequency Response Functions (FRF) are compared in two different cases: when no axial load is applied and when the axial load is set to −200 kN.

When no axial load is applied, the bearing exhibits low damping and reduced stiffness in the axial direction. This results in large axial vibrations, highlighting the system sensitivity under unloaded conditions. The order of magnitude of the difference in dynamic behaviour becomes even more evident when the response under a high axial load (−200 kN) is considered: there is a difference of two order of magnitude in the axial response amplitude compared to the unloaded condition.

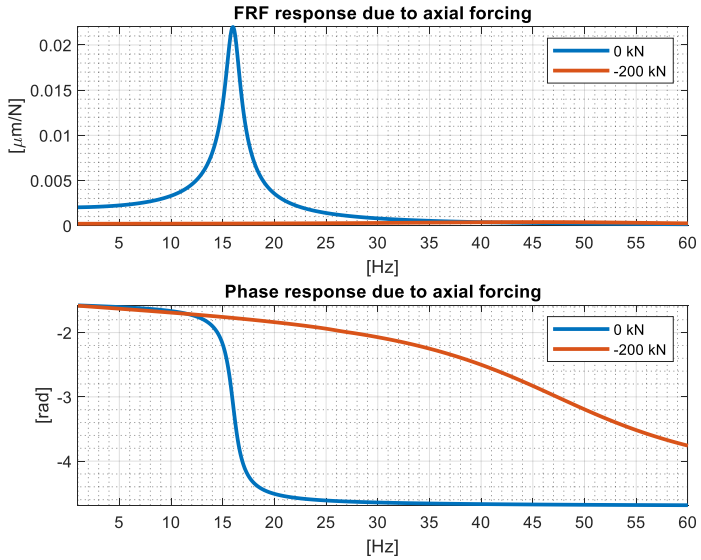

Figure 8.25: Axial FRF of the system for 0 kN axial load and −200 kN axial load

Applying an axial harmonic force to the shaft results in minimal rotations. The coupling appears to be higher in zones where damping is lower, near 0 load. This allows to locally vibrate more axially and thus making the shaft felling more torsional effects when moving. The maximum rotational effect is observed at the thrust node in *Figure 8.26*, as rotations at other points are constrained by the shaft stiffness. It is concluded that the rotations induced by pure axial forcing are approximately one order of magnitude smaller than those caused by unbalance (on the order of 10^{-5} rad), assuming a dynamic load amplitude of 1000 N. In this sense, it can be said that the radial effect of axial forcing is roughly one-tenth the effect produced by unbalance.

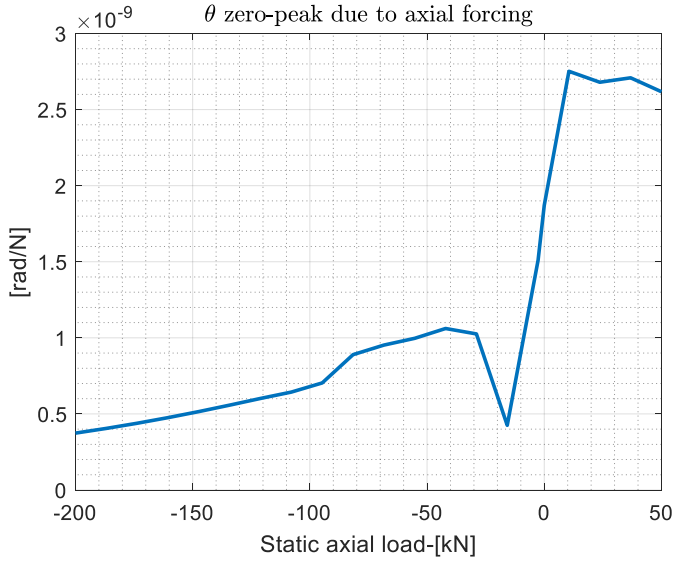

Figure 8.26: Angle ϑ of the thrust node as a function of axial load

8.2.3 Stability map

The stability map, reported in n *Figure 8.27*, is performed by varying the static axial load. Results indicate that the operating condition with zero static axial load (marked with the blue circle) lies very close to the y-axis, which suggests proximity to the stability threshold. This implies a higher risk of instability: any destabilizing influence coming, for instance, from aerodynamic effect could highly excite the system response. Under such conditions, the shaft is susceptible to vibrating at its axial natural frequency, which is approximately 16 Hz, indicating axial resonance.

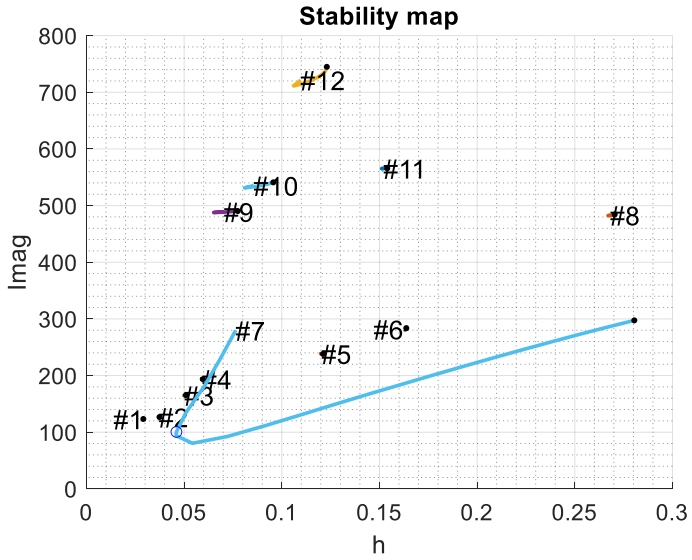

Figure 8.27: Stability map for the first 12 modes, varying static load

8.2.4 Unbalance response

Axial system response to the radial unbalance as a function of axial load in terms of amplitude and phase is reported in *Figure 8.28*. Since the amplitude of vibration is less than µm ,under the current assumptions and configuration, the unbalance alone is not sufficient to significantly excite the axial degree of freedom. A very small contribution appears only under high load conditions, where any rotational motion results in increased instantaneous axial forces. It is worth remembering that such displacements are so small that they cannot be practically measured and are visible here only thanks to numerical simulation.

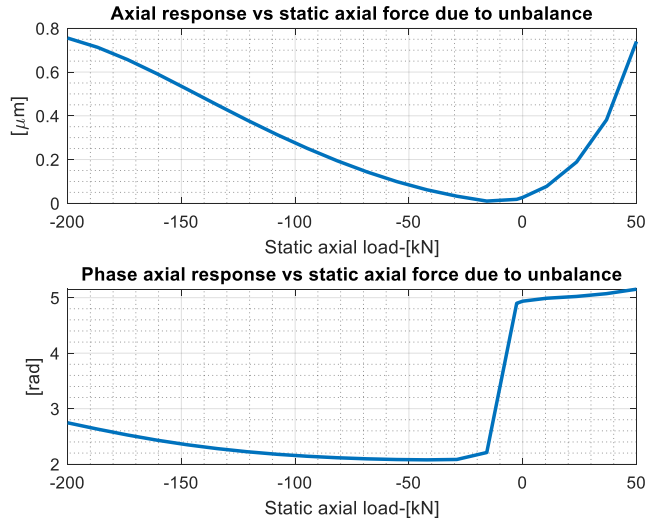

Figure 8.28: Amplitude and phase of unbalance response as a function of axial load

System response for radial displacements and tilting angles at the thrust bearing node is reported in *Figure 8.29*. The x displacement at the thrust point decreases by about 5% when the force changes from -15 kN to -200 kN, going from 55 μm to 52 μm. The z displacement decreases from 35 μm to 33 μm, which is approximately a 6% reduction. The rotation ϑ, however, decreases much more significantly, by about 43%, from 2×10^{-5} rad to 1.1×10−5 rad. The angle ϑ of the thrust is maximum for low load values. The rotation ψ shows a similar trend.

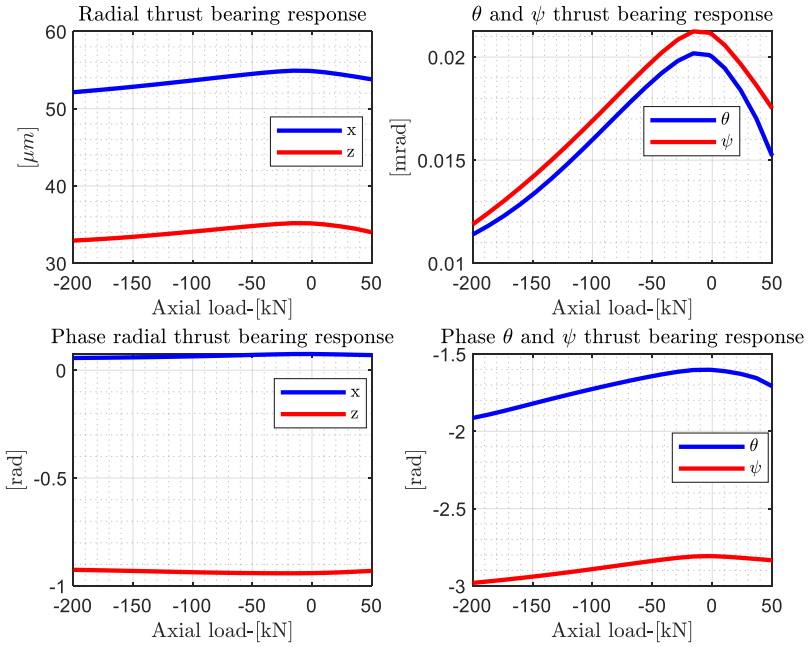

(a) (b)

Figure 8.29: Response due to unbalance (amplitude and phase) as a function of axial load, at thrust bearing node for (a) displacement and (b) tilting angle

8.2.5 Mode shapes

In this paragraph, the vertical and horizontal displacements are normalized separately using the maximum value between the displacement in the respective direction and the axial displacement. This approach yields the correct shapes in each direction, but loses the amplitude difference between directions, since the maximum value is always set to one. The objective of this analysis is to assess the thrust bearing's ability to alter the shape of the vibration modes.

A slight coupling effect can be observed from the visualization of seventh mode shape, in *Figure 8.30*: since this mode is normalized using both radial and axial displacements, the vertical bar indicates that the axial component dominates in terms

of amplitude. However, a purely axial mode would correspond to a straight shaft in both the vertical and horizontal directions. In contrast, the observed bending in the central part of the shaft, particularly in the vertical direction, indicates that radial vibration is also present in this mode.

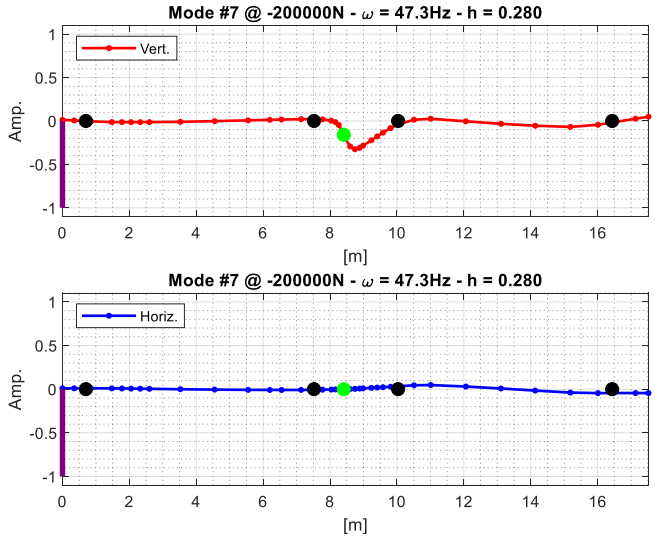

Figure 8.30: Mode shape #7, setting axial load at −200 kN

The first eigenfrequencies analysed below 120 Hz are reported in the following *Table 8.4*. Axial load is set at −200 kN.

Mode	Damped frequency (Hz)	h factor
1	19.64	0.03
2	20.17	0.04
3	26.33	0.05
4	30.81	0.06
5	37.91	0.12
6	45.16	0.16
7	47.33	0.28
8	77.08	0.27
9	78.04	0.08
10	86.10	0.10
11	90.04	0.15
12	118.55	0.12

Table 8.4: first 12 eigenfrequencies and corresponding non-dimensional damping factors when the thrust is activated

It is quite evident that the variation with respect to the thrust bearing free case is very little and the thrust is not able to change significantly the eigenfrequencies with its torsional stiffness.

As previously mentioned, the thrust locally increases the shaft stiffness, leading to a reduction in local rotation. This phenomenon becomes particularly clear when examining specific modes. A couple of mode shapes, as examples, are presented and compared in the following figures.

In *Figure 8.31a* the eight mode shape in the thrust bearing free case is reported. *Figure 8.31b* shows the same mode when an axial load of -200 kN is applied on the thrust bearing. The effect is so pronounced that it slightly alters the overall mode shape, also resulting in a frequency shift of 1 Hz. This amplified response is due to the large rotational values present in the thrust-free case, in both directions. *Figure 8.31c* shows eight mode shape when an axial load of 50 kN is applied on the thrust bearing. The influence is not so evident, but also there the shaft is a little bit risen up in the middle. This is reflected in the small frequency shift of 0.2 Hz.

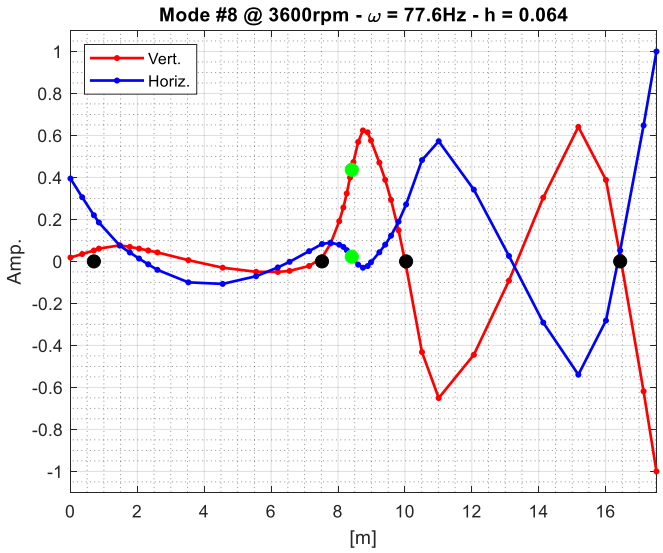

(a)

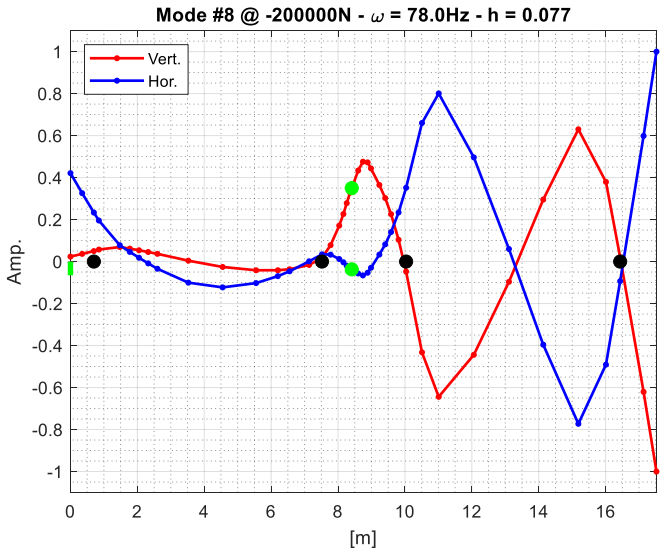

(b)

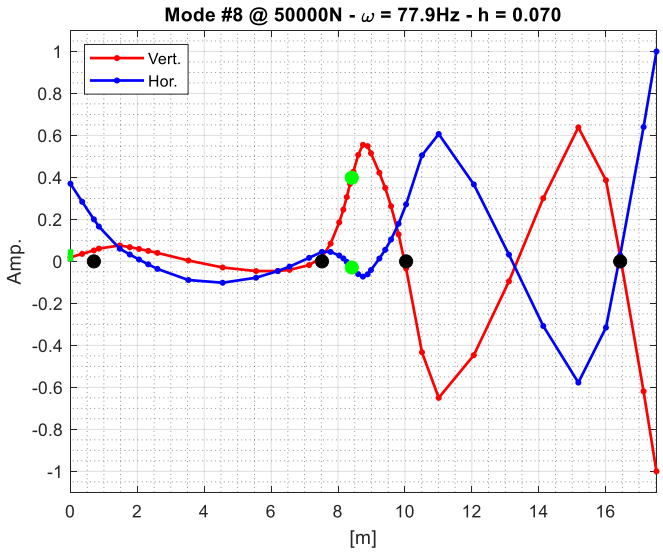

(c)

Figure 8.31: Mode #8: (a) Thrust bearing free case; (b) -200 kN static axial load; (c) 50 kN static axial load

Figure 8.32a shows ninth mode when the thrust bearing is disactivated. Comparing this plot to ninth mode shape when an axial load of −200 kN is applied in *Figure 8.32b*, the same phenomenon observed for mode eighth becomes more evident. The slope near the thrust region significantly reduced and the frequency risen up about 5 Hz. Moreover, this influence causes the section to the left of bearing 2 to rise and shifts the position of the local minimum to the left. The very same situation can be

observed in the case of 50 kN axial load in *Figure 8.32c,* but with higher angles and less frequency content change (1 Hz).

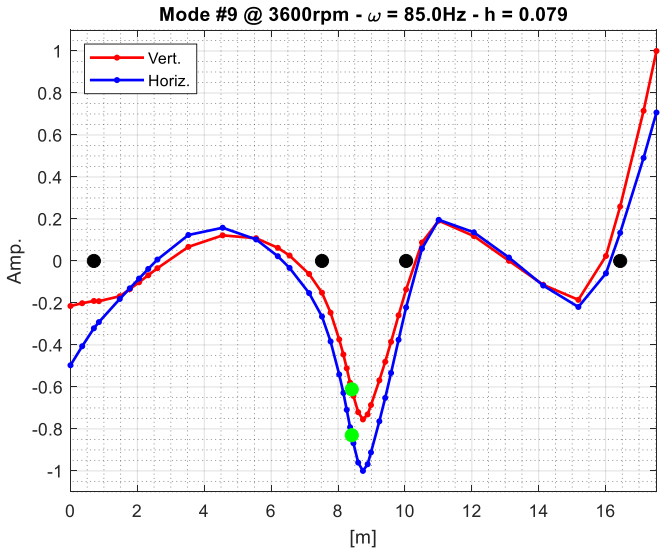

(a)

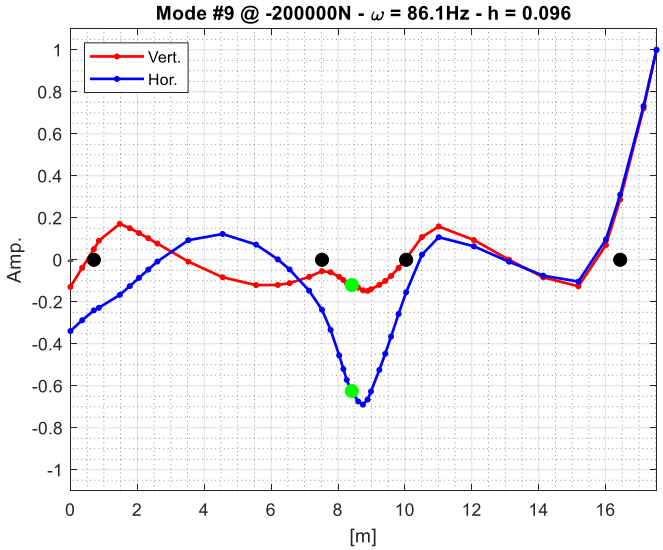

(b)

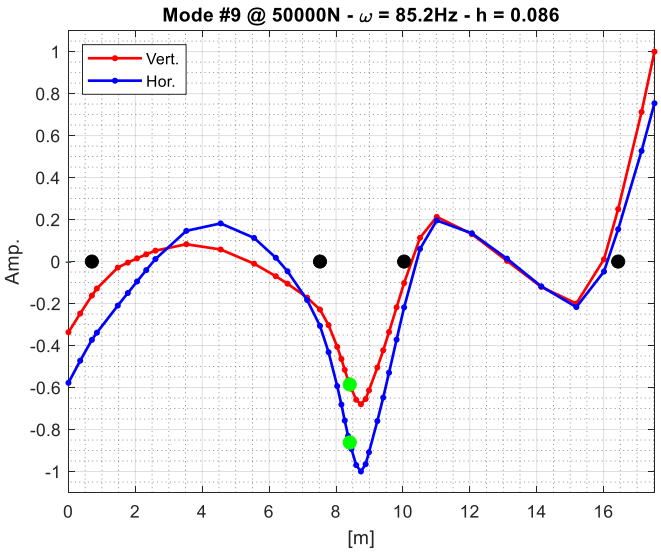

(c)

Figure 8.32: Mode #9: (a) Thrust bearing free case; (b) -200 kN static axial load; (c) 50 kN static axial load

It can be concluded that the effect becomes significant when the mode exhibits substantial rotation in the thrust node, and the associated moments are high. This condition typically occurs under high load scenarios.

8.2.6 Change in thrust bearing position

The thrust has been relocated to node 18, where the rotation reaches its maximum value between the two bearings, $1.42 \cdot 10^{-4}$ rad, in the thrust-free case. New position is shown in *Figure 8.33*, marked in purple colour. This position is also reasonable, since it is close to the actual thrust location (node 22), and the shaft diameter is the same. The purpose for this is investigated for a possible higher coupling. The same analyses of the previous case are presented in the following about this new configuration.

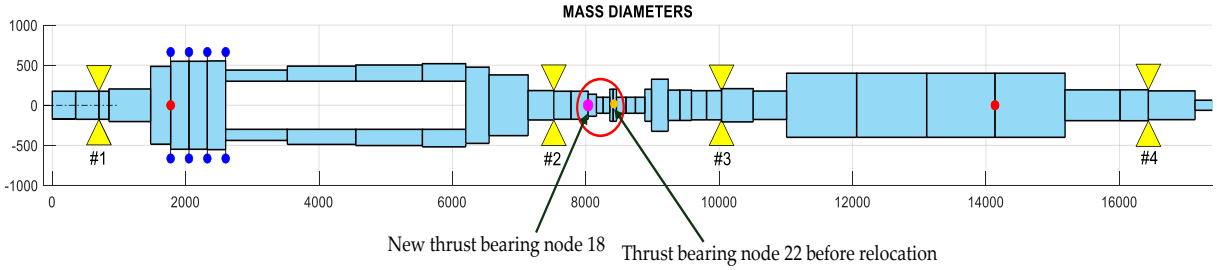

Figure 8.33: Relocation of thrust bearing: new position marked in purple colour

Figure 8.34 shows the moment M_x as a function of axial load, generated by the lubricant inside the thrust bearing because of static deflection. It can be appreciated that the moment is always bigger in magnitude with respect to the case in which the collar is located at node 22.

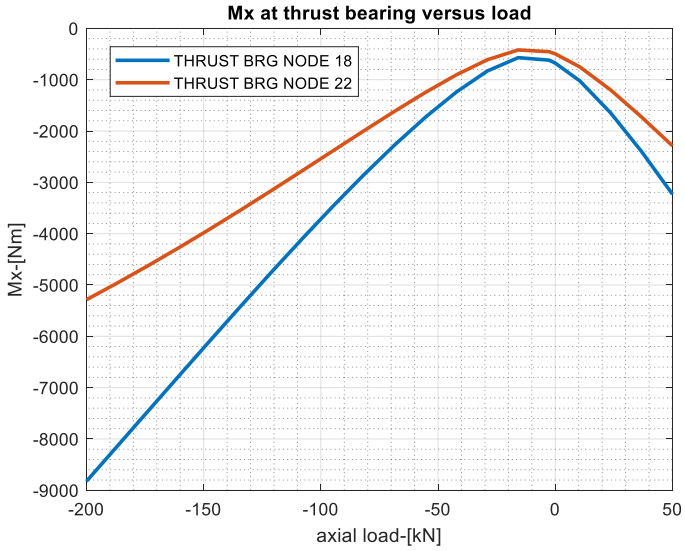

Figure 8.34: Moment M_x due to weight as a function of axial load

The axial response due to unbalance is greater than the previous case, as shown in *Figure 8.35*.

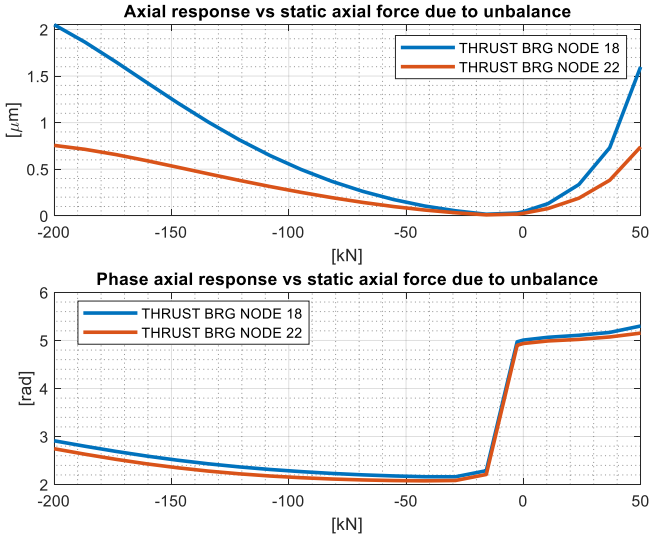

Figure 8.35: amplitude and phase of unbalance response as a function of axial load, thrust node 18

The increased static rotation, summed to the dynamic one caused by the unbalance, are increasing the rotation observed at node 18, resulting in a pronounced effect on the radial-axial coupling.

The effect on natural frequency is not much changed and not reported.

9 Time integration results

In this chapter, the results of time integration simulations are presented. A general investigation is carried out to evaluate the effectiveness and reliability of the nonlinear model, by imposing different excitations, axial or radial or combined axial and radial. Nonlinear forces of the thrust bearing due to oil film are computed following the approaches described in *Chapter 7*: Artificial Neural Network and Interpolator; results are then compared with the results from the linear model, which instead works in the complex domain. The time integration with the thrust bearing oil film forces given by Reynolds equation will be addressed in *Chapter 9.3.*

9.1 Radial dynamics only

A preliminary analysis is performed in order to validate the results of the time integration. This analysis neglects the axial degree of freedom and thrust bearing forces, focusing solely on the radial dynamics. In particular, two types of excitation are simulated:

1. Unbalance forcing, applied to visualize the system response and validate the linear model.
2. Radial disturbance noise, introduced at selected nodes to excite specific frequency ranges.

All the simulations performed are conducted using MATLAB Ode45 solver, with maximum step size of 1×10^{-4}, absolute tolerance of 1×10^{-20} and relative tolerance of 1×10^{-14}. The sampling frequency is 2000 Hz.

9.1.1 Unbalance response

In this case, the shaft residual unbalances are 0.3 kgm in node 6 and 0.2 kgm in node 37, both with 0 phase, like shown in *Figure 8.10.*

The orbits at journal bearings obtained from the steady-state complex response of the linear model are also reproduced in the time-domain simulations of the same model,

confirming the consistency between the two approaches and supporting the validation of the numerical integrators. In the case of pure unbalance excitation, the radial response transient can be considered negligible after 1.5 seconds, thanks to the system's damping, as also shown in *Figure 9.1*.

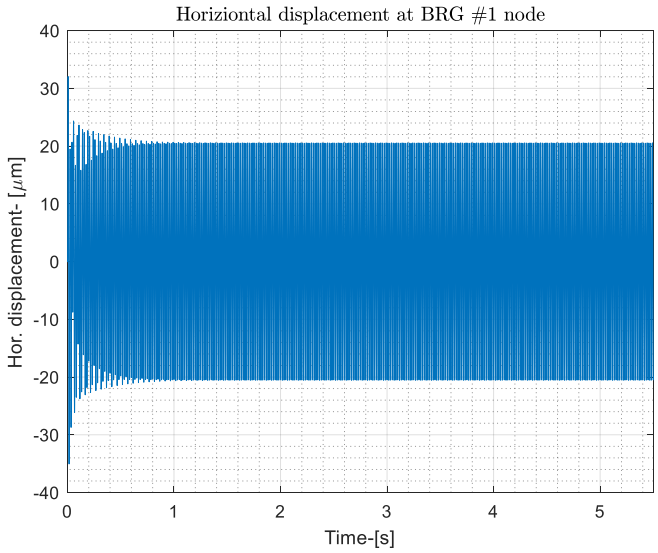

Figure 9.1: Example of time integration result: horizontal displacement at bearing #1

The results suggest that the only displacement amplitude not represented so much properly is the one of the bearings in correspondence of the exciter. However, the exciter is far from the thrust bearing and has a minimal influence on it. *Table 9.1* provides a summary of the results of this comparison.

Disp amp.	**From time integration [μm]**	**Steady state [μm]**	**Abs err [μm]**	**Perc. Err [%]**
BRG 1X	20.55	20.42	0.13	0.64
BRG 1Z	13.16	12.93	0.23	1.78
BRG 2X	30.48	30.42	0.06	0.20
BRG 2Z	21.01	20.56	0.45	2.19
BRG 3X	24.23	23.97	0.26	1.08
BRG 3Z	16.78	16.45	0.33	2.01
BRG 4 X	24.53	24.28	0.25	1.03
BRG 4 Z	13.36	15.64	2.28	14.58

Table 9.1: Comparison between journal orbit displacements from time integration and steady state

9.1.2 Radial noise

The aim of this analysis is to evaluate the response at a specific point in the structure. If this point significantly contributes to a certain mode shape, then exciting the system at the corresponding modal frequency will transfer a substantial amount of energy into that mode. As a result, the system transfer function can be computed for all degrees of freedom over the entire time history, enabling the detection of natural frequencies at that location. The FRF is numerically evaluated. At each frequency, the FRF phases correspond to the difference between the phases of the response and those of the input signal, whereas the amplitudes are obtained by dividing the response spectrum by the excitation spectrum.

Natural frequencies are particularly evident when the excitation effectively excites a specific mode and the response is measured at a point that is not a node of that mode shape, since nodes, by definition, have zero displacement and thus produce minimal or no response. The noise excitation can be applied to any vertical or horizontal degree of freedom.

The FRF are computed over the same frequency range as the applied noise, and the response amplitudes are normalized by the excitation amplitude to obtain unit response amplitude. For phase analysis, the *unwrap* function is used to ensure phase continuity.

Phase information is especially useful, as it can reveal resonance conditions even when peaks in amplitude are not evident, for example, when the system exhibits a nodal point or the mode is highly damped. In such cases, the derivative of the phase curve can be a valuable indicator, as a local maximum typically signals the presence of a resonance.

The time history and its spectrum of the band-limited (5-120 Hz) white noise used to force radially the system is shown in *Figure 9.2.*

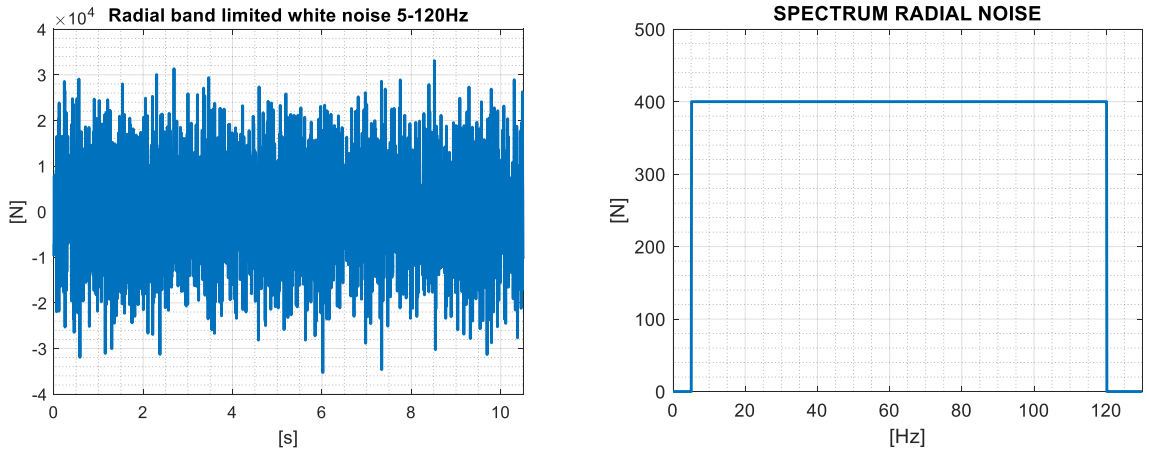

(a) (b)

Figure 9.2: (a) Time history of radial noise, (b) spectrum of radial noise, defined between 5 and 120 Hz

Assuming the shaft to be perfectly balanced, two different excitation configurations are analysed:

- Radial noise applied at the thrust bearing node in horizontal direction.
- Radial noise applied immediately to the right of the unbalance, within the generator.

The integration time for both analyses is set to 11.5 seconds to ensure sufficient excitation of all relevant frequencies within the noise. The noise input begins at 1 second to minimize interference with the initial transient response. Spectral evaluations are performed starting from this point onward.

The FRF are obtained by applying band-limited noise excitation in the horizontal direction at the thrust node and measuring the response in the same direction. In *Figure* 9.3 natural frequencies are clearly visible at approximately 38 Hz (mode #5) and 85 Hz (mode #9), indicating that the modes at these frequencies have a strong influence on the investigated degree of freedom. Additionally, a contribution is observed at 19.6 Hz (mode #1), which can be attributed to the low damping associated with that mode.

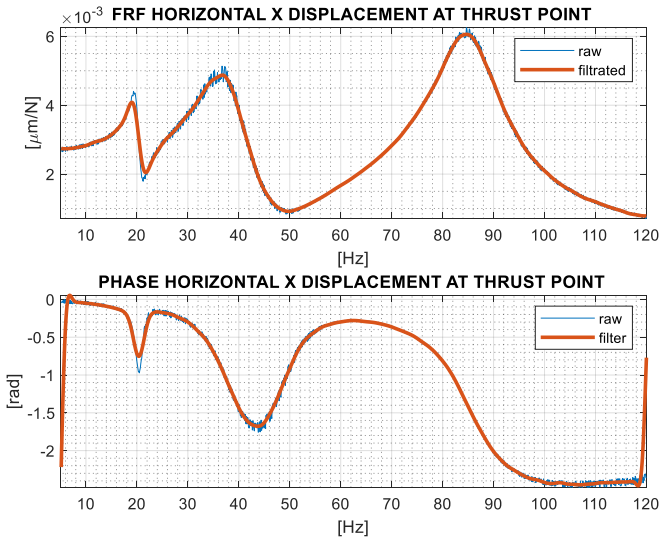

Figure 9.3: FRF of the lateral displacement in horizontal direction (x) of the thrust bearing node

To further investigate the system behaviour, the response is analysed at an additional degree of freedom: lateral displacement in horizontal direction x of the BRG #4 node, as shown in *Figure 9.4*. Several observations can be made based on the amplitude of the resulting frequency response.

- The natural frequency at 30.9 Hz (mode #4) is not present in the response, as BRG #4 lies at a node of the corresponding mode shape.
- Although the mode #6 at 44.6 Hz shows significant deformation at BRG #4, the excitation is applied at the thrust location, which is itself a node for this mode. As a result, no substantial energy is introduced into this mode.
- The 76.7 Hz component (mode #7) does not appear due to the high damping associated with the corresponding mode.
- The mode #8 at 77.6 Hz also has a node at the observation point, explaining its negligible contribution to the response.

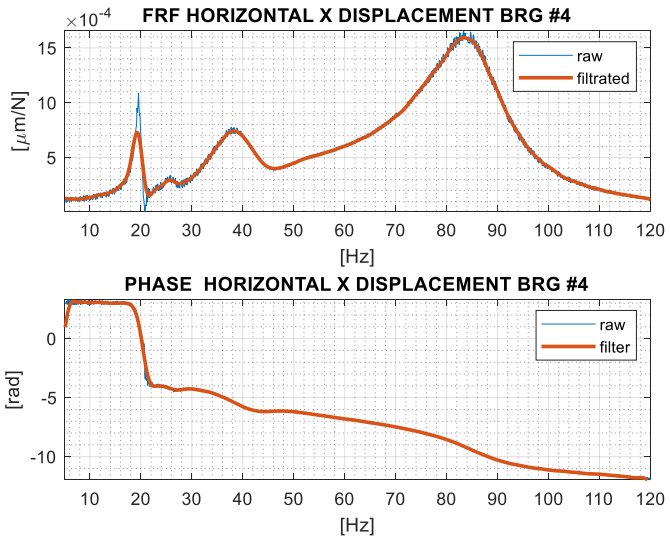

Figure 9.4: FRF of lateral horizontal x displacement of BRG #4

In this case, band-limited noise excitation is applied vertically at the node located immediately to the right of the unbalance, within the generator. This configuration predominantly excites the mode #3 at 26.2 Hz and the mode #7 at 76.7 Hz, as confirmed by the FRF measured at journal 2 in the vertical direction, in *Figure* 9.5. Despite the mode #4 at 30.9 Hz exhibits relatively small modal displacements at both the excitation node and the bearing, its low damping results in a clearly observable response. Conversely, although the mode #6 at 44.6 Hz shows significant deformation at the excitation point, its contribution to the overall response is minimal due to substantial damping.

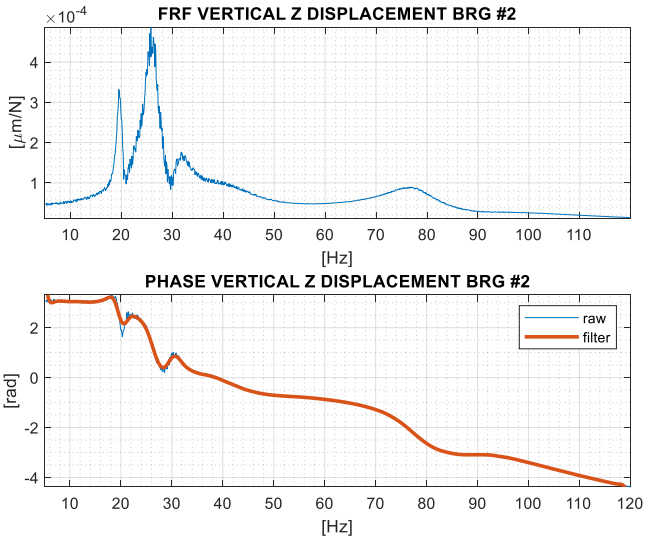

Figure 9.5: FRF of lateral vertical z displacement of BRG #4

Table 9.2 summarizes the comparisons among eigenfrequencies from the linear model in the complex domain and those identified with time integration of radial noise excitation condition.

Mode number	Eigenfrequency linear of equation of motion (Hz)	Natural freq. from noise excitation with TI (Hz): thrust node	Natural freq. from noise excitation with TI (Hz): brg #4 node	Natural freq. from noise excitation with TI (Hz): brg #1 node
1	19.58	19.52	19.33	19.33
3	26.21	Not identified	26.19	26.19
5	38.07	37.52	37.81	31.5
9	84.99	85.3	83.14	76.9

Table 9.2: Eigenfrequencies linear of equation of motion against natural frequency from noise excitation with time integration

9.2 Axial dynamics

The results below are obtained following using two strategies:

- Using the interpolator and linearized damping coefficients. The latter are computed as a function of the axial load. Since damping depends on the collar's tilt angle, the actual static tilt due to gravity is used when computing through the code the coefficients for each discrete axial load. The resulting damping coefficients are subsequently interpolated using spline interpolation.
- Using the trained neural network.

For a more detailed understanding of the errors introduced by the interpolator and net predictions, the reader is referred to *Chapter* 7.9. All the simulations performed are conducted using MATLAB Ode45 solver, with maximum step size of 1×10^{-4}, absolute tolerance of 1×10^{-20} and relative tolerance of 1×10^{-14}. A sampling frequency of 2000 Hz is adopted.

9.2.1 Axial noise

A disturbance noise is applied to the shaft during the variation of the axial load (representing fluid dynamic forces in the turbine and compressor stages) with the objective of identifying axial eigenfrequencies and comparing them to those

predicted by the linearized model. The noise time history and its spectrum are presented in *Figure 9.6*.

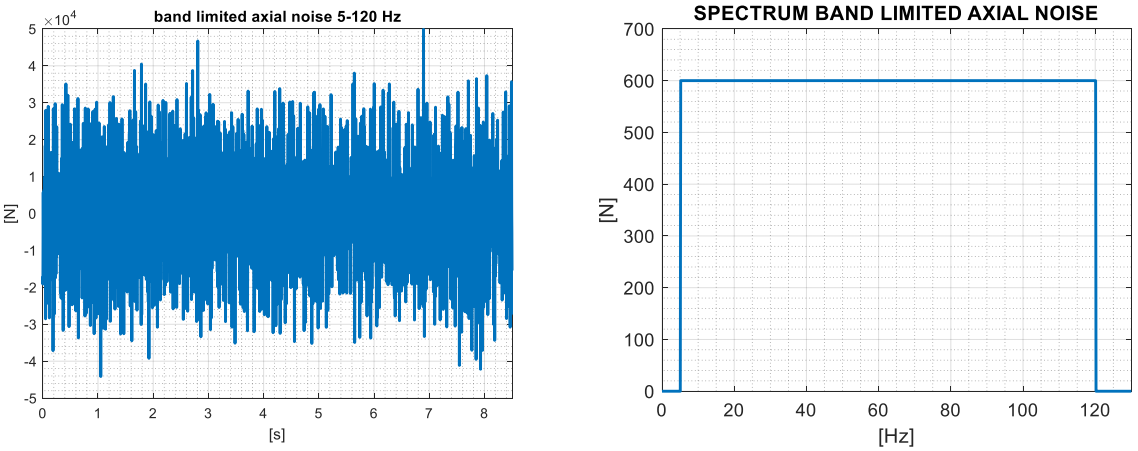

(a) (b)

Figure 9.6: (a) Time history and (b) Spectrum of axial noise

The shaft is assumed to be perfectly balanced. The neural network is employed to predict the thrust bearing force and moments. The integration time for all the analyses is set to 9.5 seconds to ensure sufficient excitation of all relevant frequencies within the noise. The noise input begins at 1 second to minimize interference with the initial transient response. Spectral evaluations are performed starting from this point onward. Different spectra for the axial *dof*, obtained by varying the axial load applied, are shown in *Figure 9.7*.

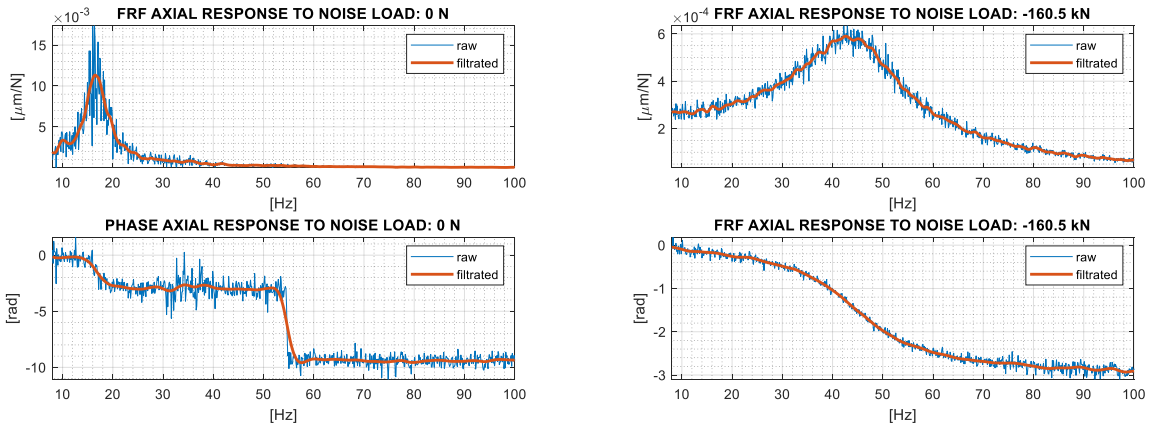

(a) (b)

Figure 9.7: FRF for axial *dof*, fixed axial load at: (a) 0 kN, (b) −160.5 kN

It can be observed from these diagrams that, as the system shifts toward the direct side (negative axial force), the bearing damping increases. This is evidenced by the reduced slope near the resonance region, the broader and less pronounced amplitude peak at higher axial loads, and the overall decrease in response amplitude. *Table 9.3* reports a comparison between axial eigenfrequencies computed using the nonlinear model and identified using a linearized approach.

Axial load [kN]	**Linear model [Hz]**	**Time integration natural frequency estimation [Hz]**	**Relative error [%]**
23.7 (load on reverse side)	27.6	29.0	4.8
0	15.4	16.0	3.8
-28.9	15.2	14.7	3.4
-81.6	28.4	26.7	6.4
-160.5 (load on direct side)	43.5	41.3	5.3

Table 9.3: Linear and nonlinear axial natural frequencies

9.2.2 Axial sinusoidal excitation

Subsequently, several simulations are performed, assuming the shaft with the same residual unbalance used in *Chapter 9.1.1*. In the results presented below, intermodulation effects are observable. According to [30], Intermodulation, or intermodulation distortion, is a phenomenon that occurs when a generic input passes through a nonlinear system, resulting in the generation of new frequency components that were not present in the original input signals. Unlike linear operations (such as addition or subtraction), nonlinear ones, like multiplication, modify the harmonic content of signals. For example, multiplying two sinusoids results in frequency components equal to the sum and difference of the original frequencies. A linear system cannot produce intermodulation. More generally, any nonlinear system with a sinusoidal input at frequency ω will generate output harmonics at $k\omega$ for integer k, known as harmonic distortion.

True intermodulation distortion only occurs when multiple frequencies are present in the input. For example, with input:

$$x(t) = A_1 cos(\omega_1 t) + A_2 cos(\omega_2 t) \tag{9.1}$$

and a nonlinear system defined by:

$$y(t) = \alpha_1 x(t) + \alpha_3 x^3(t) \tag{9.2}$$

the output includes intermodulation products at frequencies such as: $2\omega_1 \pm \omega_2$ and $2\omega_2 \pm \omega_1$.

These are intermodulation terms, not just harmonics. For an input composed of N sinusoidal components with frequencies, $\omega_1,\omega_2,\ldots,\omega_n$ the nonlinear system can generate output components at frequencies of the form:

$$k_1\omega_1 + k_2\omega_2 + \ldots + k_n\omega_n \tag{9.3}$$

where $k_1, k_2, \ldots, k_n$ are integers. The linear combination of the frequency of the input is then the frequency range associated with the output. Superharmonics 1x, 2x,3x fall inside this set. Finally, it is worth recalling what the order of intermodulation is defined as:

$$Order = |k_1| + |k_2| + \ldots + |k_n| \tag{9.4}$$

For instance, the terms $2\omega_1 \pm \omega_2$ are third order intermodulation products.

These intermodulation frequencies provide clear evidence of nonlinear dynamic behaviour and its transmission throughout the shaft.

Furthermore, the nonlinearity can even excite sub-harmonic components of the forcing terms (given ω and Ω the frequencies of excitation, some terms like $\frac{\omega}{k}$ and $\frac{\Omega}{k}$, $k = 1, \ldots, N$) as well as linear combinations of them, ie. intermodulation products.

In the case of axial combined with unbalance excitation, transient decades in about maximum 0.4 s, as shown in *Figure 9.8.* In this particular case, the shaft is forced with 14 kN of zero-peak amplitude at a frequency of 16 Hz, when the external applied static axial load is 0 kN. Under these conditions, the thrust bearing exhibits low damping, as already noted in *Chapter 8.2.1*, resulting in the slowest observed transient. To ensure a clear observation of the steady-state response, all the sinusoidal axial excitations in this paragraph are applied from 0.5 s, with a total simulation time of 5.5 s. The spectra are computed over the final 3 seconds. No significant leakage is observed using a rectangular window.

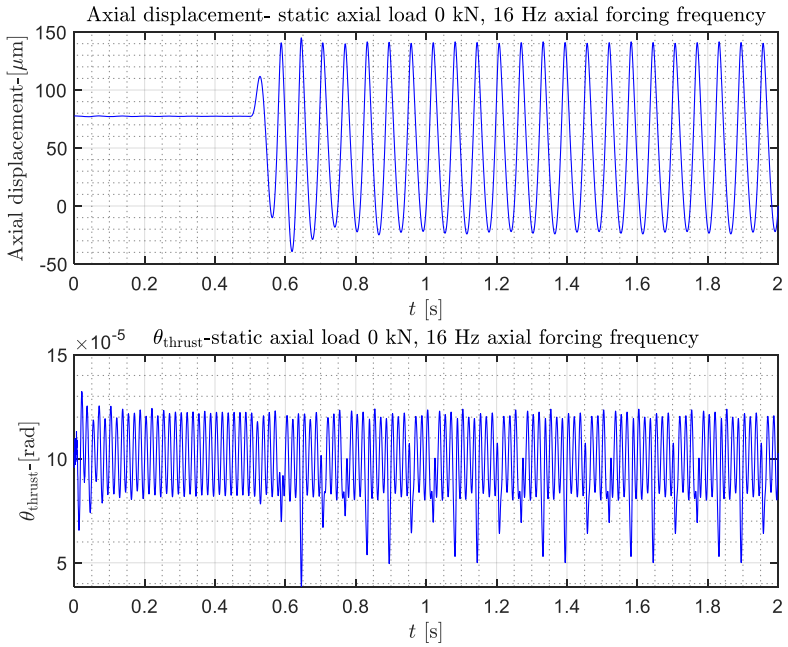

Figure 9.8: Example of time domain response to axial sinusoidal excitation: axial displacement above and θ rotation at thrust bearing node below

The system is at first excited axially with a sinusoidal force of 14 kN at 16 Hz. The axial static load is set at 0 kN. Force and moments are predicted by means of the interpolator. In this configuration the excitation is under resonance condition, in order to investigate the effect of big displacements on the nonlinear response.

Interestingly, the amplitude of the 2X harmonic of ϑ is greater than that of the 1X component, likely due to the inherent characteristics of the thrust bearing: during one cycle of sinusoidal excitation, the collar engages with both bearing surfaces, resulting in two distinct moment impulses per cycle. Nonlinear effects under this excitation are especially pronounced, with significant harmonic content observable up to the 8× harmonic.

However, in the axial direction, the difference between the dominant peak and other spectral components appears more pronounced. This observation is supported by the force–displacement response under assigned static rotation, where the relationship can be locally approximated by a linear function, suggesting quasi-linear behaviour in that region. The shaft is excited at its natural frequency under conditions of reduced stiffness and damping, causing the collar to approach both thrust bearing surfaces and experience strong force interactions, which in turn drive it back and forth between the two sides.

The effects of nonlinearity are clearly evident in the spectra of axial displacement and rotation ϑ at thrust node shown in *Figure 9.9*. This nonlinear behaviour is visible not

only near the thrust bearing but also at the journal bearing, where the waterfall plot in *Figure 9.9* has been recorded. The shaft is subjected to excitation at 16 Hz and 60 Hz, resulting in the appearance of multiple harmonic components, distinctly visible at 16 (1ω),20, 28, 32(2ω), 44,48(3ω), 60(1Ω), 64(4ω), 76, 80(5ω), 88, 92, 96(6ω), 108, 112(7ω), 120(2Ω), 124, and 128 (8ω) Hz.

Intermodulations include:

- Second-order intermodulation: $\Omega \pm \omega$, peaks at 44 Hz and 76 Hz (corresponding to 60 ± 16 Hz).
- Third-order intermodulation: $\Omega \pm 2\omega$, peaks at $28\ \text{Hz} = 60 - 2 \cdot 16$ and $92\ Hz = 60 + 2 \cdot 16$.
- Fourth-order intermodulation: $2\Omega - 2\omega$, peak at $88\ \text{Hz} = 2 \cdot 60 - 2 \cdot 16$ and $(\Omega + 3\omega)\ 108\ \text{Hz} = 3 \cdot 16 + 60$.
- Fifth-order intermodulation: $\Omega + 4\omega$ peak at $124\ \text{Hz} = 4 \cdot 16 + 60$.
- Sixth-order intermodulation: $-\Omega + 5\omega$, peak at $20\ \text{Hz} = 5 \cdot 16 - 60$.

In *Figure 9.9* illustrates the spectra of the axial displacement, the rotation of the thrust bearing around the x-axis, and the horizontal displacement of journal bearing #1.

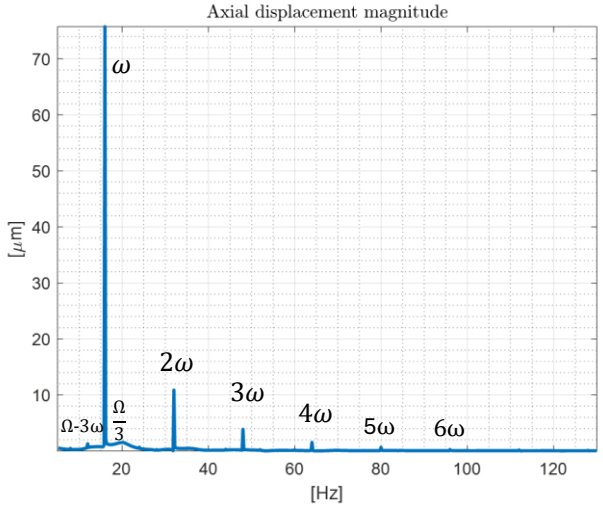

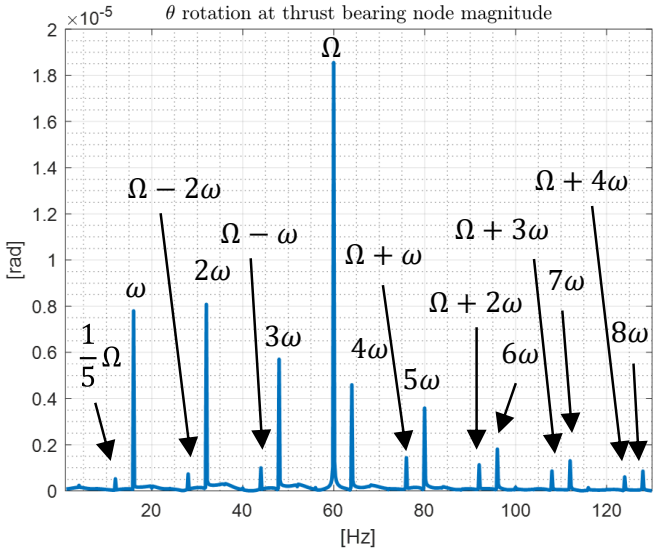

(b)

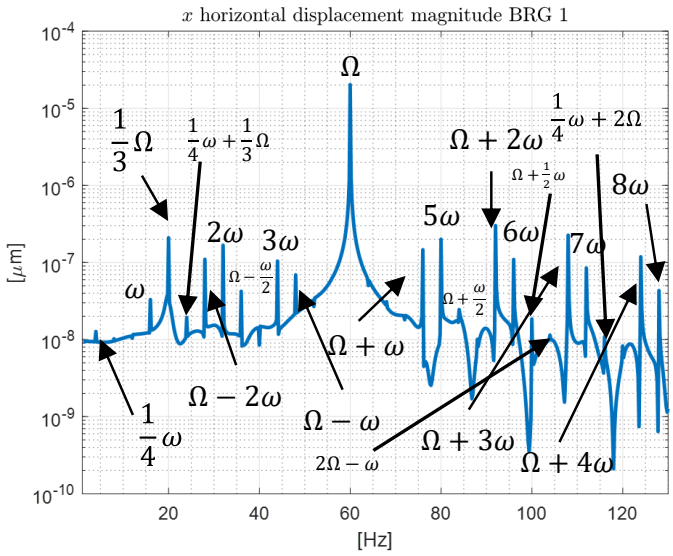

(c)

Figure 9.9: (a) Spectrum of axial displacement, static axial load 0 kN and excitation force 14 kN at 16 Hz (b) Spectrum of ϑ rotation, static axial load 0 kN and excitation force 14 kN at 16 Hz (c) Spectrum horizontal displacement x at BRG #1 node, static axial load 0 kN and excitation force 14 kN at 16 Hz

In an ideal, fully decoupled system, each direction would respond exclusively at its corresponding excitation frequency (60 Hz radially and 16 Hz axially). However, nonlinearities tend to emerge inherently in the presence of large displacements. Such displacements bring the collar into close proximity with the thrust bearing surfaces,

where the conditions for cross-directional interaction are significantly enhanced. This coupling mechanism will be further elucidated in the following example.

Similarly, the axial static load is set at -200 kN and the system is excited axially with a sinusoidal force of 50 kN at 50 Hz, close to the axial natural frequency corresponding to that load (which is approximately 47 Hz). The analysis is performed using both the interpolator and the neural network in order to assess their consistency. Some nonlinear effects are highlighted in the figures below.

As already discussed in *chapter 8*, the direct side is the region where the strongest axial-radial coupling occurs. Indeed, as shown in *Figure 9.10a* and *Figure 9.10b*, at 60 Hz a clear component is visible, although below 1 μm. It is worth to note that the linear theory predicts approximately 0.75 μm, while the current response is 0.63 μm, confirming the good predictive capability of the linear model.

Moreover, the ϑ rotations induced by axial excitations exceed those generated by mass unbalance, as evidenced by the peak at 50 Hz being higher than the peak at 60 Hz in *Figure 9.11a* and *Figure 9.11b*. This observation provides further evidence of dynamic coupling between axial and radial directions.

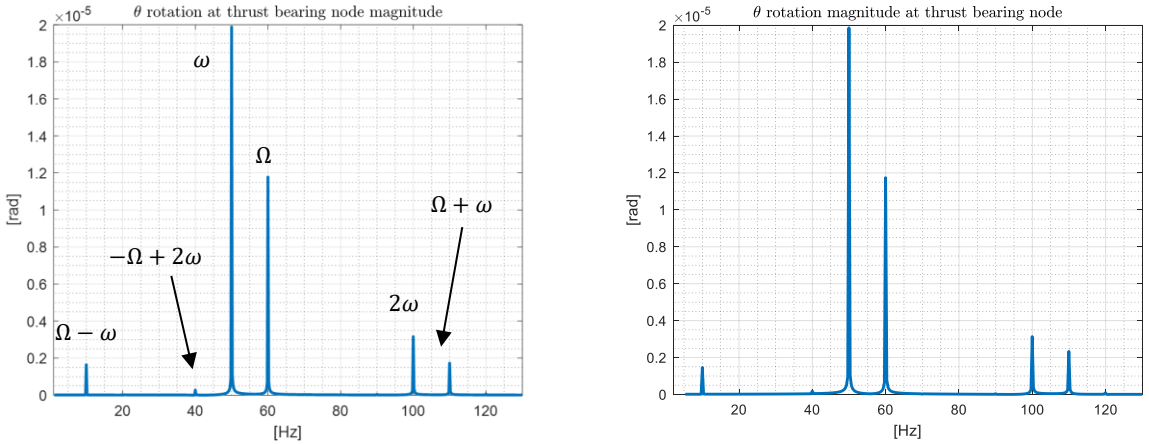

(a) (b)

Figure 9.10: Spectrum of ϑ rotation, static axial load -200 kN and excitation force 50 kN at 50 Hz: (a) with interpolator and (b) with ANN

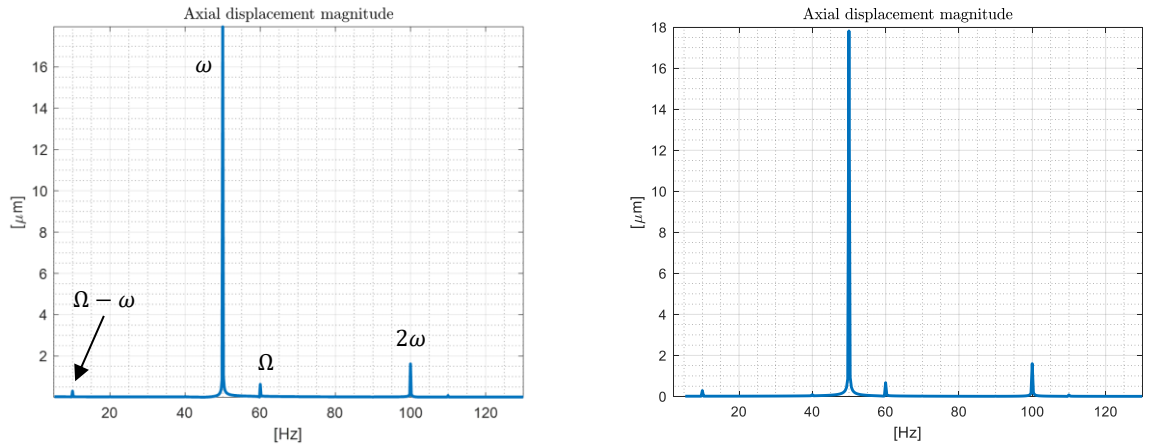

(a) (b)

Figure 9.11: Spectrum of axial displacement, static axial load −200 kN and excitation force 50 kN at 50 Hz: (a) with interpolator and (b) with ANN

From these figures, it can be deduced that both the interpolator and the neural network yield similar results, indicating that they replicate the thrust bearing response with sufficient accuracy.

9.2.3 Undamped thrust response

The use of the interpolator also enables artificial suppression of damping, effectively destabilizing the system. This configuration is of particular interest, as it highlights the onset of self-excited oscillations at a frequency matching that of the predicted resonance. In the absence of damping, whose role is to dissipate energy and attenuate system responses, the amplitude of the oscillations increases significantly. Nevertheless, the response does not diverge indefinitely, contrary to what is predicted by linear theory. This behaviour indicates the emergence of a limit cycle, in which the nonlinear restoring forces and excitation balance each other, leading to a bounded steady-state oscillation.

The system is analysed by exciting the rotor axially with a sinusoidal force of amplitude 7 kN at a frequency of ω = 30 Hz, under zero static axial load. This excitation frequency is intentionally chosen far from the axial natural frequency (16 Hz), in order to demonstrate that the dynamic coupling remains weak when the shaft is not excited in resonance. Results are shown both with damping (using the neural network) and without damping (using the interpolator). Unbalance residual forcing is considered, with the usual values and position of *Chapter 9.1.1* and *Chapter 8*. To ensure a clear observation of the steady-state response, the sinusoidal axial excitation

in this paragraph is applied from 0.5 s, with a total simulation time of 5.5 s. The spectra are computed over the final 3 seconds.

As observed in *Figure 9.12* and in *Figure 9.13*, in the damped case, the system response shows no apparent superharmonic components or intermodulation effects, as the small displacements limit the manifestation of nonlinearities. The coupling also appears very weak. In fact, the collar stays sufficiently distant from both thrust bearing surfaces. Consequently, the radial degrees of freedom are primarily excited by the unbalance force acting on the shaft at Ω = 60 Hz, while the axial one is driven mainly by axial forcing. This behaviour is supported by the near-zero 60 Hz component observed in the response along the y-direction, indicating minimal radial excitation from axial sources. Similarly, the minimal 30 Hz contribution in the ϑ response suggests negligible axial-to-rotational coupling.

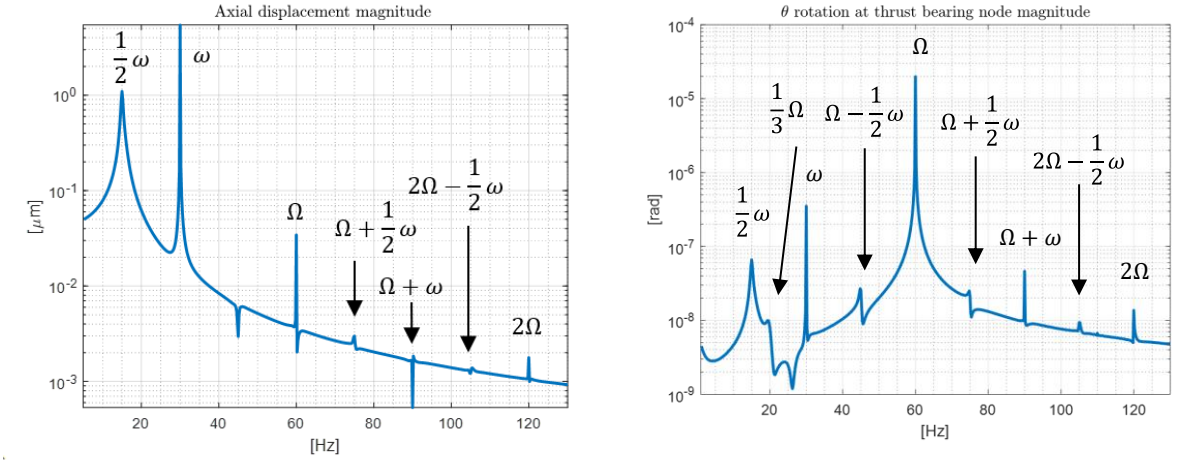

(a) (b)

Figure 9.12: (a) Spectrum of axial displacement, static axial load 0 kN and excitation force 7 kN at 30 Hz, damped case; (b) Spectrum of ϑ at thrust bearing, static axial load 0 kN and excitation force 7 kN at 30 Hz, damped case

It follows from this diagram that the predictions of linear model (8.1×10^{-4} μm/N) are in line with the response obtained by time integration ($\frac{5.4}{7000} = 7.7 \times 10^{-4}$ μm/N).

The undamped case is unstable in the linear model. However, the spectrogram of the undamped case in the nonlinear model reveals the particular descripted behaviour, with the self-excited frequency around 15 Hz present in all the simulation range, as reported in *Figure 9.13*. This value corresponds to 0.5X sub-syncronous component of the exciting frequency. Furthermore, it is also close to 16 Hz, the axial natural

frequency in the current static load case. Such sub-synchronous activation is typical of certain instability phenomena, such as whip instability in journal bearings.

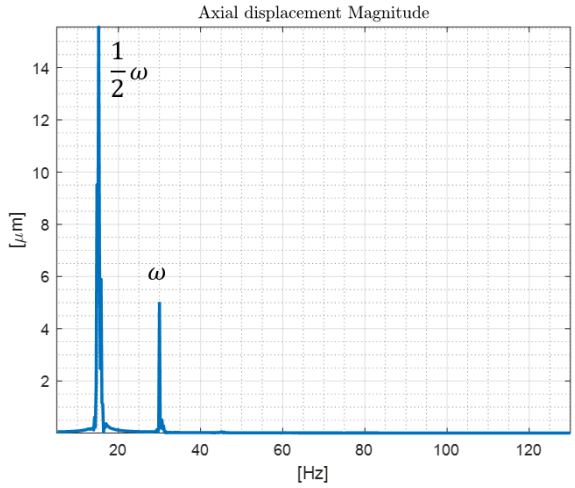

Figure 9.13: Spectrum of axial displacement, static axial load 0 kN and excitation force 7 kN at 30 Hz, undamped case

Finally, it can be noted that with damping the maximum axial displacement is 82 μm, whereas with no damping 100 μm.

9.2.4 Axial noise and radial analysis

Axial noise is often present in the current system due to turbulence generated by the flow in the turbine stages. Nonetheless, axial excitation can induce lateral vibrations because of the thrust bearing presence, and in some cases even excite radial resonances, potentially leading to critical issues.

To further investigate the coupling effects, axial noise is applied, while maintaining a constant static load. The spectrum of the response is extracted at node 32, which corresponds to brg #3.

In particular, three load cases are investigated:

- 50 kN (reverse side loaded), shown in *Figure 9.14a.*
- 0 kN shown in *Figure 9.14b.*
- -200 kN (direct side loaded), shown in *Figure 9.14c.*

In order to avoid the 60 Hz component, even in this case no unbalance excitation is considered. Interpolator is adopted in this case to replicate thrust bearing behaviour. The Frequency Response Functions (FRFs) are evaluated over a 9.5-second interval, coinciding with the duration of the applied noise load.

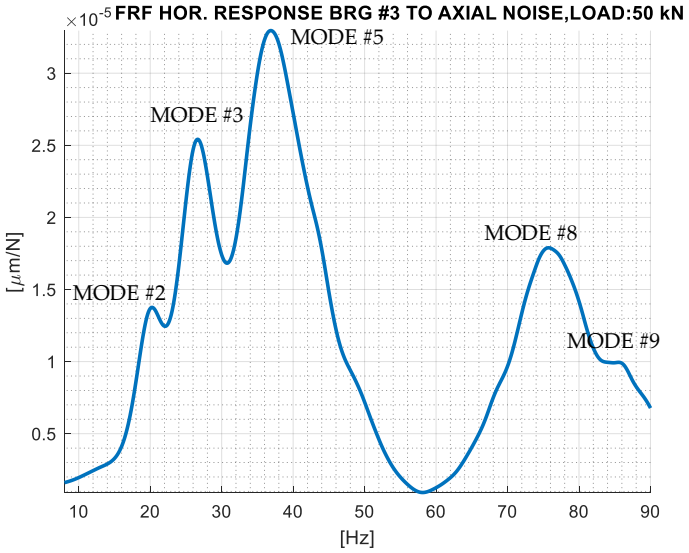
FRF HOR. RESPONSE BRG #3 TO AXIAL NOISE,LOAD:50 kN
×10^-5
MODE #2
MODE #3
MODE #5
MODE #8
MODE #9
[μm/N]
[Hz]

(a)

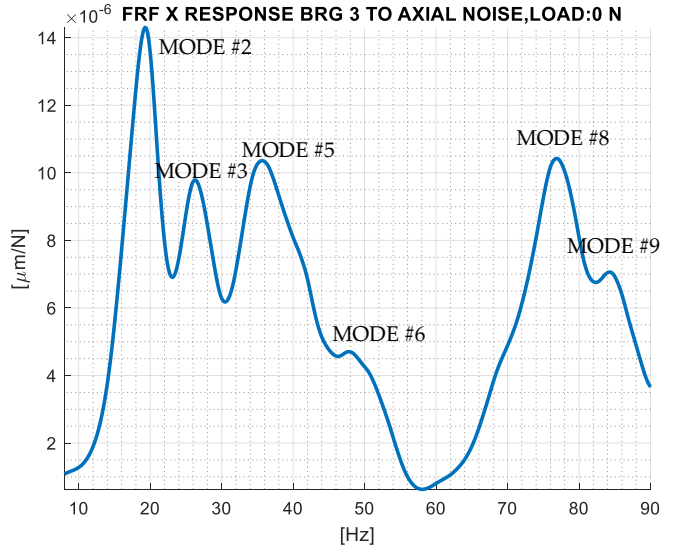
FRF X RESPONSE BRG 3 TO AXIAL NOISE,LOAD:0 N
×10^-6
MODE #2
MODE #3
MODE #5
MODE #6
MODE #8
MODE #9
[μm/N]
[Hz]

(b)

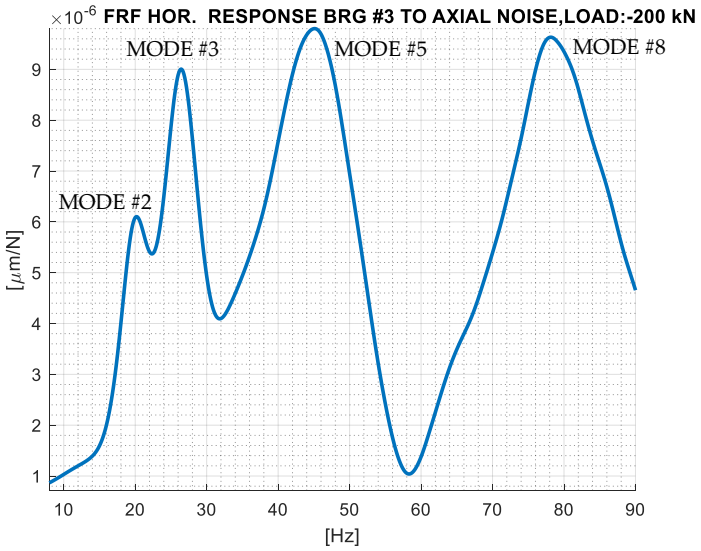

(c)

Figure 9.14: (a) FRF of radial response at bearing #3, due to axial noise, static load 50 kN; (b) FRF of radial response at bearing #3, due to axial noise, static load 0 kN; (c) FRF of radial response at bearing #3, due to axial noise, static load −200 kN

The presence of peaks at 20 (mode #2) , 26 (mode #3), 38 (mode #5), 78 (mode #8), 85 Hz (mode #9) in *Figure 9.14a*, provides further confirmation of the coupling phenomenon. Without this coupling, axial excitation would not have been able to activate radial eigenfrequency. The observed peak frequencies deviate by approximately 1 Hz from the expected natural frequencies. This discrepancy is within acceptable bounds and can be attributed to cumulative numerical errors.

It is important to note that not all natural frequencies are visible in the response. This can be explained by analysing the amplitude of the mode shapes. For a natural frequency to be sufficiently excited, the modal displacement must be significant both at the location of the observed degree of freedom and in the axial direction. For example, the axial mode at 44.5 Hz is absent in this analysis because brg #3 is a node for this mode. Likewise, the mode at 44.6 Hz (mode #6), despite showing a high amplitude in the normalized mode shape, contributes very little in terms of axial displacement. As a result, this frequency does not manifest in the FRF.

The same broadband axial excitation is applied under a 0 kN load condition. The resulting frequency response function (FRF) at the same degree of freedom is shown in *Figure 9.14b*. Even considering the amplitude scale, the response is significantly lower, despite the 0 kN load condition being associated with reduced damping. This suggests that the increased responses observed earlier are due to the presence of coupling. However, no change in the frequencies of the eigenfrequencies was

observed under the 0 kN load, indicating that the coupling affects more the amplitude than the position of the natural frequencies. 44.6 Hz (mode #6), is now visible because of low damping associated with low load.

In *Figure 9.14c*, the response is shown when the axial load is changed again to -200 kN, Although the axial eigenfrequency remains approximately at the same frequency (~45 Hz) as in the 50 kN load case, the damping is significantly higher in this scenario. This is evident from the FRF amplitude scale, which is about an order of magnitude lower compared to the 50 kN case. The direct side contributes larger restoring forces during operation, which in turn helps to smooth the system dynamic response. The peak at 45 Hz corresponds to the axial eigenfrequency, which becomes visible again due to the significantly increased counteraction of the forcing under resonant conditions.

9.2.5 Radial noise and axial analysis

Two common sources of random radial excitation in turbomachinery systems are asymmetric flow turbulences (particularly under off-design conditions or due to geometric imperfections) and irregular hydrodynamic forces in radial bearings, often caused by cavitation, wear, or inadequate lubrication. Although such excitations primarily induce lateral vibrations, axial vibrations can also be observed due to the transmission of forces through the thrust bearing. This interaction becomes particularly critical when the radial excitation contains frequency components that coincide with the axial natural frequency, potentially triggering axial resonance.

To explore the interaction between radial and axial dynamics under a plausible excitation scenario induced by the turbine stage, an analysis similar to the one reported in *Chapter 9.2.4*, is carried out by applying radial noise excitation at the location of the first turbine stage (node 10), in horizontal (x) direction and observing the response in the axial direction, in *Figure 9.15*. In order to avoid the 60 Hz component, the shaft is considered perfectly balanced. Interpolator adoption is adopted for evaluating thrust bearing forces. The Frequency Response Functions (FRFs) are evaluated over a 9.5-second interval, coinciding with the duration of the applied noise load.

Similar to previous cases, clear peaks appear at 20, 30.5, and 38 Hz, which correspond to modes #1, #4, and #5, respectively. The axial eigenfrequency around 45 Hz is also present, although it appears to be significantly attenuated and partially masked. Additionally, a peak near 61 Hz is observed, which is likely the result of nonlinear effects (2x of 30.5 Hz).

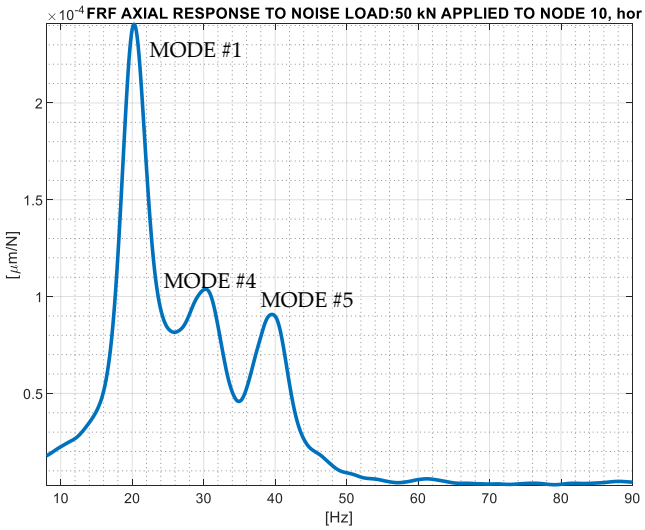

Figure 9.15: FRF of axial response, due to radial noise applied at node 10, static axial load 50 kN.

9.2.6 Load ramp with axial noise

To further emphasize the potential risks associated with axial disturbances, particularly under low load conditions, a simulation is conducted involving a increasing ramp in the applied static load, as occurred during the operating phase of the machine, combined with superimposed axial noise. The profile of the ramp is illustrated in *Figure 9.16*. The axial noise introduced shares the same frequency content as previously described, but it is distributed over a longer time interval to reflect a more persistent excitation scenario. The shaft has no residual unbalance. The total integration time is set to 120.5 s and the ramp starts at 1 s, lasting up to 120 s. Then, the static axial load is kept constant. Noise is added only during the ramp. Even in this case, the interpolator is used.

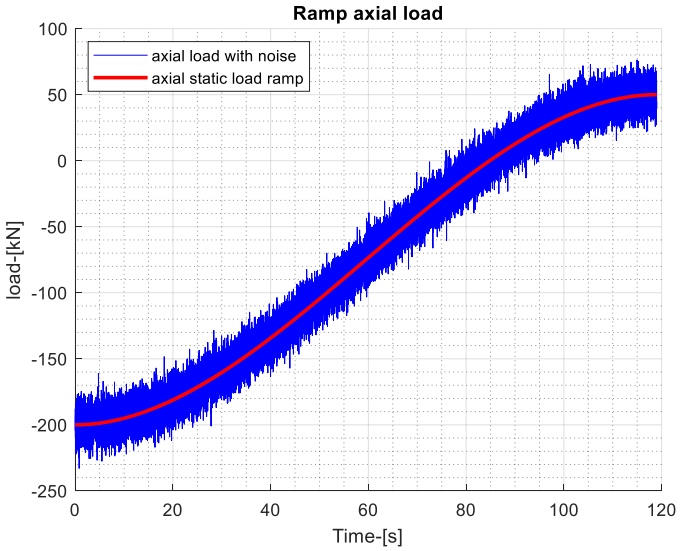

Figure 9.16: time history of load ramp, disturbed with axial noise

Figure 9.17 shows the spectrogram of the axial displacement during the ramp loading. This analysis highlights the system's pronounced sensitivity to applied static load and emphasizes the potential risks associated with low-load magnitude operating conditions. In such scenarios, both stiffness and damping are diminished, rendering the system more susceptible to external disturbances, which may result in significant displacements. Indeed, the diagram shows a red region around 16 Hz, corresponding to the axial eigenfrequency at zero static axial load.

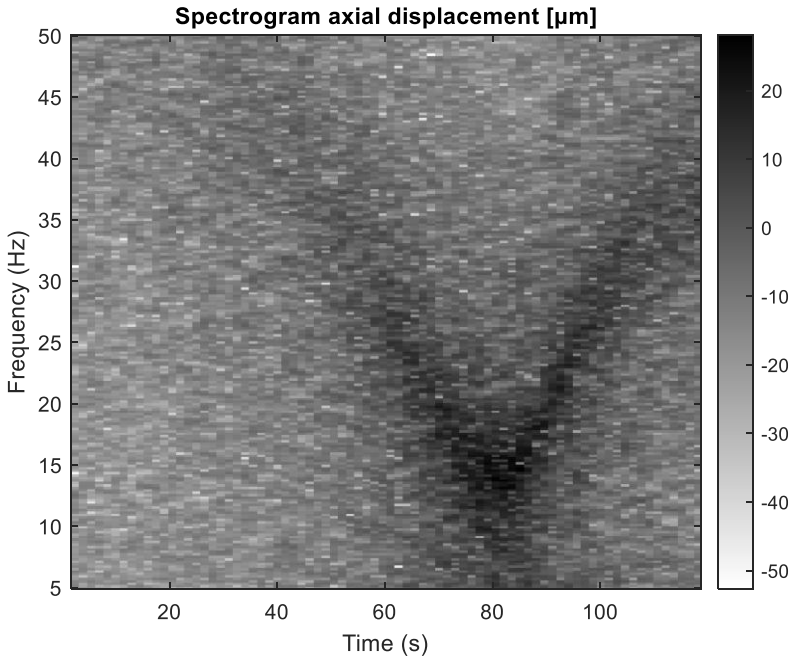

Figure 9.17: Spectrogram of axial displacement during the ramp

9.3 Pad dynamics

Finally, the model is further developed to take into account the dynamics, which is simulated then together with the full state. The resultant oil film force on each pad does not necessarily act on the pivot line, typically located at 60% of the pad length. By considering the pad, it can tilt of an angle β, around the pivot line. The moment of inertia force will balance the moment of oil film forces (pressure and shear stresses) with respect to the pivot line.

Theoretically, the generalized forces on the thrust collar also depend on the pad states when the pads are not in equilibrium. However, until now, forces and moments acting on the runner have been assumed to depend solely on the runner's state, by assuming higher pad dynamics.

A preliminary study regarding the oil film instabilities and pad dynamics is here presented: incomplete oil filling, cavitation, or insufficient film thickness can cause pad vibrations, as noted in prior research and the introduction. Pads are particularly susceptible to flutter instability. Neglecting pad dynamics altogether prevents excitation of these effects, which are important since vibrating pads exert dynamic forces on the oil film, exciting the collar at specific frequencies.

A simplified approach in terms of moment of oil film forces is to simulate oil film instabilities is to introduce a torsional disturbance noise acting on the rotation degree of freedom of one or more pads. At first, it is necessary to understand how to simulate the pad dynamics and integrate them into the dynamic condensation. Each pad is allowed to tilt only about its pivot point, which means a single degree of freedom is sufficient for each pad. Since there are 18 pads on the reverse side and 11 on the direct side, this results in 29 additional degrees of freedom. These can be denoted as β_{nR} with n going from 1 to 19 and β_{mD} with m going from 1 to 11 for the direct side. Each pad is subjected to moment of oil film forces obtained by integration of Reynolds equation, hereafter indicated as T_{number_side}, where *number* refers to the pad index and *side* to the thrust face, as well as to a moment due to its own rotational inertia. The torsional moments of inertia are calculated by the pad geometry:

$$J_{P_R} = 1.68 \times 10^{-5}\, kgm^2 \text{ and } J_{P_D} = 1.1 \times 10^{-2}\, kgm^2.$$

Just the inertia term is clearly expressed while damping and stiffness forces are included in the oil film external force T:

$$J_P \ddot{\beta}_J = T(\dot{\beta}_J, \beta_J, y, \theta, \psi, \dot{y}, \dot{\theta}, \dot{\psi})$$

It is worth recalling that the variable y represents the axial shaft degree of freedom, whereas θ and ψ correspond thrust collar rotational degrees of freedom about the x and z axes, respectively.

The forces acting on the thrust collar, therefore, include also the contribution coming from pads:

$$F_y = F_y(y, \theta, \psi, \dot{y}, \dot{\theta}, \dot{\psi}, \beta_{1R}, \dots, \beta_{19R}, \beta_{1D}, \dots, \beta_{11D})$$

$$M_x = M_x(y, \theta, \psi, \dot{y}, \dot{\theta}, \dot{\psi}, \beta_{1R}, \dots, \beta_{19R}, \beta_{1D}, \dots, \beta_{11D})$$

$$M_z = M_z(y, \theta, \psi, \dot{y}, \dot{\theta}, \dot{\psi}, \beta_{1R}, \dots, \beta_{19R}, \beta_{1D}, \dots, \beta_{11D})$$

These latter forces are computed by the Reynolds code, which evaluates all the resulting force components. The state is augmented then as already done when including the axial degree of freedom. 29 rows and 29 columns are added to each matrix and 29 elements to the vector of generalized forces.

Indicating with the subscript s the terms related to the shaft and its radial *dofs* with m the shaft mass and with y the axial degree of freedom the total system equations becomes:

$$\begin{bmatrix} M_s & 0 & 0 & \cdots & \cdots & 0 & 0 \\ 0 & J_{PR} & 0 & \ddots & \ddots & \ddots & 0 \\ 0 & 0 & J_{PR} & 0 & \ddots & \ddots & \vdots \\ \vdots & \ddots & 0 & \ddots & 0 & \ddots & \vdots \\ \vdots & \ddots & \ddots & 0 & J_{PD} & 0 & 0 \\ 0 & \ddots & \ddots & \ddots & 0 & J_{PD} & 0 \\ 0 & 0 & \cdots & \cdots & 0 & 0 & m \end{bmatrix} \begin{bmatrix} \ddot{x}_s \\ \ddot{\beta}_{1R} \\ \ddot{\beta}_{2R} \\ \vdots \\ \ddot{\beta}_{10D} \\ \ddot{\beta}_{11D} \\ \ddot{y} \end{bmatrix} + \begin{bmatrix} C_s & 0 & 0 & \cdots & \cdots & 0 & 0 \\ 0 & 0 & \ddots & \ddots & \ddots & \ddots & 0 \\ 0 & \ddots & \ddots & \ddots & \ddots & \ddots & \vdots \\ \vdots & \ddots & \ddots & \ddots & \ddots & \ddots & \vdots \\ \vdots & \ddots & \ddots & \ddots & \ddots & \ddots & 0 \\ 0 & \ddots & \ddots & \ddots & \ddots & \ddots & 0 \\ 0 & 0 & \cdots & \cdots & \cdots & 0 & 0 \end{bmatrix} \begin{bmatrix} \dot{x}_s \\ \dot{\beta}_{1R} \\ \dot{\beta}_{2R} \\ \vdots \\ \dot{\beta}_{1D} \\ \dot{\beta}_{2D} \\ \dot{y} \end{bmatrix} + \begin{bmatrix} K_s & 0 & 0 & \cdots & \cdots & 0 & 0 \\ 0 & 0 & \ddots & \ddots & \ddots & \ddots & 0 \\ 0 & \ddots & \ddots & \ddots & \ddots & \ddots & \vdots \\ \vdots & \ddots & \ddots & \ddots & \ddots & \ddots & \vdots \\ \vdots & \ddots & \ddots & \ddots & \ddots & \ddots & 0 \\ 0 & \ddots & \ddots & \ddots & \ddots & \ddots & 0 \\ 0 & 0 & \cdots & \cdots & \cdots & 0 & 0 \end{bmatrix} \begin{bmatrix} x_s \\ \beta_{1R} \\ \beta_{2R} \\ \vdots \\ \beta_{1D} \\ \beta_{2D} \\ y \end{bmatrix} = \begin{bmatrix} F_s \\ T_{1R} \\ T_{2R} \\ \vdots \\ T_{1D} \\ T_{2D} \\ F_y \end{bmatrix}$$

Since forces act on the additional degrees of freedom, they must be treated as master *dofs* in the Craig-Bampton reduction. As a result, the number of master degrees of freedom increases from 7 to 37. The number of fixed-interface modes can be kept at 40, since this value is closely related to the dynamics of the shaft. For mathematical handling of this transformation, the interested reader can refer to *Chapter 6*. All the simulations performed are conducted using MATLAB Ode23t solver, with maximum step size of 1×10^{-4}, absolute tolerance of 1×10^{-20} and relative tolerance of 1×10^{-14}, with a sampling frequency of 2000 Hz.

Results from simulations suggest that the moments on the pads of the direct sides are on the order of 1×10^{-1} Nm, while those on the reverse side are approximately one order of magnitude lower. In the following simulation, the static axial load is fixed at –200 kN, and the shaft is axially excited at 47 Hz, which corresponds to the resonance condition for that load level. Additionally, the shaft is subjected to unbalance excitation. Therefore, the expected period of the resulting signals in the degrees of

freedom is given by the least common multiple (LCM) of the periods corresponding to 60 Hz and 47 Hz.

Interestingly, nonlinear behaviour is also observed in the pads, as shown in *Figure 9.18b.* The spectrum of the collar's rotational angle θ is reported, and its amplitude distribution is comparable to that shown in *Figure 9.10*.

The pad's free transient is influenced by the global system transient. However, numerical results indicate that the overall transient decays within approximately 0.05 s, and the pad's free tilting becomes negligible after about 0.03 s.

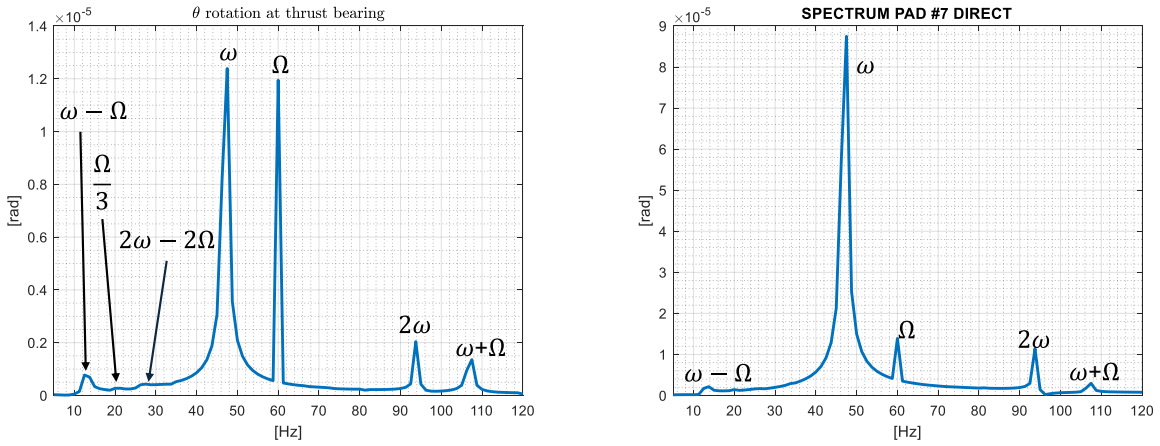

(a) (b)

Figure 9.18: (a) Rotation at thrust bearing under axial excitation at 47 Hz, load -200 kN; (b) spectrum of pad #7 direct

A band-limited Gaussian noise moment excitation is then applied to all pads on the reverse side to simulate flutter-induced excessive vibrations. To sufficiently excite the shaft motion, the noise amplitude is carefully tuned. Special care is taken to avoid non-physical conditions, such as negative film thicknesses. If such a condition occurs, the code flags an error and stops the simulation.

The final noise is band-limited between 5 Hz and 120 Hz, with an amplitude adjusted so that the resulting maximum moment is approximately two orders of magnitude greater than typical values observed on the reverse side. No unbalance is applied to the shaft, and the axial load is kept at 0 kN.

From the response spectra, some natural frequencies of the system can be identified, as shown *Figure 9.20*. However, it should be noted that the thrust bearing introduces nonlinear effects, which complicate the system's response. The axial displacement response is not completely negligible, as shown in *Figure 9.19.*

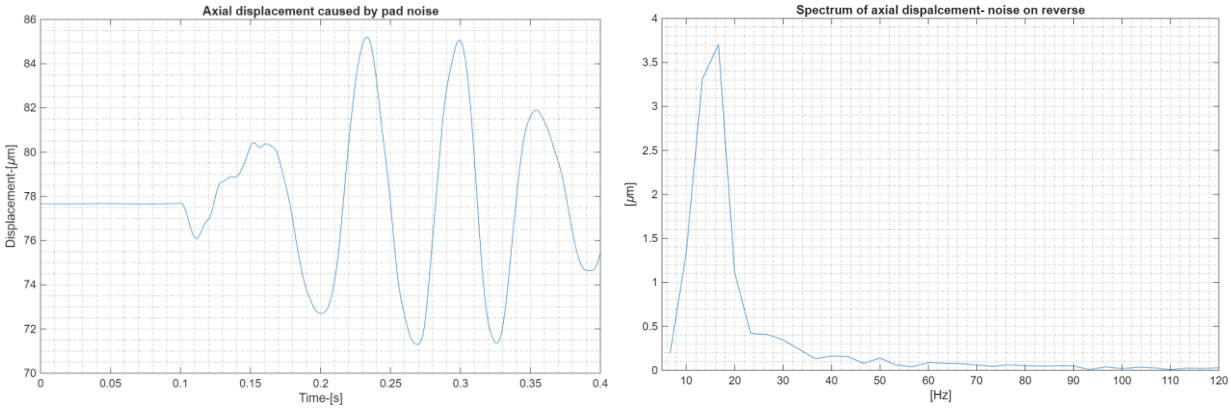

(a) (b)

Figure 9.19: (a) Axial displacement; (b) spectrum of axial displacement under noise on pads of reverse side

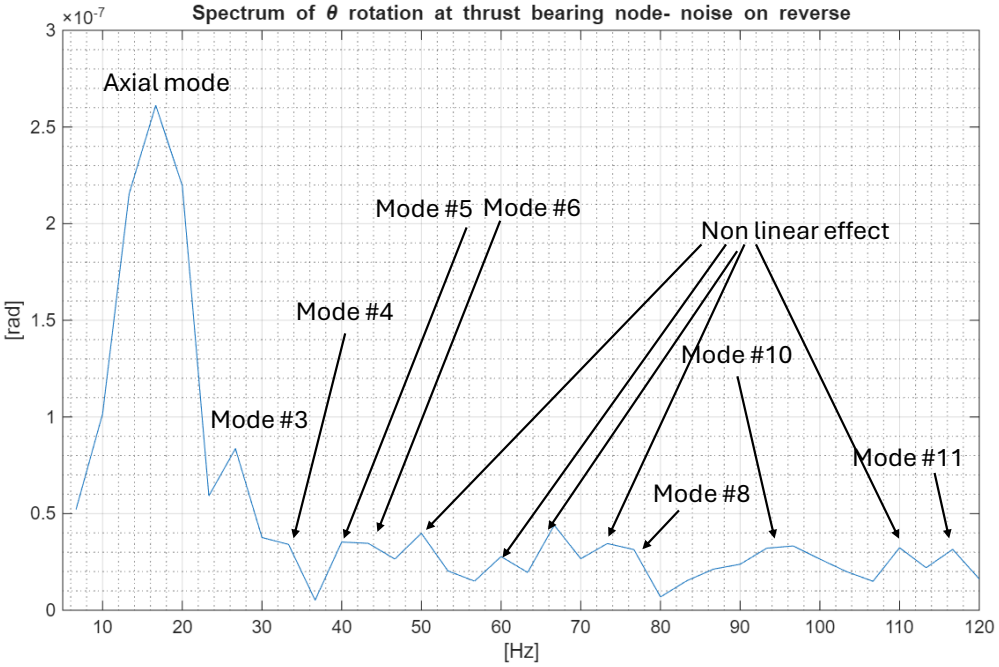

Figure 9.20: Rotation at thrust bearing node under noise on pads of reverse side

10 Conclusions

This thesis work proposes a new rotordynamic model comprising the nonlinear axial dynamics of a medium-size gas turbine. The model is a reliable tool to predict coupled lateral-axial dynamics. The thrust bearing coupling effect is widely analysed, particularly focusing on nonlinear axial force and moments generated by the lubricant. Several numerical simulations are performed, analysing the dynamic response of the system under different excitations, including random disturbances. The numerous analyses reported offer a great opportunity to enrich the knowledge about the axial Sub-Synchronous Vibrations (SSV) phenomenon and its root causes, allowing to limit it and thus reducing expensive out-of-service of the machine.

However, the proposed model relies on several approximations, for instance about damping estimation generated by the fluid film thrust bearing. For further developments, an improved model, more precise and adherent to real machines, could be developed, in order to obtain reliable results to use during the design phase of such machines. The new model could conveniently comprise effects of changing relevant parameters, here neglected, like the rotational speed of the machine or the clearance of the thrust bearing. Since axial SSV are occasionally observed also on compact automotive turbocharger, the model could be rearranged to analyse these ones, substantially different in geometry and working at a higher rotational speed with respect to gas turbines for power production.

The Artificial Neural Network (ANN) trained has obtained relatively accurate results about estimation of nonlinear Reynolds forces generated by the lubricant, but dataset limitations are significant. Enlarging the dataset is a viable solution to improve the ANN and to make it reliable in capturing nonlinear effects, especially near clearance boundaries. Because of the computational effort of solving Reynolds equations to build the dataset, an accurate evaluation of the correct trade-off between accuracy and efficiency is mandatory.

Future work may include modelling the dynamic behaviour of the bearing pads, by incorporating the dynamics itself directly into the system state equations, rather than assuming fast dynamic and instantaneous steady state. This approach would make it

possible to study potential oil film instabilities, turbulence or starvation and to evaluate the influence of flutter instability in the pads on axial excitation of the rotor.

Finally, to assess the accuracy of the model, experimental validation is needed, by comparing results from numerical simulations with the ones coming from the field.

Bibliography

[1] J. K. Whalen and M. E. Leader, 'Solving Stability Problems While Commissioning A 100 MW Turbine Generator Set.', 2003, [Online]. Available: https://hdl.handle.net/1969.1/163276

[2] L. A. Branagan, 'Survey of Damage Investigation of Babbitted Industrial Bearings', *Lubricants*, vol. 3, pp. 91–112, 2015.

[3] J. J. Wilkes, S. M. Decamillo, M. J. Kuzdzal, and J. D. Mordell, 'Evaluation Of A High Speed, Light Load Phenomenon In Tilting-Pad Thrust Bearings.', 2000, [Online]. Available: https://hdl.handle.net/1969.1/163376

[4] N. Mittwollen, T. Hegel, and J. Glienicke, 'Effect of Hydrodynamic Thrust Bearings on Lateral Shaft Vibrations', *Journal of Tribology*, vol. 113, no. 4, Art. no. 4, Oct. 1991, doi: 10.1115/1.2920697.

[5] Y. Lie and R. Bhat, 'Coupled Dynamics of a Rotor Journal Bearing System Equipped with Thrust Bearings', *Shock and Vibration*, vol. Vol.2, pp. 1–14, Jan. 1995, doi: 10.1155/1995/602701.

[6] D. Kiuchi, 'Coupled Sub-Syncronous Vibrations of Lateral and Axial directions', presented at the Turbomachinery Symposium, Turbomachinery Laboratory, 2011.

[7] W. W. Gardner, 'An Experimental Study of Thrust Pad Flutter', *Journal of Tribology*, vol. 120, no. 3, Art. no. 3, Jul. 1998, doi: 10.1115/1.2834590.

[8] O. Wu, Y. Xiaoyang, and J. Qian, 'Analysis of tilting-pad thrust bearing static instability and lubrication performance under the bistability', *Industrial Lubrication and Tribology*, vol. 66, no. 5, pp. 584–592, Aug. 2014, doi: 10.1108/ILT-08-2012-0069.

[9] A. M. Mikula and R. S. Gregory, 'A Comparison of Tilting Pad Thrust Bearing Lubricant Supply Methods', *Journal of Lubrication Technology*, vol. 105, no. 1, Art. no. 1, Jan. 1983, doi: 10.1115/1.3254542.

[10] S. DeCamillo, 'Axial Subsynchronous Vibration', 2014, doi: 10.21423/R1K35G.

[11] L. Ishimoto and R. Marques, 'Radial Subsynchronous Vibration Caused by Axial Vibration', presented at the Turbomachinery and Pump Symposia, Turbomachinery Laboratory, 2019.

[12] T. F. Peixoto and K. L. Cavalca, 'Influence of thrust bearings in lateral vibrations of turbochargers under axial harmonic excitation', in *12th International Conference on Vibrations in Rotating Machinery*, CRC Press, 2020.

[13] I. Chatzisavvas, A. Boyaci, P. Koutsovasilis, and B. Schweizer, 'Influence of Hydrodynamic Thrust Bearings on the Nonlinear Oscillations of High-Speed Rotors', *Journal of Sound and Vibration*, vol. 380, Jun. 2016, doi: 10.1016/j.jsv.2016.05.026.

[14] P. Koutsovasilis, 'Automotive turbocharger rotordynamics: Interaction of thrust and radial bearings in shaft motion simulation', *Journal of Sound and Vibration*, vol. 455, pp. 413–429, Sep. 2019, doi: 10.1016/j.jsv.2019.05.016.

[15] L. Dassi, S. Chatterton, E. Gheller, and P. Pennacchi, 'Large Axial Vibrations in Turbomachines: Non-Linear Behaviour of Double Sided Lubricated Thrust Bearing', presented at the ASME Turbo Expo 2024: Turbomachinery Technical Conference and Exposition, American Society of Mechanical Engineers Digital Collection, Aug. 2024. doi: 10.1115/GT2024-124990.

[16] M. Lalanne and G. Ferraris, *Rotordynamics Prediction in Engineering*. Chichester: John Wiley and Sons.

[17] S. P. Williams, S. Lee, and C. J. Giddings, 'Characterization of Hydrodynamic Lift Forces by Field-Flow Fractionation. Inertial and Near-Wall Lift Forces', *Chemical Engineering Communications*, vol. 130, no. 1, pp. 143–166, Jan. 1994, doi: 10.1080/00986449408936272.

[18] Y. Hori, *Hydrodynamic Lubrication*. Tokyo: Springer-Verlag, 2006. doi: 10.1007/4-431-27901-6.

[19] Y. Tian, C. Zhang, and L. Yang, 'Analysis of the longitudinal coupled dynamic characteristics of shaft-shell system considering the lubrication of thrust bearing', *European Journal of Mechanics - A/Solids*, vol. 113, Sep. 2025, doi: 10.1016/j.euromechsol.2025.105726.

[20] L. Bozzi, F. Malavasi, and V. Garotta, 'Heavy-Duty Gas Turbines Axial Thrust Calculation in Different Operating Conditions', presented at the ASME 2011 Turbo Expo: Turbine Technical Conference and Exposition, American Society of Mechanical Engineers Digital Collection, May 2012, pp. 945–954. doi: 10.1115/GT2011-46351.

[21] G. Genta, *Dynamics of Rotating Systems*. Springer, 2004.

[22] Z. Huang, 'The effect of lubricating oil temperature on the stability of rubbing rotor-bearing system', *Journal of Physics: Conference Series*, vol. 2254, no. 1, p. 012042, Apr. 2022, doi: 10.1088/1742-6596/2254/1/012042.

[23] F. Palloni, 'Implementazione del superemento di craig-bampton in femtools application framework', presented at the Problemi di vibrazioni nelle strutture civili e nelle costruzioni meccaniche, Perugia, Jun. 2004.

[24] R. R. CRAIG and M. C. C. BAMPTON, 'Coupling of substructures for dynamic analyses.', *AIAA Journal*, vol. 6, no. 7, pp. 1313–1319, 1968, doi: 10.2514/3.4741.

[25] A. M. Nielsen, *Neural Networks and Deep Learning*. Determination Press, 2015.

[26] K. P. Katsaros and P. G. Nikolakopoulos, 'Performance Prediction Model for Hydrodynamically Lubricated Tilting Pad Thrust Bearings Operating under Incomplete Oil Film with the Combination of Numerical and Machine-Learning Techniques', *Lubricants*, vol. 11, no. 3, Art. no. 3, Mar. 2023, doi: 10.3390/lubricants11030113.

[27] E. Gheller, S. Chatterton, D. Panara, G. Turini, and P. Pennacchi, 'Artificial neural network for tilting pad journal bearing characterization', *Tribology International*, vol. 188, p. 108833, Oct. 2023, doi: 10.1016/j.triboint.2023.108833.

[28] A. Chasalevris and J.-C. Louis, 'Evaluation of Transient Response of Turbochargers and Turbines Using Database Method for the Nonlinear Forces of Journal Bearings', *Lubricants*, vol. 7, no. 9, Art. no. 9, Sep. 2019, doi: 10.3390/lubricants7090078.

[29] P. Novotný, J. Hrabovský, J. Juračka, J. Klíma, and V. Hort, 'Effective thrust bearing model for simulations of transient rotor dynamics', *International Journal of Mechanical Sciences*, vol. 157–158, pp. 374–383, Jul. 2019, doi: 10.1016/j.ijmecsci.2019.04.057.

[30] C. Hutter, D. Platz, E. A. Tholén, T. H. Hansson, and D. B. Haviland, 'Reconstructing Nonlinearities with Intermodulation Spectroscopy', *Physical Review Letters*, vol. 104, no. 5, Feb. 2010, doi: 10.1103/PhysRevLett.104.050801.

[31] L. San Andrés and A. Vistamehr, 'Nonlinear rotordynamics of vehicle turbochargers: parameters affecting sub harmonic whirl frequencies and their jump', presented at the The 8th IFToMM International Conference on Rotor Dynamics, Seoul, Sep. 2010.

[32] J. Zhang, J. Tian, and T. He, 'Analysis on shafting axial vibration of marine thrust bearing considering pad geometrical parameters', *Chinese Journal of Ship Research*, vol. 13, Dec. 2018, doi: 10.19693/j.issn.1673-3185. 01245.

[33] Y. Zhang, W. Xu, Z. Li, J. He, and L. Yin, 'Dynamic Characteristics Analysis of Marine Propulsion Shafting Using Multi-DOF Vibration Coupling Model', *Shock and Vibration*, vol. 2019, no. 1, p. 5169156, 2019, doi: 10.1155/2019/5169156.

[34] R. R. Mutra, J. Srinivas, and D. Singh, 'Thrust Bearing Influence on the Stability Analysis of Turbocharger Rotor-Bearing System', in *Advances in Rotor Dynamics, Control, and Structural Health Monitoring*, S. Dutta, E. Inan, and S. K. Dwivedy, Eds., Singapore: Springer, 2020, pp. 85–98. doi: 10.1007/978-981-15-5693-7_7.

[35] A. M. Mikula, 'The Leading-Edge-Groove Tilting-Pad Thrust Bearing: Recent Developments', *Journal of Tribology*, vol. 110, 1985.

[36] H. Jiang and W. Jiang, 'Study of lateral–axial coupling vibration of propeller-shaft system excited by nonlinear friction', *Arch Appl Mech*, vol. 86, no. 8, pp. 1537–1550, Aug. 2016, doi: 10.1007/s00419-016-1134-8.

[37] L. Dassi, S. Chatterton, and P. Pennacchi, 'Identification of nonlinear dynamic parameters of thrust bearings in rotating machines: Modelling of axial Sub-Synchronous vibration and experimental verification', *Mechanical Systems and Signal Processing*, vol. 230, p. 112664, May 2025, doi: 10.1016/j.ymssp.2025.112664.

List of Figures

Figure 2.1: (a) Example of thrust bearing; (b) section comprising collar and doubled-sided thrust bearing 12

Figure 2.2: Pressure distribution in infinitely long bearing 13

Figure 2.3: Example of pad; particular of leading and trailing edge 14

Figure 2.4: Different pivot configuration: (a) point; (b) line 14

Figure 2.5: Geometry of: (a) tilting pad bearing; (b) fixed pad bearing 15

Figure 2.6: Particular of oil supply arrangement: (a) flooded; (b) spray bar; (c) LEG thrust bearing 16

Figure 2.7: Nonlinear axial load-displacement relation 18

Figure 2.8: Lalanne reference frame [16] 18

Figure 2.9: Oil film distribution due to collar rotation 19

Figure 2.10: Collar rotation 19

Figure 2.11: Static deflection due to weight 21

Figure 2.12: (a) Self levelling thrust bearing; (b) particular of the mechanism 22

Figure 2.13: Geometry of thrust bearing analysed: (a) direct side; (b) reverse side 22

Figure 3.1: Simplified geometry of a thrust bearing 25

Figure 3.2: (a) density, viscosity and heat capacity of lubricant as a function of temperature; (b) particular of dynamic viscosity as a function of temperature 28

Figure 3.3: Direct side: (a) pressure distribution; (b) film thickness 29

Figure 3.4: Input and output parameters of MATLAB code used 30

Figure 3.5: Lalanne reference frame [16] 30

Figure 4.1: (a) Fy vs y and ϑ and (b) Mx vs y and ϑ 37
Figure 4.2: (a) Mxvs ϑ, fixing y and (b) Mx vs y, fixing ϑ 37
Figure 4.3: Mz vs y and ϑ 38
Figure 4.4: permissible combinations y and ϑ 39
Figure 4.5: (a) Fy vs y and $\vartheta quad$ and (b) $Mquad$ vs y and $\vartheta quad$ 40
Figure 4.6: (a) Fy vs ϑ and ϑ and (b) Mx vs ϑ and ϑ 41
Figure 5.1: W501D machine: particular of turbine and compressor 43
Figure 5.2: Cylindrical FEM element and its degrees of freedom 46
Figure 5.3: Fibers participating to elastic energy and difference between mass and stiffness diameter 47
Figure 5.4: Assembly procedure for stiffness matrix 49
Figure 5.5: matrix general shape 50
Figure 5.6: Original FEM model 52
Figure 5.7: Reduced FEM model 53
Figure 5.8: Mode shape #2: (a) before reduction; (b) after reduction 53
Figure 5.9: Example of working fluid flow inside a turbine stage 56
Figure 5.10: Unbalance response of the system in amplitude and phase as function of shaft rotational speed located at radial bearing #1. 60
Figure 5.11: Typical response of a nonlinear system; particular of bent peak and bi-stable region 65
Figure 6.1: Craig reduction (20 modes) compared to complete model considered as reference, in terms of relative error (above) and absolute error (below) of axial displacement 75
Figure 7.1: schematic representation of the working principle of an ANN 80
Figure 7.2: main geometrical parameters of the thrust bearing 85
Figure 7.3: schematic representation of a full factorial plan with 3 factors 88
Figure 7.4: schematic representation a latin hypercube sampling 89
Figure 7.5: example of a plan, varying axial displacement and tilting angle 89
Figure 7.6: (a) Example of a plan, varying axial displacement y and tilting angle ψ, covering completely the allowable space. (b) Example of a plan, varying axial displacement y and tilting angle ϑ, covering completely the allowable space 90

Figure 7.7: (a) Absolute error of the axial force as a function of y and ϑ. (b) Relative error of the axial force as a function of y and ϑ 94

Figure 7.8: (a) absolute error of the force as a function of y and ϑ; (b) relative error of the force as a function of y and ϑ 98

Figure 8.1: (a) Stiffness and (b) Damping coefficients of the first journal bearing 100

Figure 8.2: Mode shape #1 102

Figure 8.3: Mode shape #2 102

Figure 8.4: Mode shape #4 103

Figure 8.5: Mode shape #6 103

Figure 8.6: Mode shape #8 104

Figure 8.7: Mode shape #9 104

Figure 8.8: Mode shape #10 105

Figure 8.9: Campbell diagram reporting the first 12 modes 105

Figure 8.10: Unbalance point locations and measurement points 106

Figure 8.11: Response due to unbalance (amplitude and phase) at thrust bearing node for (a) radial displacements and (b) tilting angles 107

Figure 8.12: Displacement response due to unbalance (amplitude and phase) at first journal bearing 108

Figure 8.13: Shaft radial deformation caused by unbalance excitation 108

Figure 8.14: Static deflection at -200 kN, 0 kN and 50 kN 109

Figure 8.15: Zoom of the vertical displacement due to gravity at -200 kN, 0 kN and 50 kN 110

Figure 8.16: (a) Tilting angle due to weight at the thrust node as a function of axial load; (b) Moment Mx due to weight as a function of axial load 111

Figure 8.17: Axial displacement as a function of load 111

Figure 8.18: Reaction forces at journal bearings as a function of axial load 112

Figure 8.19: (a) Stiffness and (b) Damping coefficients of the second journal bearing as a function of axial load 113

Figure 8.20: Direct damping terms as a function of the axial load 113

Figure 8.21: Direct stiffness terms as a function of the axial load 114

Figure 8.22: Cross-term damping coefficients as a function of axial load 115

Figure 8.23: Sensitivity map of the first 12 eigenfrequencies with respect to axial load 116

Figure 8.24: Axial natural frequency as a function of axial load 118

Figure 8.25: Axial FRF of the system for 0 kN axial load and -200 kN axial load ... 118

Figure 8.26: Angle ϑ of the thrust node as a function of axial load 119

Figure 8.27: Stability map for the first 12 modes, varying static load 120

Figure 8.28: Amplitude and phase of unbalance response as a function of axial load 120

Figure 8.29: Response due to unbalance (amplitude and phase) as a function of axial load, at thrust bearing node for (a) displacement and (b) tilting angle..... 121

Figure 8.30: Mode shape #7, setting axial load at -200 kN 122

Figure 8.31: Mode #8: (a) Thrust bearing free case; (b) -200 kN static axial load; (c) 50 kN static axial load 124

Figure 8.32: Mode #9: (a) Thrust bearing free case; (b) -200 kN static axial load; (c) 50 kN static axial load 126

Figure 8.33: Relocation of thrust bearing: new position marked in purple colour.... 126

Figure 8.34: Moment Mx due to weight as a function of axial load 127

Figure 8.35: amplitude and phase of unbalance response as a function of axial load, thrust node 18 127

Figure 9.1: Example of time integration result: horizontal displacement at bearing #1 130

Figure 9.2: (a) Time history of radial noise, (b) spectrum of radial noise, defined between 5 and 120 Hz 132

Figure 9.3: FRF of the lateral displacement in horizontal direction (x) of the thrust bearing node..... 133

Figure 9.4: FRF of lateral horizontal x displacement of BRG #4 134

Figure 9.5: FRF of lateral vertical z displacement of BRG #4 134

Figure 9.6: (a) Time history and (b) Spectrum of axial noise 136

Figure 9.7: FRF for axial *dof*, fixed axial load at: (a) 0 kN, (b) -160.5 kN 136

Figure 9.8: Example of time domain response to axial sinusoidal excitation: axial displacement above and θ rotation at thrust bearing node below 139

Figure 9.9: (a) Spectrum of axial displacement, static axial load 0 kN and excitation force 14 kN at 16 Hz (b) Spectrum of ϑ rotation, static axial load 0 kN and excitation force 14 kN at 16 Hz (c) Spectrum horizontal displacement x at BRG #1 node, static axial load 0 kN and excitation force 14 kN at 16 Hz 141

Figure 9.10: Spectrum of ϑ rotation, static axial load -200 kN and excitation force 50 kN at 50 Hz: (a) with interpolator and (b) with ANN 142

Figure 9.11: Spectrum of axial displacement, static axial load -200 kN and excitation force 50 kN at 50 Hz: (a) with interpolator and (b) with ANN 143

Figure 9.12: (a) Spectrum of axial displacement, static axial load 0 kN and excitation force 7 kN at 30 Hz, damped case; (b) Spectrum of ϑ at thrust bearing, static axial load 0 kN and excitation force 7 kN at 30 Hz, damped case 144

Figure 9.13: Spectrum of axial displacement, static axial load 0 kN and excitation force 7 kN at 30 Hz, undamped case 145

Figure 9.14: (a) FRF of radial response at bearing #3, due to axial noise, static load 50 kN; (b) FRF of radial response at bearing #3, due to axial noise, static load 0 kN; (c) FRF of radial response at bearing #3, due to axial noise, static load -200 kN 147

Figure 9.15: FRF of axial response, due to radial noise applied at node 10, static axial load 50 kN. 149

Figure 9.16: time history of load ramp, disturbed with axial noise 150

Figure 9.17: Spectrogram of axial displacement during the ramp 150

Figure 9.18: (a) Rotation at thrust bearing under axial excitation at 47 Hz, load -200 kN; (b) spectrum of pad #7 153

Figure 9.19: (a) Axial displacement; (b) spectrum of axial displacement under noise on pads of reverse side 154

Figure 9.20: Rotation at thrust bearing node under noise on pads of reverse side ... 154

List of Tables

Table 5.1: Main engine parameters of modelled gas turbine 44

Table 5.2: Comparison of lateral natural frequencies of complete and reduced models 53

Table 5.3: Stiffness and damping forces and their dependencies in different models 55

Table 5.4: Benchmark of the integrators commonly used in rotordynamics. 64

Table 6.1: Degrees of freedom of the system 67

Table 6.2: Simulation time for different numbers of modes considered 74

Table 6.3: comparison of the errors varying the modes 77

Table 7.1: simulation times for some net architectures 91

Table 7.2: MSE validation errors under different architectures 92

Table 8.1: Modes at 3600 rpm with damped natural frequency below 120 Hz 101

Table 8.2: Percentage variation of reaction forces of journal bearings between no-thrust and thrust cases 112

Table 8.3: Percentage variation of first 11 eigenfrequencies and corresponding non-dimensional damping factors between different analysed cases 117

Table 8.4: first 12 eigenfrequencies and corresponding non-dimensional damping factors when the thrust is activated 122

Table 9.1: Comparison between journal orbit displacements from time integration and steady state 130

Table 9.2: Eigenfrequencies linear of equation of motion against natural frequency from noise excitation with time integration 135

Table 9.3: Linear and nonlinear axial natural frequencies 137